CENTRO FEDERAL DE EDUCAÇÃO TECNOLÓGICA DE MINAS GERAIS
PROGRAMA DE PÓS-GRADUAÇÃO MULTICÊNTRICO EM QUÍMICA DE MINAS GERAIS

ALEXANDRE COELHO RODRIGUES GOMES

MECHANISMS AND KINETICS OF NEUTRAL-NEUTRAL GAS-PHASE REACTIONS INVOLVING PHOSPHORUS-BEARING SPECIES OF ASTROCHEMICAL INTEREST

BELO HORIZONTE
2025

ALEXANDRE COELHO RODRIGUES GOMES

MECHANISMS AND KINETICS OF NEUTRAL-NEUTRAL GAS-PHASE REACTIONS INVOLVING PHOSPHORUS-BEARING SPECIES OF ASTROCHEMICAL INTEREST

Thesis presented to the Multicentric Postgraduate Program in Chemistry of Minas Gerais (Programa de Pós-Graduação Multicêntrico em Química de Minas Gerais) at the Federal Center for Technological Education of Minas Gerais (Centro Federal de Educação Tecnológica de Minas Gerais), as a requirement for obtaining the degree of Doctor of Chemistry.

Supervisor: Prof. Dr. Breno Rodrigues Lamaghere Galvão
Co-supervisor: Prof. Dr. Jing Li (李晶老师)

BELO HORIZONTE

2025

Gomes, Alexandre Coelho Rodrigues.
G633m Mechanism and kinetics of neutral-neutral gas-phase reactions involing phosphorus-bearing species of astrochemical interest / Alexandre Coelho Rodrigues Gomes. – 2025.
118 f. : il.
Orientador: Breno Rodrigues Lamaghere Galvão.
Coorientador: Jing Li

Tese (doutorado) – Centro Federal de Educação Tecnológica de Minas Gerais, Programa de Pós-Graduação Multicêntrico em Química de Minas Gerais, Belo Horizonte, 2025.
Bibliografia.

1. Astroquímica. 2. Cinética química. 3. Fósforo. 4. Mecanismos de reação (Química). 5. Química teórica. I. Galvão, Breno Rodrigues Lamaghere. II. Jing, Li. II. Título.

CDD: 523.02

Ficha catalográfica elaborada pela Biblioteca - *campus* Nova Suíça - CEFET-MG
Bibliotecária: Wagner Oliveira Braga - CRB6-3261

ALEXANDRE COELHO RODRIGUES GOMES

MECHANISM AND KINETICS OF NEUTRAL-NEUTRAL GAS-PHASE REACTIONS INVOLING PHOSPHORUS-BEARING SPECIES OF ASTROCHEMICAL INTEREST

Tese apresentada ao Programa de Pós-Graduação Multicêntrico em Química de Minas Gerais, do Centro Federal de Educação Tecnológica de Minas Gerais, como requisito para a obtenção do título de Doutor em Química.

Belo Horizonte, 29 de agosto de 2025.

Aprovada pela Banca Examinadora:

_____

Prof. Dr. Breno Rodrigues Lamaghere Galvão (Orientador)

_____ _____

Prof. Dr. Márcio Oliveira Alves

Prof. Dr. Ricardo Rodrigues de Oliveira Júnior

_____ _____

Prof. Dr. Tanmoy Mondal

Prof. Dr. Vinícius Cândido Mota

To my family. 致我的家人。

Acknowledgements

First and foremost, I would like to thank God for granting me the strength to persevere during the most challenging times.

I am deeply grateful to my family — my parents, brothers, sisters-in-law, my niece Cleo, my godson João, my niece Luiza, and Nina (my adorable dog) — for the constant affection, love, and understanding you have always shown me. I dedicate this work to all of you. In particular, I would like to express my heartfelt gratitude to my parents for their unwavering support, patience, companionship, and love. Without you, this moment would not have been possible. I love you all very much.

I would like to thank my supervisor, Professor Breno Rodrigues Lamaghere Galvão, for his continuous support, guidance, understanding, patience, and for all the knowledge shared throughout my entire academic journey, from my undergraduate research to the present day. Without your mentorship, the doctoral internship I carried out in China — a country for which I hold deep respect, as I do for Brazil — would likely not have been possible, and this PhD would hardly have been concluded in such a satisfactory way. I sincerely hope to continue working with you for many years to come. Thank you very much.

I would also like to thank the Coordenação de Aperfeiçoamento de Pessoal de Nível Superior (CAPES) for providing the opportunity to undertake the doctoral internship at Qufu Normal University (曲阜师范大学), in Shandong (山东), China (中国), through Finance Code 001. This opportunity was of great importance to me, and I believe it will yield valuable and lasting outcomes in the future.

Last but not least, I would like to express my sincere gratitude to the Centro Federal de Educação Tecnológica de Minas Gerais (CEFET-MG) and its Programa de Pós-Graduação Multicêntrico em Química de Minas Gerais (PPGMQ-MG) for the institutional and financial support, resources, and academic environment that made this achievement possible in its entirety.

己所不欲，勿施于人。

《论语》

Abstract

Phosphorus is a fundamental element for both the origin and maintenance of life, yet the chemistry of phosphorus-bearing species (PBSs) in the interstellar medium (ISM), as well as the pathways leading to their bioavailability, remains poorly understood. Advancing phosphorus astrochemistry is crucial for clarifying its distribution, reactivity, and prebiotic roles. To date, seven PBSs have been detected in the ISM, with phosphorus nitride (PN) and phosphorus monoxide (PO) identified as the main gas-phase reservoirs. A detailed understanding of the formation and destruction mechanisms of these species is crucial for advancing our knowledge of the chemical evolution of this element and for the development of more accurate astrochemical models. Given the extreme physical conditions of the ISM, theoretical chemistry plays a vital role by providing rate coefficients and thermokinetic data to explore key reaction pathways. While ion-neutral processes dominate in many interstellar regions, neutral-neutral reactions remain relatively underexplored, despite their importance in explaining the observed abundances of PBSs. This work tries to address this gap by investigating, through high-level computational methods, such as CCSD(T), CASSCF, and MRCI, the mechanisms and kinetics of several neutral-neutral gas-phase reactions involving PN and PO under interstellar-like conditions. Since these processes are often inaccessible to direct experimental or observational techniques, temperature-dependent rate constants were computed using various formulations of transition state theory and incorporated into an astrochemical model to evaluate the impact of each reaction on the broader phosphorus chemistry in the ISM. Key findings include: (i) PO formation via the reaction $P(^4S) + O_2(^3\Sigma_g^-) \rightarrow O(^3P) + PO(^2\Pi)$ occurs through both doublet and quartet states, with the quartet gaining importance above 700 K; (ii) the reaction $N(^4S) + PN(^1\Sigma^+) \rightarrow N_2(^1\Sigma_g^+) + P(^4S)$ involves a highly multireference NPN system and, despite an activation barrier, yields rate constants on the order of 10^{-10}cm^3 s^{-1} at high temperatures, suggesting relevance in shock-heated regions; (iii) the reactions $N(^4S) + PH(^3\Sigma^-) \rightarrow H(^2S) + PN(^1\Sigma^+)$ and $P(^4S) + NH(^3\Sigma^-) \rightarrow H(^2S) + PN(^1\Sigma^+)$ exhibit similar rate constants, indicating both may serve as efficient PN formation pathways; (iv) in the CPN system, a barrierless mechanism was identified for PN destruction via $C(^3P) + PN(^1\Sigma^+) \rightarrow P(^4S) + CN(^2\Sigma^+)$, with the calculated rates supporting its inclusion in chemical models; and (v) analysis of the astrochemical simulations highlights the $N(^4S) + PH(^3\Sigma^-) \rightarrow H(^2S) + PN(^1\Sigma^+)$ reaction as particularly relevant for PN formation, and the $C(^3P) + PN(^1\Sigma^+) \rightarrow P(^4S) + CN(^2\Sigma^+)$ process as a key destruction pathway.

Key-words: Astrochemistry; Chemical kinetics; Phosphorus; Reaction mechanisms; Theoretical Chemistry

Resumo

O fósforo é um elemento fundamental tanto para a origem quanto para a manutenção da vida, mas a química das espécies contendo fósforo (PBSs) no meio interestelar (ISM), assim como os caminhos que levaram à sua bioacessibilidade, ainda é pouco compreendida. Avançar no campo da astroquímica do fósforo é essencial para esclarecer sua distribuição, reatividade e possíveis papéis prebióticos. Até o momento, sete PBSs foram detectadas no ISM, com o fosforeto de nitrogênio (PN) e o monóxido de fósforo (PO) reconhecidos como os principais reservatórios gasosos desse elemento. Uma compreensão detalhada dos mecanismos de formação e destruição dessas espécies é crucial para aprimorar nosso entendimento sobre a evolução química deste elemento e para o desenvolvimento de modelos astroquímicos mais precisos. Diante das condições extremas do ISM, a química teórica desempenha um papel central ao fornecer coeficientes de taxa e dados termocinéticos necessários para a identificação de vias reacionais relevantes. Embora processos íon-neutro predominem em muitas regiões interestelares, reações entre espécies neutras permanecem relativamente pouco exploradas, apesar de sua importância para explicar as abundâncias observadas de PBSs. Este trabalho busca preencher essa lacuna por meio da investigação, com métodos computacionais de alto nível, como CCSD(T), CASSCF e MRCI, dos mecanismos e da cinética de diversas reações gasosas neutro-neutro envolvendo PN e PO, em condições semelhantes às do meio interestelar. Como esses processos são frequentemente inacessíveis por vias experimentais ou observacionais diretas, constantes de velocidade dependentes da temperatura foram calculadas com diferentes formulações da teoria do estado de transição e incorporadas a um modelo astroquímico, com o objetivo de avaliar o impacto individual de cada reação na química do fósforo no ISM. Os principais resultados obtidos incluem: (i) a formação de PO na reação $P(^4S) + O_2(^3\Sigma_g^-) \rightarrow O(^3P) + PO(^2\Pi)$ ocorre por estados dupleto e quarteto, sendo este último mais relevante acima de 700 K; (ii) a reação $N(^4S) + PN(^1\Sigma^+) \rightarrow N_2(^1\Sigma_g^+) + P(^4S)$ envolve um sistema NPN altamente multirreferencial e, apesar de apresentar barreira de ativação, atinge constantes da ordem de 10^{-10}cm^3 s^{-1} em altas temperaturas, sugerindo importância em regiões aquecidas por choques; (iii) as reações $N(^4S) + PH(^3\Sigma^-) \rightarrow H(^2S) + PN(^1\Sigma^+)$ e $P(^4S) + NH(^3\Sigma^-) \rightarrow H(^2S) + PN(^1\Sigma^+)$ apresentam constantes de velocidade semelhantes, indicando ambas como possíveis rotas eficientes de formação de PN; (iv) no sistema CPN, identificou-se um mecanismo sem barreira para a destruição de PN via $C(^3P) + PN(^1\Sigma^+) \rightarrow P(^4S) + CN(^2\Sigma^+)$, com taxas calculadas que justificam sua inclusão em modelos astroquímicos; e (v) a análise das simulações astroquímicas destaca a reação $N(^4S) + PH(^3\Sigma^-) \rightarrow H(^2S) + PN(^1\Sigma^+)$ como particularmente relevante para a formação de PN, e o processo $C(^3P) + PN(^1\Sigma^+) \rightarrow P(^4S) + CN(^2\Sigma^+)$ como uma via-chave de destruição.

Palavras-chaves: Astroquímica; Cinética química; Fósforo; Mecanismos de reação; Química teórica

List of Figures

Figure 1 – Temperature-density diagram of interstellar clouds. 23
Figure 2 – Surrounding environments involved in the formation of a protostar. 24
Figure 3 – Surroundings of a CEs. 25
Figure 4 – Hybridization of phosphorus atomic orbitals. 25
Figure 5 – Potential energy profile for a generic reaction. 54
Figure 6 – Minimum energy path for the $P(^4S) + O_2(^3\Sigma_g^-) \rightarrow O(^3P) + PO(^2\Pi)$ reaction calculated at CAS/AVTZ+d level for both doublet and quartet PESs. 69
Figure 7 – State-averaged CAS/AVTZ+d optimized cuts along the POO→O+PO dissociation including four A' doublet states. 70
Figure 8 – Potential energy diagram for the formation of PO at the MRCI(Q)/AVTZ+d//CAS/AVTZ+d level. 71
Figure 9 – Single-state MRCI(Q)/AVXZ+d//CAS/AVXZ+d ($X = T, Q, 5$) optimized cuts along the POO→P+O_2 dissociation on the ground $^2A'$ state. 72
Figure 10 – Rate coefficients as a function of temperature for the $P(^4S) + O_2(^3\Sigma_g^-) \rightarrow O(^3P) + PO(^2\Pi)$ reaction. 75
Figure 11 – Potential energy diagram for the destruction of PN by nitrogen atoms. 77
Figure 12 – Rate coefficients as a function of temperature for the N + PN → N_2 + P reaction. . 80
Figure 13 – Potential energy diagram for the doublet state state of HPN. 82
Figure 14 – Search for intersystem crossing regions between doublet and quartet potential energies surfaces (N+PH). 84
Figure 15 – Search for intersystem crossing regions between doublet and quartet potential energies surfaces (P+NH). 85
Figure 16 – Minimum energy path from HPN towards the H+PN channel. 86
Figure 17 – Rate coefficients as a function of temperature (HPN). 87
Figure 18 – Rate coefficients as a function of temperature for the P+NH → N+PH (black) and N+PH → P+NH (blue) reactions. 88
Figure 19 – Rate coefficients as a function of temperature for the destruction of PN by H atoms. 89
Figure 20 – Potential energy diagram for the $^3A'$ (red) and $^3A''$ (black) electronic states of the CPN system. 91
Figure 21 – Rate coefficients as a function of temperature obtained for the exoergic reactions (CPN). 94
Figure 22 – Rate coefficients as a function of inverse temperature obtained for the endoergic reactions (CPN). 95
Figure 23 – Ratios of [PO]/[PN] as a function of time in the diffuse/translucent cloud model. . . 97
Figure 24 – Evolution of the abundances of P, PO, PN and the radical PH (dashed line) in the diffuse/translucent cloud model. 98

Figure 25 – Evolution of the abundances of P, PO, PN and the radical PH (dashed line) in the dense cloud model. 99
Figure 26 – Major reactions for PN. 100
Figure 27 – Major reactions for PO. 101

List of Tables

Table 1 – PN, PO and CP in astrochemical environments. 28
Table 2 – Possible term symbols for some electron configurations. 41
Table 3 – Relationship between Λ and its corresponding spectroscopic term symbol 42
Table 4 – Multiplicities of molecular electronic states for given multiplicities of the separated atoms. 50
Table 5 – Properties of the stationary points of $1^2A'$ PESs at differents levels of theory and the O(^{3}P)+PO($^2\Pi$) asymptotic limit^a. 73
Table 6 – Properties of the stationary points of $1^4A'$ PESs at differents levels of theory^a. . . . 74
Table 7 – Properties of the stationary points of $1^4A'$ PES at differents levels of theory^a. . . . 78
Table 8 – Rate coefficients as a function of temperature for the different methodologies studied in this section of the work using a Modified Arrhenius equation fit (NPN). 81
Table 9 – Properties of the stationary structures of the doublet HPN PES^a. 83
Table 10 – Rate coefficients as a function of temperature for all reactions studied in this section of the work using a modified Arrhenius equation fit (HPN). 89
Table 11 – Properties of the asymptotic limits and stationary points of $^3A'$ and $^3A''$ PESs^a. . . 92
Table 12 – Rate coefficients as a function of temperature for all reactions studied in this section of the work using a modified Arrhenius equation fit (CPN). 94
Table 13 – List of chemical reactions involving phosphorus-bearing species explored in the models (SILVA et al., 2025). 96

List of abbreviations and acronyms

AC	Activated Complex
AE	Activation Energy
AVXZ	Augmented correlation consistent basis sets
B3LYP	Hybrid Exchange and Correlation Functional Becke, Three-Parameter, Lee-Yang-Parr
CAS	Complete Active Space
CASSCF	Complete Active Space Self-Consistent Field
CC	Coupled Cluster
CCSD	Coupled-Cluster with Single and Double excitations
CCSD(T)	Coupled Cluster with Single, Double and perturbative Triple excitations
CCSD(T)-F12	Coupled Cluster Singles and Doubles and Perturbative Triples including explicit correlation
CBS	Complete Basis Set
CEs	Circumstellar Envelopes
CI	Configuration Interaction
CVT	Canonical Variational Transition State Theory
DFT	Density Functional Theory
EC	Electron correlation
HF	Hartree-Fock
HP	Hartree product
IRC	Intrinsic Reaction Coordinate
ISM	Interstellar Medium
KIDA	Kinetic Database for Astrochemistry
KS	Kohn-Sham

LCAO	Linear combination of atomic orbitals
LR-TST	Long-range transition state theory
M	Multireference diagnostic
M06-2X	Hybrid meta-GGA Minnesota exchange and correlation functional 06
MCSCF	Multi-Configuration Self-Consistent Field
ME	Master equation
MEP	Minimum Energy Path
MO	Molecular Orbital
MRCI	Multi-Reference Configuration Interaction
MRCI(Q)	Multi-Reference Configuration Interaction with Davidson correction
PBMs	Phosphorus-bearing molecules
PBSs	Phosphorus-bearing species
PES	Potential Energy Surface
RRHO	Rigid-Rotor Harmonic-Oscillator
SCF	Self-Consistent Field
SCT	Small Curvature Tunneling
TS	Transition State
TST	Transition State Theory
UHF	Unrestricted Hartree-Fock
UMIST	University of Manchester Institute of Science and Technology (astrochemical database)
VRC-TST	Variable Reaction Coordinate Transition State Theory
VTST	Variational Transition State Theory
ZPE	Zero point energy

List of symbols

Σ	Electronic state symbol
Π	Electronic state symbol
ω	Spin coordinate
$\chi(x)$	Spin-orbital as a function of spatial and spin coordinates
$\psi(r)$	Spatial part of the wavefunction
$\alpha(\omega)$	Spin-up function (quantum spin coordinate)
$\beta(\omega)$	Spin-down function (quantum spin coordinate)
ψ^{HP}	Hartree product wavefunction
$f(i)$	Fock operator
ε_i	Energy of the i-th spin-orbital
$\chi(r_i)$	Spin-orbital
$C_{\mu i}$	Expansion coefficient of basis function μ in spin-orbital i
$\chi_i(r)$	Kohn-Sham one-electron spin orbital
$\hbar$	Reduced Planck constant
∇^2	Laplacian operator
$\rho(r)$	Electron density at position r
Z_I	Atomic number of nucleus I
T_1	T_1 diagnostic
ψ_{HF}	Hartree-Fock wavefunction
h	Planck's constant
$\hat{H}$	Hamiltonian operator
C_0^2	Magnitude of the dominant configuration in the CI wave functions
$V(x)$	Total potential energy of a system

α, β, γ	Parameters of the modified Arrhenius equation
k_B	Boltzmann constant
p_j	Probability of a system being in a state with energy E_j
$k(T)$	Temperature-dependent rate constant
$AB^{\ddagger}$	Transition state complex
$\Delta G^{\ddagger}$	Gibbs free energy of activation
$\Delta H^{\ddagger}$	Enthalpy of activation
$\Delta S^{\ddagger}$	Entropy of activation
κ	Transmission coefficient
R	Gas constant
Q	Molecular partition function
q_{trans}	Translational partition function
q_{rot}	Rotational partition function
q_{vib}	Vibrational partition function
q_{elec}	Electronic partition function
E_{vdw}	van der Waals interaction energy
E_{LJ}	Lennard-Jones potential energy
N_A	Avogadro's number
$K^{\ddagger}$	Equilibrium constant between the transition state and the reactants

Contents

1 INTRODUCTION 17
1.1 Justification and motivation 19
1.2 Objectives 19
1.2.1 Main 19
1.2.2 Specifics 20

2 LITERATURE REVIEW 21
2.1 Astrochemistry and astrophysics: introduction and interstellar environments 21
2.2 Astrochemistry of phosphorus 25
2.2.1 The element phosphorus 25
2.2.2 Phosphorus in astrochemical environments 26
2.2.2.1 Review on the selected reactions 28
2.3 Neutral-neutral reactions in astrochemical environments 30
2.4 Computational chemistry 31
2.4.1 The Born-Oppenheimer approximation 31
2.4.2 The Hartree-Fock (HF) method for electronic structure calculation 32
2.4.3 Density Functional Theory (DFT) 34
2.4.4 Post Hartree-Fock (HF) electronic structure calculation methods 35
2.4.4.1 Configuration Interaction (CI) 36
2.4.4.2 Multi-Configuration Self-Consistent Field (MCSCF) 37
2.4.4.3 Multireference Configuration Interaction (MRCI) 38
2.4.4.4 Coupled Cluster Theory (CC) 39
2.5 Atomic/molecular term symbols and molecular symmetry 41
2.6 Chemical kinetics 43
2.6.1 Arrhenius equation: dependence on temperature 45
2.6.2 Potential-energy surfaces (PESs) 46
2.6.2.1 Wigner-Witmer rules 49
2.6.3 Chemical reactions: from the microscopic to the macroscopic level 50
2.6.4 Transition state theory (TST) 53
2.6.4.1 Variational Transition State Theory 57
2.6.5 The Multiple-Well Master Equation 59

3 METHODOLOGY 62
3.1 $\mathbf{P}(^4\mathbf{S}) + \mathbf{O}_2(^3\Sigma_g^-) \rightarrow \mathbf{O}(^3\mathbf{P}) + \mathbf{PO}(^2\Pi)$ 63
3.2 $\mathbf{N}(^4\mathbf{S}) + \mathbf{PN}(^1\Sigma^+) \rightarrow \mathbf{N}_2(^1\Sigma_g^+) + \mathbf{P}(^4\mathbf{S})$ 64

3.3 $\mathbf{P}(^4\mathbf{S}) + \mathbf{NH}(^3\Sigma^-) \rightarrow \mathbf{H}(^2\mathbf{S}) + \mathbf{PN}(^1\Sigma^+)$ **and** $\mathbf{N}(^4\mathbf{S}) + \mathbf{PH}(^3\Sigma^-) \rightarrow \mathbf{H}(^2\mathbf{S}) + \mathbf{PN}(^1\Sigma^+)$ . . . **66**
3.4 **CPN system** . . . **67**

4 RESULTS AND DISCUSSION . . . **68**
4.1 $\mathbf{P}(^4\mathbf{S}) + \mathbf{O}_2(^3\Sigma_g^-) \rightarrow \mathbf{O}(^3\mathbf{P}) + \mathbf{PO}(^2\Pi)$ . . . **68**
4.1.1 Potential energy surface and reaction mechanism . . . 68
4.1.2 Comparison between methods . . . 72
4.1.3 Reaction rates coefficients . . . 74
4.2 $\mathbf{N}(^4\mathbf{S}) + \mathbf{PN}(^1\Sigma^+) \rightarrow \mathbf{N}_2(^1\Sigma_g^+) + \mathbf{P}(^4\mathbf{S})$ . . . **77**
4.2.1 Potential energy surface and reaction mechanism . . . 77
4.2.2 Reaction rates coefficients . . . 79
4.3 $\mathbf{P}(^4\mathbf{S}) + \mathbf{NH}(^3\Sigma^-) \rightarrow \mathbf{H}(^2\mathbf{S}) + \mathbf{PN}(^1\Sigma^+)$ **and** $\mathbf{N}(^4\mathbf{S}) + \mathbf{PH}(^3\Sigma^-) \rightarrow \mathbf{H}(^2\mathbf{S}) + \mathbf{PN}(^1\Sigma^+)$ . . . **82**
4.3.1 Potential energy surface and reaction mechanisms . . . 82
4.3.2 Reaction rates coefficients . . . 86
4.3.3 Destruction of PN by H atoms in high temperature regions . . . 88
4.4 **CPN system** . . . **90**
4.4.1 Potential energy surface and reaction mechanisms . . . 90
4.4.2 Reaction rates coefficients . . . 93
4.5 **Astrochemical modeling** . . . **95**
4.5.1 [PO]/[PN] ratios . . . 97
4.5.2 Abundances of phosphorus-bearing species as a function of time . . . 97
4.5.3 Key reactions that influence the abundances of PN and PO . . . 99

5 CONCLUDING REMARKS AND FUTURE DIRECTIONS . . . **102**

6 FINAL ACKNOWLEDGEMENTS . . . **105**

BIBLIOGRAPHY . . . **106**

APPENDIX A – LIST OF PUBLICATIONS RELATED TO THIS WORK . . . **118**

1 Introduction

Phosphorus plays a critical role in the structure of key biological molecules and in the metabolic activities of living organisms (MACIÁ, 2005; HUNTER, 2012; GOLDFORD et al., 2017; RIVILLA et al., 2020; SOUSA-SILVA et al., 2020; ALTWEGG et al., 2016; CONCEPCIÓN et al., 2021). It forms the phosphate ion (PO_4^{3-}), a water-soluble compound whose salts are abundant on Earth and were readily accessible during the origin and evolution of life (HUNTER, 2012). As a fundamental structural component of nucleic acids (DNA and RNA), it constitutes the phosphate backbone that links nucleotides, and it is also a key element in adenosine triphosphate (ATP), the main energy carrier in living organisms, as well as in phospholipids, which are essential for maintaining the integrity of cell membranes (WESTHEIMER, 1987; MACIÁ, 2005). The ubiquity of phosphorus in these essential biomolecules highlights its central role in both the origin and maintenance of life as we know it. However, despite its biological importance, the chemistry of phosphorus-bearing species (PBSs) in the interstellar medium (ISM) remains poorly understood, and how this element became biologically available on Earth is still an open question (HUNTER, 2012; RIVILLA et al., 2020; ALTWEGG et al., 2016; CHANTZOS et al., 2020; ZIURYS, 2024). In this context, investigating the astrochemistry of phosphorus is crucial for elucidating its distribution and reactivity in space, thereby contributing to astrochemical models and to a better understanding of the chemical pathways that may have led to the emergence of life.

The prebiotic chemistry on early Earth, including processes involving PBSs, may have been influenced or enriched by the delivery of material from extraterrestrial sources, such as comets and asteroids (PASEK; LAURETTA, 2005; ALTWEGG et al., 2016; FERNÁNDEZ-RUZ; JIMÉNEZ-SERRA; AGUIRRE, 2023). As a result, studying the chemical processes occurring in various astrophysical environments, such as molecular clouds and star-forming regions, is crucial for gaining a deeper understanding of the primordial phosphorus chemistry that may have contributed to the origins of life on our planet.

To date, seven PBSs have been reliably detected in the ISM (PN, PO, PH_3, HCP, CP, CCP and SiP) with phosphorus monoxide (PO) being the most prevalent and frequently observed, particularly in oxygen-rich circumstellar envelopes (CEs) and molecular clouds (ZIURYS, 2024). Phosphorus nitride (PN) and PO are believed to represent the main reservoirs of gas-phase phosphorus in the ISM, although their relative abundances are still somewhat uncertain (MCGUIRE, 2022; LEFLOCH et al., 2016; THORNE et al., 1984; BECK et al., 2013; TENENBAUM; WOOLF; ZIURYS, 2007; SILVA et al., 2025). Current astrochemical models may lack key destruction pathways for PN (FERNÁNDEZ-RUZ; JIMÉNEZ-SERRA; AGUIRRE, 2023), which could help explain discrepancies in the predicted [PO]/[PN] ratios. Consequently, investigating the formation and destruction mechanisms of these molecules is essential for enhancing our

understanding of their spatial distribution and evolution, ultimately contributing to more accurate and comprehensive phosphorus-related astrochemical models.

Astrochemical reactions are very difficult to be modelled within an experimental approach. Especially regarding their kinetics, due to the very low (sometimes very high) temperatures and pressures observed in space. A theoretical temperature-dependent obtained rate coefficient may give some help in finding those reactions that are more likely to take place in the different regions of the ISM, thus, efficiently contributing to phosphorus astrochemistry. Obtaining these rates can also aid in building a more comprehensive chemical network that incorporates PBSs.

Although many regions of the ISM, such as photon-dominated zones and areas influenced by cosmic rays and UV radiation, are rich in ionizing agents that favour ion–neutral reactions (typically more efficient due to lower activation energy barriers), neutral–neutral processes have remained comparatively understudied. However, it has been demonstrated that not all neutral–neutral reactions require activation energy. In particular, those involving atoms and radicals can occur rapidly, often proceeding along barrierless pathways through the formation of strongly bound, energized intermediates (SMITH; HERBST; CHANG, 2004; TERZIEVA; HERBST, 1998; HERBST et al., 1994; YAMAMOTO, 2017; CLARY et al., 1994; CARTECHINI et al., 2002; KAISER et al., 2002). Several studies have stressed the importance of deepening our understanding of neutral–neutral reactions in order to build more complete and reliable kinetic databases for astrochemical modelling.

For example, Smith, Herbst and Chang (2004) present a gas-phase reaction network for interstellar chemistry with particular emphasis on neutral–neutral processes. The authors replace outdated hard-sphere approximations with updated rate estimates and include additional rapid neutral reactions. Similarly, Puzzarini (2022) emphasize the significance of neutral–neutral chemistry in the ISM, especially in low-density environments dominated by highly reactive species and gas-phase interactions. Furthermore, Agúndez and Wakelam (2013) review the chemical kinetics databases and reaction networks, with particular focus on the performance of chemical models in cold dark clouds. They highlight that experimental studies, especially those conducted at low temperatures, have revealed that many neutral–neutral reactions, particularly those involving at least one radical, can proceed rapidly and without activation barriers. These findings challenge the earlier assumption that such reactions are inefficient under interstellar conditions, thus shifting the traditional emphasis away from only regarding ion–neutral chemistry. In fact, numerous exothermic neutral–neutral reactions have now been shown to be barrierless and highly efficient at low temperatures, underscoring their crucial role in shaping molecular abundances in dark interstellar clouds environments.

It is therefore evident that neutral–neutral reactions must not be overlooked in the construction of robust astrochemical models. This is particularly true for the chemistry of PBSs, where a comprehensive model must include all relevant reaction types, especially those involving key species such as PN and PO.

1.1 Justification and motivation

As previously mentioned and discussed, the justification and motivation for this work lie in the investigation of reaction mechanisms and the calculation of rate constants for reactions involving the two main phosphorus-bearing species (PBSs) detected in the ISM (PN and PO), with the aim of advancing our understanding of phosphorus astrochemistry. All selected gas phase neutral-neutral reactions, for which mechanisms were explored and rate coefficients computed, are considered relevant for explaining the observed abundances of these molecules in the ISM. Moreover, the atomic species selected to collide with PN and PO (oxygen, nitrogen, carbon, and hydrogen) are also known to be abundant in such environments.

The originality of this research lies in addressing phosphorus-related astrochemical reactions for which there is limited or no available data on their mechanisms and kinetic behaviour. By supplying accurate kinetic data, this work can contribute to the development of more complete and realistic chemical networks used in astrochemical modeling. The final results obtained by this study are expected to enhance the understanding of the formation and destruction mechanisms of PN and PO in the ISM, and, in a broader way, have the potential to impact not only the field of astrochemistry, but also adjacent areas such as experimental and observational astrochemistry, astronomy, astrophysics, and, perhaps, even astrobiology.

To achieve the goals proposed, the work employs state-of-the-art computational methodologies, such as CCSD(T), CASSCF, and MRCI, enabling the characterization of fundamental processes that are, mainly, currently beyond experimental and observational reach. For each process chosen, mechanisms and chemical kinetics studies were conducted, and temperature-dependent rate constants were obtained using different variants of transition state theory. Finally, the reactions were incorporated into an astrochemical model developed by our group, allowing the individual contribution of each process to the overall phosphorus chemistry to be assessed.

1.2 Objectives

1.2.1 Main

Given the importance of the study of phosphorus-bearing species in the interstellar medium, the main objective of this work is to theoretically study the mechanisms and kinetics of relevant neutral-neutral gas-phase reactions considering phosphorus astrochemistry, in other words, to understand more about phosphorus astrochemistry.

1.2.2 Specifics

As specifics objectives, the proposed ones are:

- Perform high-level electronic structure calculations to investigate the mechanisms of reactions:
  - $P(^4S) + O_2(^3\Sigma_g^-) \rightarrow O(^3P) + PO(^2\Pi)$;
  - $N(^4S) + PN(^1\Sigma^+) \rightarrow N_2(^1\Sigma_g^+) + P(^4S)$;
  - $P(^4S) + NH(^3\Sigma^-) \rightarrow H(^2S) + PN(^1\Sigma^+)$;
  - $N(^4S) + PH(^3\Sigma^-) \rightarrow H(^2S) + PN(^1\Sigma^+)$;
  - $C(^3P) + PN(^1\Sigma^+) \rightarrow [P(^4S) + CN(^2\Sigma^+), P(^4S) + CN(^2\Pi), N(^4S) + CP(^2\Sigma^+)]$; and
  - $N(^4S) + CP(^2\Sigma^+) \rightarrow P(^4S) + CN(^2\Sigma^+)$.
- Theoretically calculate the rate constants of all these processes using different variants of Transition State Theory;
- Provide new theoretical data on phosphorus astrochemistry to the most commonly found astrochemicals databases; and
- Employ astrochemical models in order to evaluate the significance of each investigated reaction for phosphorus astrochemistry.

2 Literature review

2.1 Astrochemistry and astrophysics: introduction and interstellar environments

Astrochemistry is a highly interdisciplinary field that studies the rich and diverse chemical processes occurring throughout the universe. It brings together scientists from various backgrounds, including those who investigate relevant physical and chemical phenomena in the laboratory or through computational simulations; those who analyze molecular spectra using large telescopes across different regions of the electromagnetic spectrum; and those who develop extensive kinetic models to simulate the chemistry of specific astrophysical environments (HERBST; JR, 2013). These models aim to investigate and propose mechanisms underlying chemical processes in astrophysical environments, helping to explain the presence and formation pathways of various molecules. As described by Alexander Dalgarno, considered by some as the "father" of this field of knowledge, astrochemistry represents a blending of astronomy and chemistry in which each area enriches the other in a mutually stimulating interaction (PUZZARINI, 2022; DALGARNO, 2008). The field encompasses the study of molecular formation, destruction, and excitation in space, as well as their impact on the structure, dynamics, and evolution of astronomical objects (DALGARNO, 2008).

Laboratory simulations, observational data, and theoretical approaches are complementary: each can support and validate the findings of the other. These methodologies also contribute to the study of prebiotic chemistry, which explores the chemical processes that may have led to the origin of life, as well as to our understanding of star and planet formation (YAMAMOTO, 2017; TIELENS, 2021). As such, astrochemistry is a relatively young but rapidly evolving discipline, driven especially by advances in observational techniques, laboratory methods, and theoretical modelling.

Astrophysics, in turn, is a branch of astronomy that applies principles of physics and chemistry to understand the birth, evolution, and death of stars, planets, and other celestial bodies. Astrophysicists use theories such as classical mechanics, quantum mechanics, and general relativity to explain the formation, interactions, and long-term behaviour of these objects. At its core, astrophysics seeks to uncover the physical mechanisms that govern the universe at both microscopic and macroscopic scales. For molecular astrophysicists, analyzing the chemical makeup of interstellar space provides insights into the large-scale properties of the universe, while the extreme environmental conditions offer unique opportunities to understand the microscopic processes governing molecular excitation and relaxation (YAMAMOTO, 2017; TIELENS, 2021). Understanding the chemical and molecular evolution of matter in the universe is therefore

essential for reconstructing its history, complementing studies on structure formation and physical evolution processes (YAMAMOTO, 2017; TIELENS, 2021; BASU, 2025).

These two fields are closely related, as both focus on the universe beyond Earth, rely on astronomical observations, and contribute to the understanding of cosmic evolution and the origins of life. The key distinction lies in their specific focus: while astrochemistry investigates the formation, interaction, and evolution of chemical elements and molecules in space, astrophysics concerns itself with the physical properties and processes of celestial bodies and phenomena. This work specifically focuses on astrochemistry and its objectives.

Although the contribution of atoms and molecules to the total mass of the universe is very small (HINSHAW et al., 2013; COLLABORATION et al., 2014), this small fraction comprises the fundamental building blocks of galaxies, stars, and planets. Of the total mass of atoms and molecules in the universe, 98% consists of hydrogen and helium, while heavier elements such as carbon, nitrogen, oxygen and phosphorus make up the remaining 2%. In the Milky Way, 90% of the mass is concentrated in stars, with the remaining 10% constituting the interstellar matter (YAMAMOTO, 2017). The interstellar medium (ISM), which occupies this space, is composed of diffuse gas and dust distributed between stars. It exhibits significant variations in density, temperature, and ionization, and is governed by the gravitational influence of stellar components. As both the site of star formation and the repository of material ejected from dying stars, enriched by stellar nucleosynthesis, the ISM plays a vital role in the evolution of galaxies (SNELL, 2023).

Molecules are found in a wide variety of astronomical environments, such as diffuse and dense clouds in the ISM and in circumstellar envelopes (CEs) of evolved stars. The ISM is far from thermodynamic equilibrium, and its chemical processes are dominated by kinetics rather than thermodynamics. This is due to the non-equilibrium nature of the ISM, where low temperatures and gas densities coexist with intense ultraviolet radiation and energetic ions. Under such conditions, the rates and pathways of chemical reactions critically determine the molecular composition (TIELENS, 2021).

Among the environments found in the ISM, molecular clouds are particularly significant as dense regions where molecules are formed and where stars and planets originate. Prebiotic organic molecules, considered precursors to biologically relevant compounds, are commonly detected in these regions (ZIURYS, 2024). These clouds are primarily composed of neutral and ionized hydrogen, molecular hydrogen, helium, and trace elements such as carbon, oxygen, nitrogen, phosphorus, and other heavier species. Dust particles, mainly silicates and carbonaceous compounds, are also present. Heavier elements are often depleted in these dust grains, reducing their observed gas-phase abundances compared to lighter elements such as hydrogen and helium (YAMAMOTO, 2017; TIELENS, 2021).

The ISM is composed of distinct regions that vary mainly in temperature, density, and ionization state. Molecular clouds are dense and cold, whereas diffuse clouds are less dense and

warmer. The most tenuous regions, such as coronal gas and intercloud media, are not shielded from ultraviolet light and are therefore both ionized and diffuse. Figure 1 presents a schematic temperature-density diagram of these interstellar clouds (YAMAMOTO, 2017).

Figure 1 – Temperature-density diagram of interstellar clouds.

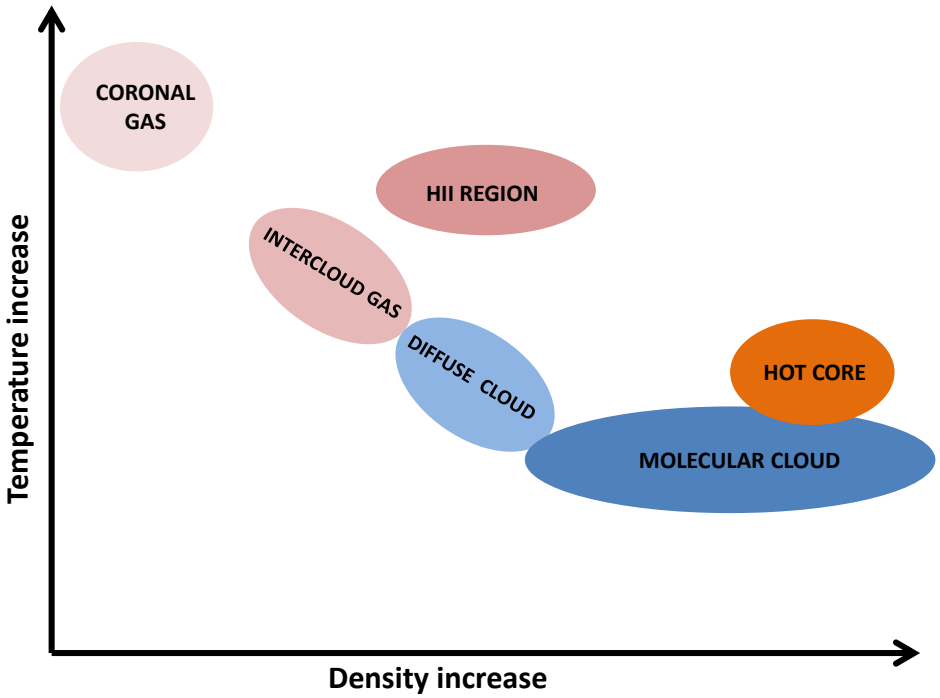

Source: Adapted from Yamamoto (2017).

Shock waves from supernovas explosions and stellar winds compress and heat the ISM, making it a highly turbulent environment. These dynamic processes contribute to its structure, chemical composition, and the triggering of star formation. Gravity also plays a critical role, as regions within molecular clouds may collapse under their own gravitational pull to form protostars. These protostars can further influence their surroundings through radiation and ionization, continuing the cycle of stellar birth and ISM enrichment. In this way, the ISM is part of a continuous cycle in which stars are formed from interstellar gas and later return material to the ISM, enriched with heavier elements (YAMAMOTO, 2017; TIELENS, 2021; SNELL, 2023).

Chemical processes play a fundamental role in star formation. As a molecular cloud collapses due to gravity, local temperature and density increase, leading to the formation of protostars. The regions surrounding a forming star include shock- and radiation-dominated areas, each characterized by distinct chemical processes and species, including atomic, molecular, and dust components. Radiation also plays a crucial role in ISM chemistry. Ultraviolet radiation from nearby stars ionizes hydrogen and other elements, initiating ionization and recombination processes. In these events, electrons recombine with ions to form neutral atoms, which can then participate in neutral-neutral reactions (YAMAMOTO, 2017; ZIURYS, 2006; RIVILLA et al., 2020). Which are the focus of this work. Figure 2 illustrates the surrounding environments

involved in protostar formation.

Figure 2 – Surrounding environments involved in the formation of a protostar.

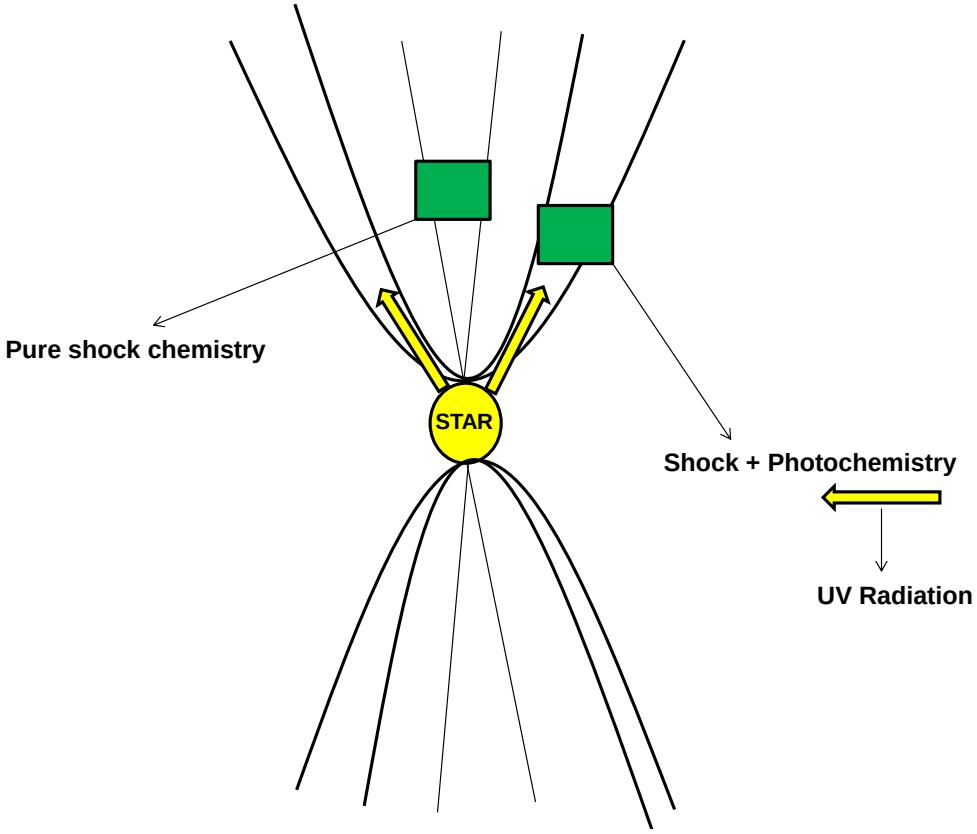

Source: Adapted from Rivilla et al. (2020).

Circumstellar envelopes (CEs) are gaseous and dusty regions formed by mass loss from evolved stars, such as supergiants. These envelopes contribute significantly to ISM enrichment by releasing heavy elements and dust. The gas in CEs is primarily composed of molecular hydrogen, but may also include carbon monoxide and a variety of organic and inorganic species. The inner regions of CEs are characterized by higher temperatures and densities, fostering complex chemical reactions and molecule formation. Mass loss through CEs plays an important role in the late stages of stellar evolution. Figure 3 presents a schematic view of a circumstellar envelope (ZIURYS, 2006).

In summary, the combined perspectives of astrochemistry and astrophysics provide a robust framework for understanding the molecular and physical processes that shape the universe. The ISM and related environments are chemically rich and dynamically active, serving as the backdrop for the formation of stars, planets, and potentially life. Among the many elements present in these environments, phosphorus stands out due to its essential role in biology and its intriguing, yet still poorly understood, chemistry in space (ZIURYS, 2024). The following section explores the astrochemistry of phosphorus, focusing on its occurrence, molecular forms, and relevance in the ISM and CEs.

Figure 3 – Surroundings of a CEs.

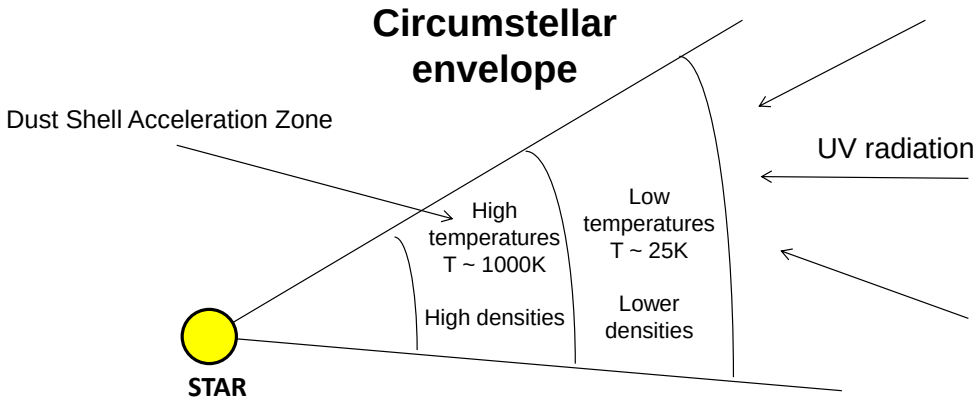

Source: Adapted from Ziurys (2006).

2.2 Astrochemistry of phosphorus

2.2.1 The element phosphorus

Under ambient temperature and pressure conditions ($T = 298.15, K$, $p = 1, atm$), phosphorus (P, Z=15) is a solid element. It exhibits common oxidation states of –3, +3, and +5. Phosphorus occurs in several allotropic forms, including white, red, and black phosphorus. Under room conditions, black phosphorus is the most thermodynamically stable allotrope (SHRIVER et al., 2008; LEE, 1999).

As mentioned before, phosphorus can easily form compounds with other elements, such oxygen, forming phosphates, which are vital for biological systems. It can also form compounds with halogens, metals and hydrogen. It is an element essential for life as we know it, being found in DNA (deoxyribonucleic acid), RNA (ribonucleic acid) and ATP (adenosine triphosphate). It is also a component of bones and teeth, when combined with calcium (SHRIVER et al., 2008; LEE, 1999; MACIÁ, 2005; HUNTER, 2012; GOLDFORD et al., 2017; RIVILLA et al., 2020; SOUSA-SILVA et al., 2020; ALTWEGG et al., 2016; CONCEPCIÓN et al., 2021).

Due to its electronic configuration (Figure 4), its atomic orbitals can hybridize into five sp^3d orbitals, allowing it to form compounds such as PCl_5.

Figure 4 – Hybridization of phosphorus atomic orbitals.

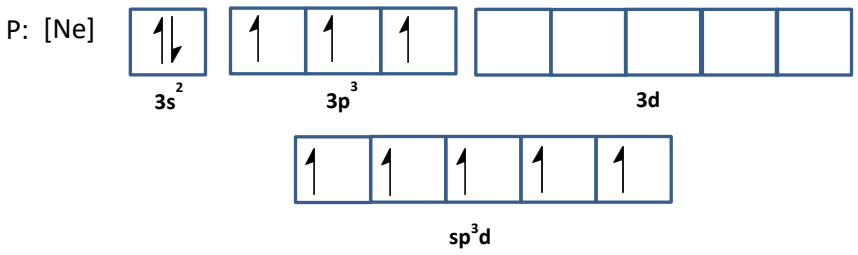

Source: Adapted from Lee (1999).

2.2.2 Phosphorus in astrochemical environments

The identification of PBSs in the ISM has been limited, with phosphorus monoxide (PO) and phosphorus nitride (PN) being the primary detections (YAMAMOTO, 2017; MCGUIRE, 2022). These species have been predominantly observed in high-mass star-forming regions and in the CEs of evolved stars (RIVILLA et al., 2016).

PN, notably the first phosphorus-containing molecule detected in space in the late 1980s within the Orion-KL region of the Orion Molecular Cloud (TURNER; BALLY, 1987; ZIURYS, 1987), has since been observed in several other molecular clouds (BERNAL; KOELEMAY; ZIURYS, 2021) as well as in various high-mass star-forming environments (ANDREAZZA; ALMEIDA; BORIN, 2016; RIVILLA et al., 2020; LEFLOCH et al., 2016). PO, by contrast, is typically associated with oxygen-rich evolved stellar environments (RIVILLA et al., 2016), but has more recently been identified in multiple star-forming regions and low-mass protostars (BERNAL; KOELEMAY; ZIURYS, 2021; BERGNER et al., 2019; RIVILLA et al., 2020), often coexisting with PN. Moreover, both PN and PO have been detected in molecular clouds located in the outer regions of the Galaxy (KOELEMAY; GOLD; ZIURYS, 2023).

Evidence supporting a shock-induced origin for PN in star-forming regions comes from the strong correlation observed between the spectral line profiles of PN and silicon monoxide (SiO), a known shock tracer (LEFLOCH et al., 2016; FONTANI et al., 2019). Furthermore, factors such as the duration of the pre-shock phase and the abundance of atomic nitrogen have been shown to significantly impact the gas-phase abundances of both PO and PN (LEFLOCH et al., 2016). Research by Aota and Aikawa (2012) indicates that in solar-type star-forming regions, atomic nitrogen plays a critical role in PN chemistry, requiring maximum shock temperatures exceeding 4000 K for its formation (LEFLOCH et al., 2016). The most commonly employed neutral-neutral reactions in astrochemical databases that account for PN formation were initially proposed by Millar, Bennett and Herbst (1987):

$$\mathrm{PO}(^2\Pi) + \mathrm{N}(^4\mathrm{S}) \rightarrow \mathrm{PN}(^1\Sigma^+) + \mathrm{O}(^3\mathrm{P}) \tag{2.1}$$

$$\mathrm{PO}(^2\Pi) + \mathrm{N}(^4\mathrm{S}) \rightarrow \mathrm{P}(^4\mathrm{S}) + \mathrm{NO}(^2\Pi) \tag{2.2}$$

$$\mathrm{PH}(^3\Sigma^-) + \mathrm{N}(^4\mathrm{S}) \rightarrow \mathrm{PN}(^1\Sigma^+) + \mathrm{H}(^2\mathrm{S}). \tag{2.3}$$

While experimental validation of these reactions is still lacking, the rate coefficients utilized in kinetic models are typically estimated through comparisons with analogous processes. Recent computational studies have provided support for the rate constants of reactions 2.1 and 2.2 (SOUZA; SILVA; GALVÃO, 2021; SILVA et al., 2025). The rate coefficient adopted for reaction 2.3 in databases like UMIST (MILLAR et al., 2024) and KIDA (WAKELAM et al., 2024) was inferred by drawing a chemical analogy to the reaction N+NH $\rightarrow$ N_2+H (SMITH; HERBST; CHANG, 2004), which has been extensively studied both theoretically and exper-

imentally (CARIDADE et al., 2005; HACK; WAGNER; ZASYPKIN, 1994; MILLER et al., 1985).

Beyond the ISM, CEs of evolved stars also exhibit phosphorus chemistry, albeit with different molecular inventories and formation conditions. These environments display a more diverse, although still limited, phosphorus chemistry. The first P-bearing molecule identified in such environments was CP, detected in the carbon-rich shell of IRC+10216 (GUÉLIN et al., 1990). This discovery was followed over the next decades by the detection of additional PBSs, including PN, CCP, HCP, PH_3, and SiP, most of which were also found in IRC+10216 (MILAM et al., 2008; AGÚNDEZ et al., 2008; TENENBAUM; ZIURYS, 2008; AGÚNDEZ et al., 2014; KOELEMAY et al., 2022). Moreover, PH_3, PN and HCP were also observed in the protoplanetary nebula CRL2688 (MILAM et al., 2008; TENENBAUM; ZIURYS, 2008; MCGUIRE, 2022; AGÚNDEZ et al., 2014). PO was first identified as an interstellar molecule within the oxygen-rich circumstellar envelope of the hypergiant VY CMa (TENENBAUM; WOOLF; ZIURYS, 2007), and was later detected in various molecular clouds (BERNAL; KOELEMAY; ZIURYS, 2021; BERGNER et al., 2019; RIVILLA et al., 2020). Since its initial detection, PO has also been observed in other oxygen-rich CEs, including those surrounding NML Cyg, IK Tau, and R Cas, where it frequently coexists with PN (TENENBAUM; WOOLF; ZIURYS, 2007). The detection of PO is particularly significant, as it marks the first, and thus far the only, identification in space of a molecule containing a direct P–O bond (LEFLOCH et al., 2016; TENENBAUM; WOOLF; ZIURYS, 2007; RIVILLA et al., 2016; CONCEPCIÓN et al., 2021; ZIURYS, 2024). Notably, PN and PO almost always appear together, suggesting a potential link between their formation mechanisms (BERNAL; KOELEMAY; ZIURYS, 2021; ZIURYS, 2024).

PO and PN are generally considered the main gaseous reservoirs of phosphorus in the ISM (THORNE et al., 1984; AGÚNDEZ; CERNICHARO; GUÉLIN, 2007; BECK et al., 2013; LEFLOCH et al., 2016; ZIURYS, 2024). Although their abundances appear to be comparable in many observed environments, several studies suggest that PO is typically more abundant than PN (RIVILLA et al., 2016; LEFLOCH et al., 2016; RIVILLA et al., 2018; BERGNER et al., 2019). Observational data often report [PO]/[PN] abundance ratios greater than 1 (LEFLOCH et al., 2016; HAASLER et al., 2022; FERNÁNDEZ-RUZ; JIMÉNEZ-SERRA; AGUIRRE, 2023), yet current astrochemical models frequently fail to reproduce this trend, generally predicting ratios below unity, especially in regions influenced by cosmic rays (JIMÉNEZ-SERRA et al., 2018; CHANTZOS et al., 2020; SIL et al., 2021; FERNÁNDEZ-RUZ; JIMÉNEZ-SERRA; AGUIRRE, 2023). This mismatch highlights the complexity of phosphorus chemistry in the ISM and suggests that energetic processes such as UV radiation and cosmic ray interactions may play a significant role in shaping the observed abundances (TURNER; BALLY, 1987; ZIURYS, 1987; JIMÉNEZ-SERRA et al., 2018).

In addition to the limited number of detections, uncertainties in reaction rate coefficients and possible gaps in the currently available chemical reaction networks may hinder accurate

modeling of the formation and destruction pathways of these species (FERNÁNDEZ-RUZ; JIMÉNEZ-SERRA; AGUIRRE, 2023). Advancing our understanding of the underlying chemical processes is therefore essential to bring together observational data with theoretical predictions. Furthermore, progress in characterizing the astrochemical behaviour and galactic distribution of phosphorus remains constrained by the scarcity of laboratory spectroscopic data for PBMs, posing ongoing challenges for their detection and study. Table 1 summarizes the detections of the PBSs relevant to the present work, considering the reactions chosen to be studied, along with their corresponding sources. The references of these detections can be found throughout the text.

Table 1 – PN, PO and CP in astrochemical environments.

Species	Source type
PN	C-rich giant branch envelope
	O-rich giant branch envelope
	Hypergiant envelope
	Clouds: high-mass star formation
	Clouds: low-mass star formation
	Protoplanetary nebula
PO	O-rich giant branch envelope
	Hypergiant envelope
	Clouds high-mass star formation
	Clouds low-mass star formation
CP	C-rich giant branch envelope

Source: Adapted from (ZIURYS, 2024).

The following section presents a review of the selected reactions involving PN and PO investigated in this work, with particular emphasis on their mechanisms and rate coefficients under interstellar conditions.

2.2.2.1 Review on the selected reactions

Regarding the $P(^4S) + O_2(^3\Sigma_g^-) \rightarrow O(^3P) + PO(^2\Pi)$ reaction, previous determinations of its rate coefficients (HUSAIN; NORRIS, 1977; HUSAIN; SLATER, 1978; CLYNE; ONO, 1982; HENSHAW et al., 1987) generally lacked temperature dependence and varied significantly, with differences of over an order of magnitude. This process has also been recently experimentally revaluated taking into account the temperature dependence of its rate coefficients (DOUGLAS et al., 2019), where a rate coefficient of $(2.70 \pm 0.12) \times 10^{-13} cm^3 s^{-1}$ has been obtained at room temperature. However, in this latter work, the quartet potential energy surface, which may also contribute to the overall rate was not assessed. Besides that, the B3LYP functional was employed, and this one is also known for its poor performance in predicting barrier heights (ZHAO; TRUHLAR, 2008b; PEVERATI; TRUHLAR, 2012). It is worth pointing out though that the final reported rate was adjusted to experimental data.

$N(^4S) + PN(^1\Sigma^+) \rightarrow N_2(^1\Sigma_g^+) + P(^4S)$ reaction, it has already been shown by Aota and Aikawa (2012) that in solar-type star forming regions, atomic nitrogen is very important to explain the chemistry of PN, being necessary that the maximum temperature in shocks between both species has to be larger than 4000 K (LEFLOCH et al., 2016; DOUGLAS; GOBRECHT; PLANE, 2022). This is interesting since in these high temperature environments, collision $N(^4S) + PN(^1\Sigma^+)$ may be fast and could be important, given the abundance of atomic nitrogen. This process can indeed be found in astrochemical databases (MILLAR et al., 2024; WAKELAM et al., 2024). Nevertheless, the employed rate coefficient of $1.0{\times}10^{-18}$ cm^3 s^{-1} (with no temperature dependence) was suggested by Millar, Bennett and Herbst (1987) by arguing that it should possess an activation energy since PN molecule is stable. However, this reference only considers its impact on the very low temperatures of dense clouds. Although this is a reasonable suggestion for such cold environments, one can expect a rapid increase for higher temperatures, depending on the value of the activation energy. Therefore, to study its contribution to PN destruction in circumstellar envelopes and shocks regions is an important task to be explored.

When it comes to the most commonly used neutral-neutral reactions in astrochemical databases that explain the formation of PN, proposed by Millar, Bennett and Herbst (1987), one can mention $N(^4S) + PO(^2\Pi) \rightarrow O(^3P) + PN(^1\Sigma^+)$, $N(^4S) + PO(^2\Pi) \rightarrow P(^4S) + NO(^2\Pi)$ and $N(^4S) + PH(^3\Sigma^-) \rightarrow H(^2S) + PN(^1\Sigma^+)$. However, these processes have not been experimentally probed, and the rate coefficients employed in the models are estimations based on similar ones, such as N+NH $\rightarrow$ N_2+H (SMITH; HERBST; CHANG, 2004), which in turn had its rate constant already studied theoretically and experimentally (CARIDADE et al., 2005; HACK; WAGNER; ZASYPKIN, 1994; MILLER et al., 1985). Reactions $N(^4S) + PO(^2\Pi) \rightarrow O(^3P) + PN(^1\Sigma^+)$ and $N(^4S) + PO(^2\Pi) \rightarrow P(^4S) + NO(^2\Pi)$ recently received computational corroboration (SOUZA; SILVA; GALVÃO, 2021; SILVA et al., 2025).

Therefore, a better understanding of several other astrochemical collisions involving PO and PN with abundant and reactive species available in space (such as atomic carbon, nitrogen, and oxygen) is essential to obtain a better description of the abundances of these molecules in different regions of the ISM. This is why the $P(^4S) + NH(^3\Sigma^-) \rightarrow H(^2S) + PN(^1\Sigma^+)$ and $N(^4S) + PH(^3\Sigma^-) \rightarrow H(^2S) + PN(^1\Sigma^+)$ processes were selected to be studied in this work. A recent work by Douglas, Gobrecht and Plane (2022) estimated the rate coefficients for several reactions involving PO and PN using collision capture rates methodology and with long-range transition state theory (LR-TST) (GEORGIEVSKII; KLIPPENSTEIN, 2005), which is an important contribution to this endeavour. However, in the present work the aim is to enhance the knowledge regarding these processes by performing accurate calculations on their energies and rate coefficients. It is important to mention that, reaction $P(^4S) + NH(^3\Sigma^-) \rightarrow H(^2S) + PN(^1\Sigma^+)$ which is also potentially relevant in the transformation of atomic phosphorus into molecular species is not available in the astrochemical databases (WAKELAM et al., 2024; MILLAR et al., 2024).

In the context of the CPN system, Jiménez-Serra et al. (2018) highlighted that the collisions $N(^4S) + CP(^2\Sigma^+) \rightarrow C(^3P) + PN(^1\Sigma^+)$ and $P(^4S) + CN(^2\Sigma^+) \rightarrow C(^3P) + PN(^1\Sigma^+)$, initially proposed by Agúndez, Cernicharo and Guélin (2007), have highly uncertain rate constants, and incorporating these reactions into astrochemical models has minimal impact on the overall results. In a more recent study, Fernández-Ruz, Jiménez-Serra and Aguirre (2023) estimated the rate coefficients for these reactions by adopting the parameters of the analogous reaction N+CN $\rightarrow$ N_2+C, based on the assumption that nitrogen and phosphorus exhibit comparable chemical behaviour due to their similarities. However, these assumptions might not fully describe the relevance of these processes.

The following section highlights the importance of investigating neutral-neutral reactions in astrochemical environments, particularly through theoretical approaches, not only to better understand the observed abundances of detected species, but also to enhance the accuracy of astrochemical models across different astrophysical contexts.

2.3 Neutral-neutral reactions in astrochemical environments

Even though part of the reactions that occur in space involve ionized species, neutral-neutral reactions also play an important role. They are similar to the one shown in Equation 2.4, assuming that the process is exothermic (TIELENS, 2021).

$$A + B \rightarrow C + D + \Delta E. \tag{2.4}$$

These reactions are very important for the study of the formation and evolution of molecules in space. Mainly, they occur in molecular clouds, in which both density and temperature conditions (dense and cold regions, see Figure 1) can aid the formation and stabilization of more complex species. Low temperatures allow that reactions without an activation barrier (or with a very low one) may occur, while high densities increase the collision probability between the present species, making it more easily for chemical reactions to occur (HERBST et al., 1994; YAMAMOTO, 2017; TIELENS, 2021).

Reactions between neutral gaseous species can be exothermic or endothermic. They often have reaction barriers, due to the necessity of bond breaking, formation of transition states and molecular rearrangement processes. Due to the low temperatures present in space, such reactions are often important only if they are barrierless (or possess a low barrier). Therefore, the use of these reactions in chemical models demands careful considerations. In this context, theoretical and computational chemistry can be of great value, helping to search the presence or absence of reaction barriers. On the contrary, neutral–neutral reactions that involve radicals often occur without reaction barriers, meaning that they can be fast even at low temperatures. However, it is important to mention that these are not rules. Each type of reaction must be individually

investigated, in order to obtain reliable results (SMITH; HERBST; CHANG, 2004; WAKELAM et al., 2010; AGÚNDEZ; WAKELAM, 2013; TIELENS, 2021; PUZZARINI, 2022).

In summary, the study of gas-phase neutral-neutral reactions in the ISM and in CEs is crucial for understanding the chemistry of space, the formation of stars and planets, and the potential emergence of life. The following section presents the theoretical background of computational chemistry and the methodologies applied in this work.

2.4 Computational chemistry

Computational chemistry is a powerful tool to aid and collaborate with experimental chemistry in solving chemical problems. This field of chemistry uses computer simulations and theoretical methods to study, analyse, calculate and predict atomic and molecular properties, such as molecular structure and energetics, reaction mechanisms, electronic structure, rate constants and others.

2.4.1 The Born-Oppenheimer approximation

For molecular systems, in order to perform quantum calculations it is necessary to develop and apply approximations. An important one used throughout the calculations of this work, is the Born-Oppenheimer approximation (BORN; OPPENHEIMER, 1927). This approximation considers that the nuclei can be fixed in well-defined positions to solve the electronic problem. The nuclei are admitted to be much heavier than the electrons, being considered stationary (no kinetic energy and mutual repulsions constant), while the electrons move in the field that these create. Therefore the Schrödinger's equation is solved for the electrons separately, being the problem minimized for the electronic part independently (BORN; OPPENHEIMER, 1927; LEVINE, 2000; SZABO; OSTLUND, 1989).

It is important to mention that the nuclei are considered stationary only when one is solving the electronic part of the Schrödinger's equation. The motion of the electrons still depend parametrically on the nuclear coordinates, as the total electronic energy for a certain arrangement of the nuclei must include the constant nuclear repulsion and the nuclei-electrons attraction. After calculating the electronic energy, it is possible to calculate the vibration and rotational energies of the nuclei (for example, the zero point energy (ZPE)). Therefore, the Born-Oppenheimer approximation provides a way to treat electrons and nuclei separately (LEVINE, 2000; SZABO; OSTLUND, 1989).

After finding the electronic wavefunction and the electronic energy (taking into account the Born-Oppenheimer approach), several properties can be extracted, such as the equilibrium geommetry, ionization potential, electron affinity, and so on. Transition states structures, which are very important to the present work, can also be determined (ATKINS; FRIEDMAN, 2005). These results constitute the basis for computational studies of molecular structure and reactivity.

2.4.2 The Hartree-Fock (HF) method for electronic structure calculation

Aiming to make the calculation of electronic energies more viable for polyelectronic systems, the suitable way to start is finding a well behaved wave function. The first step is based on finding an approximate one using the Hartree-Fock (HF) procedure. Within this approach, which is an *ab initio* one, the electronic repulsion of the various electrons that constitute the system is considered as an average potential. This approximation allows each electron to be solved in an individual way. Therefore, it is important to observe that the HF procedure does not consider the electron correlation (ATKINS; PAULA, 2015; LEVINE, 2000; ATKINS; FRIEDMAN, 2005).

To fully describe an independent electron, besides its spatial distribution, it is necessary to specify its spin. The combination of these two elements leads to its spin-orbital($\chi(x)$), in which "x" indicates both space (r) and spin coordinates (ω), as shown in Equations 2.5 and 2.6 (LEVINE, 2000; SZABO; OSTLUND, 1989).

$$\chi(x) = \psi(r)\alpha(\omega) \tag{2.5}$$

$$\chi(x) = \psi(r)\beta(\omega), \tag{2.6}$$

in which, $\alpha(\omega)$ refers to spin up and $\beta(\omega)$ to spin down.

The total wave function, disregarding the antisymmetry principle will be the product of these one electron spin-orbitals (Equation 2.7) (LEVINE, 2000; SZABO; OSTLUND, 1989)

$$\psi^{HP}(x_1, x_2, ...x_N) = \chi_i(x_1)\chi_j(x_2)...\chi_k(x_N). \tag{2.7}$$

Here, HP is the Hartree product and "N" is the number of electrons of the system. Observing the fact that the inherent instantaneous electronic repulsion is disregarded.

The HP is not antisymmetric, and the interchange between two electrons does not change the sign of the wave function. To solve this problem, Slater determinants are used, which can be expressed as:

$$\psi(x_1, x_2, ..., x_N) = (N!^{-1/2}) \begin{vmatrix} \chi_i(x_1) & \chi_j(x_1) & ... & \chi_k(x_1) \\ \chi_i(x_2) & \chi_j(x_2) & ... & \chi_k(x_2) \\ \vdots & \vdots & & \vdots \\ \chi_i(x_N) & \chi_j(x_N) & ... & \chi_k(x_N) \end{vmatrix} \tag{2.8}$$

in which $N!^{-1/2}$ is a normalization factor.

In order to obtain the most realistic spin-orbitals, an initial guess function must be variationally optimized such as to yield the lowest total energy of the system. This optimization is performed with the constraint that the spin-orbitals must be orthonormal (ATKINS; FRIEDMAN, 2005; LEVINE, 2000). After applying the variational principle, taking into account the orthonormality constraint, the HF Equation is achieved:

$$f(i)\chi_i(r_i) = \varepsilon_i\chi_i(r_i). \tag{2.9}$$

In Equation 2.9, $f(i)$ is called Fock operator. This operator contains terms that mathematically express the electron kinetic energy, the potential energy between this electron and the nuclei of the system, the mean field created by the other electrons, and the effects of correlation between the electrons with the same spin. Since this operator depends on all electrons, its detailed form relies on all the individual spin-orbitals, meaning that it depends on an initial guess shape for them. Therefore, one is dealing with a numerical and iterative method. The process is then repeated using the newly found wave function, until the energies and wave function stop changing, reaching the so-called self-consisted field (SCF), within a convergence criteria previously established (ATKINS; FRIEDMAN, 2005; ATKINS; PAULA, 2015).

The HF procedure is the basis for electronic structure calculation and it can be used to approximately solve numerically the problem of atoms. However, for molecules, due to the higher number of electrons, this would be computationally expensive. Therefore, a modification of this procedure needed to be applied. In 1951, C. C. J. Roothaan and G. G. Hall proposed that the spin-orbitals can be expanded as a linear combination of known basis functions (Equation 2.10) (ATKINS; FRIEDMAN, 2005; LEVINE, 2000).

$$\chi(r_i) = \sum_{\mu=1} C_{\mu i}\chi_\mu. \tag{2.10}$$

The basis are chosen to be atom-centered functions, similar to atomic orbitals. This procedure is called linear combination of atomic orbitals (LCAO). With this procedure, the problem of calculating the wave functions is reduced to finding the coefficients $C_{\mu i}$. This is also an iterative approach, since the Fock operator depends on the yet unknown coefficients (ATKINS; FRIEDMAN, 2005; LEVINE, 2000).

Although the HF method, combined with the Roothaan–Hall contribution, is extremely important for quantum calculations, it does not take into account electron correlation. This means that the HF energy can, and should, be improved by other methodologies that include these inherent instantaneous Coulombic interactions between electrons. In addition, the Slater determinant used in HF is not always an eigenfunction of the $\hat{S}^2$ operator (the square of the total spin angular momentum operator), which may lead to spin contamination (LEVINE, 2000; SZABO; OSTLUND, 1989).

2.4.3 Density Functional Theory (DFT)

Density Functional Theory (DFT) is another calculation approach widely used to calculate electronic energies and properties of systems that possess many atoms. Differently from the wave-function (ψ) based methods, DFT does not try to achieve the molecular wave function. Insted, it tries to obtain the electron density (ρ) and from this, it calculates the molecular electronic energy (ATKINS; FRIEDMAN, 2005; LEVINE, 2000).

As it is well known, electrons are indistinguishable. Therefore, the probability density for finding an electron near a point (x, y, z) is given by Equation 2.11.

$$\rho(r) = N \sum_{allspins} \int ... \int |\psi(r, r_2, ..., r_N, m_{s1}, m_{sN})|^2 dr_2 ... dr_N, \tag{2.11}$$

in which $dr = dxdydz$ and m_s are their respective spins. In this Equation, ψ must be antisymmetric with respect to electron exchange, according to the antisymmetry principle. By focusing on the electron density (ρ) rather than the wavefunction, DFT can provide a much faster way of calculating the properties of the systems of interest. When integrated over all space this electron density provides the total number of electrons, N (Equation 2.12) (LEVINE, 2000; CRAMER, 2004).

$$N = \int \rho(r) dr. \tag{2.12}$$

In 1964, P. Hohenberg and W. Kohn stated that the ground-state electronic density, only by itself is enough to determine the ground-state energy of a system (the Hohenberg–Kohn existence theorem (HOHENBERG; KOHN, 1964)). Although this is a strong statement, it lacked practical use, as it does not provide a way to obtain the energy from the density. In this spirit, considering this theorem, W. Kohn and L. J. Sham derived equations (Kohn–Sham self-consistent field methodology (KOHN; SHAM, 1965)) that made the Hohenberg-Kohn theorem practical to calculate electronic structure. They demonstrated that the exact ground state electronic energy can be written in the form of Equation 2.13 (ATKINS; FRIEDMAN, 2005; CRAMER, 2004; LEVINE, 2000)

$$E[\rho] = -\frac{\hbar^2}{2m_e} \sum_{i=1}^{N} \int \chi_i^*(r_1) {\nabla_1}^2 \chi_i(r_1) dr_1 - j_0 \sum_{I=1}^{M} \frac{Z_I}{r_{I1}} \rho(r_1) dr_1 + \frac{1}{2} j_0 \int \frac{\rho(r_1)\rho(r_2)}{r_{12}} dr_1 dr_2 + E_{XC}[\rho], \tag{2.13}$$

in which $E[\rho]$ is the exact ground state electronic energy of an N-electron system, and the Kohn-Sham (KS) orbitals are the one-electron spin orbitals $\chi_i (i = 1, 2, ..., N)$. M is the number of nuclei with atomic number Z_I and $j_0 = \frac{e^2}{4\pi\varepsilon_0}$ (ATKINS; FRIEDMAN, 2005).

The first term on the right of Equation 2.13 represents the kinetic energy of electrons in a non-interacting reference system; the second is the electron–nucleus attraction; the third

corresponds to the classical Coulomb interaction between the total charge distribution at r_1 and r_2; and finally, the last term is the exchange–correlation energy of the system. Of all these terms, E_{XC} is the only one that does not possess an exact known form. Within the Kohn–Sham formalism, orbitals are introduced in order to evaluate the kinetic energy of the non-interacting system, whereas the missing contributions from the interacting system are included in the exchange–correlation functional. This functional depends on the electronic density and contains all the unknown quantities that emerged during the derivation. Exchange–correlation functionals are therefore a fundamental concept in DFT (ATKINS; FRIEDMAN, 2005; LEVINE, 2000).

DFT is suitable for treating systems such as molecular ones, including reaction pathways, and systems that demand an extensive exploratory study. For this reason it is widely used, although sometimes only as a starting point, to study chemical reactions and molecular dynamics. Nevertheless, although it has the advantages of speeding up the calculations of many-electron systems, the accuracy of the results might sometimes not be so reliable. For instance, for reaction barriers, DFT might not provide very accurate results. Therefore, theoretical chemists are always trying to develop new exchange–correlation functionals that can provide more accurate results. It is worth noting that most DFT functionals have a higher computational cost than the HF method, but are still considerably less demanding than correlated post-HF approaches such as coupled-cluster. For this reason, DFT calculations are often employed not to provide final results, but as starting points for more sophisticated methods capable of yielding more robust electronic energies (CRAMER, 2004; LEVINE, 2000; JENSEN, 2007).

2.4.4 Post Hartree-Fock (HF) electronic structure calculation methods

In electronic structure calculations, one calculates the distribution of electrons in the system of interest. For this purpose, different methods and theories can be applied, such as the well known and fundamental HF theory, already mentioned. However, the HF method provides solutions to the Schrödinger equation in which the real electron–electron interaction is replaced by an average interaction. So, the difference in energy between the HF one and the exact energy is the electron correlation (EC) energy. In order to avoid errors, one must consider this fact. To provide better aproximations and better results, post-HF methods, such as Configuration Interaction (CI), Coupled Cluster (CC), Multi-Configuration Self-Consistent Field (MCSCF) and Multi-reference Configuration Interaction methods (MRCI), which take into account electron correlation can and should be applied, therefore obtaining more accurate results when it comes to molecular properties (CRAMER, 2004; LEVINE, 2000; JENSEN, 2007).

To include the instantaneous electron correlation, one can introduce the interelectronic distances in the wave functions, as in the explicitly correlated approaches (although this can only be made for systems with a small number of electrons). Alternatively, one can also add the contributions of other electron configurations, mixing the ground state determinant with higher order ones. The best way to deal with this is to build a wave function as a linear

combination of multiple determinants (CRAMER, 2004; LEVINE, 2000; JENSEN, 2007). A generic multi-determinant guess wave function can be written as Equation 2.14:

$$\psi = c_0\psi_{HF} + c_1\psi_1 + c_2\psi_2 + ..., \tag{2.14}$$

in which the coefficients "c" are related to each determinant in the expansion. It is important to mention that this expansion procedure does not have to include the HF determinant. However, since the HF wave function is reasonable, it is a wise procedure to consider it as the first term of the expansion. Electron correlation methods differ in how they calculate the coefficients in front of the other determinants. In the next subsections, the theories of the calculation methods used in this work will be discussed, in a more qualitative way.

2.4.4.1 Configuration Interaction (CI)

In a conventional HF-SCF procedure, only occupied orbitals contribute to the total energy, that is, virtual orbitals are neglected. However, one can treat all orbitals in the same way, during the optimizing and relaxing process, therefore, all orbitals are taken into account. A pure HF calculation cannot describe the dissociation of molecules into open-shell fragments, therefore it can not provide accurate PESs, which for the present work is essential (CRAMER, 2004; SZABO; OSTLUND, 1989).

If multiple Slater determinants are used (see Equation 2.14), with the single-determinant HF wavefunction serving as the reference, the additional determinants can be classified based on the number of electrons promoted from occupied to virtual orbitals. For instance, a singly excited determinant is the one in which a single electron in one occupied spin-orbital is promoted to a virtual spin-orbital; in a doubly excited determinant two electrons are promoted, and so on. The expansion coefficients of Equation 2.14 are determined by requiring that the energy should be a minimum. The MOs used for building the excited Slater determinants are taken from a previous HF calculation and held fixed (JENSEN, 2007; ATKINS; FRIEDMAN, 2005).

Rewriting Equation 2.14 as Equation 2.15:

$$\psi = c_0\psi_{HF} + \sum_{i}^{occ.}\sum_{r}^{vir.} c_i^r\psi_i^r + \sum_{i<j}^{occ.}\sum_{r<s}^{vir.} c_{ij}^{rs}\psi_{ij}^{rs} + ..., \tag{2.15}$$

where i and j are occupied MOs in the HF procedure; r and s are virtual MOs in the ψ_{HF}, and the sum leads to the others determinants created by exciting electrons from one occupied orbital into a virtual one. Analysing Equation 2.15, it can be concluded that the first summation includes all possible single excitations, the second all the double excitations, and so on. The problem is then minimized in finding the expansion coefficients for each excited configuration that it contains. It is worth noticing that in order to preserve the correct spin state, the CI method employs Configuration State Functions as its basis, ensuring that the resulting wavefunction is properly adapted to the symmetry of the desired state (CRAMER, 2004).

In summary, in a Configuration Interaction (CI) approach, the single Slater Determinant, of the HF theory, is broaden in N-electrons ones, like the procedure mentioned previously (Equation 2.15). By doing so, one considers not only the energy of the ground state but also of the possible excited states of the system (CRAMER, 2004; ATKINS; FRIEDMAN, 2005).

A full configuration interaction calculation (full-CI) is the one that considers all possible excited configurations that can be taken from a single HF determinant. The problem is that, even for small systems, the number of determinants is high. Therefore, a full-CI calculation is unfeasible. The best way to deal with this problem is by using a truncated set of determinants, or by carrying out multi-reference configuration interaction (MRCI) calculations, which will be discussed later. It is important to mention that, within this approach, the energy of two noninteracting molecules is not twice the energy of one of them, that is, CI calculations are not size-consistent (SZABO; OSTLUND, 1989; CRAMER, 2004; ATKINS; FRIEDMAN, 2005).

A size-consistent method can be defined in different ways, such as: It is the one in which the energy of a many-electron system is proportional to the number of electrons N in the limit of $N \rightarrow \infty$ (ATKINS; FRIEDMAN, 2005); it is the one in which the approximations employed in order to calculate energies vary linearly with the number of particles as the size of the system increases (SZABO; OSTLUND, 1989); and it is the one for which the energy increases in proportion to the size of the molecule. A special case of size consistency is size consistency for infinitely separated systems, i.e., the method provides the energy of a system of two or more infinitely separated molecules as equal to the sum of the energies of the individual molecules (LEVINE, 2000).

2.4.4.2 Multi-Configuration Self-Consistent Field (MCSCF)

Considering the limitations of a CI calculation, there are further improvements that can be made in order to limit the CI expansion, such as determining the orbitals used within the expansion. A further step would be to optimize the unknown coefficients of Equation 2.14 at the same time as the coefficients $C_{\mu i}$ of Equation 2.10. The wave function constructed within this theory is called a multiconfiguration self-consistent field (MCSCF) function. The guess wave function, possessing only a few determinants, is then optimized for a combination of configurations, considering not only the expansion coefficients but also the orbitals. The selection of the orbitals and configurations that should be included in an MCSCF calculation depends on the chemical system being studied (ATKINS; FRIEDMAN, 2005; CRAMER, 2004; JENSEN, 2007; SZABO; OSTLUND, 1989). This methodology is particularly important when dealing with excited states, but it is also crucial for ground states with significant multireference character. Such situations may arise in relatively simple systems, like ozone, as well as in more complex molecules, such as transition metal compounds.

A further improvement is the Complete Active Space Self-Consistent Field (CASSCF) method. The selection of configurations is done by partitioning the molecular orbitals into active

and inactive spaces. Within this approach, the determinants included in the calculations are configurations that come from all possible ways of distributing the active electrons over the active orbitals. The MCSCF active space choices are commonly abreviated as (m,n), where "m" stands for the number of electrons and "n" the number of orbitals Therefore, if one decides to choose all possible configurations, that is, allowing all possible arrangements of electrons to enter into the MCSCF calculation, then that means that the complete active space (CAS) was selected, being this calculation called CASSCF (CRAMER, 2004; ATKINS; FRIEDMAN, 2005).

The best procedure is therefore to allow all possible arrangements of electrons to take part in the MCSCF calculations. However, this choice has to be made wisely, since CASSCF simultaneously optimizes all the coefficients in Equation 2.14 and all the molecular orbitals, meaning that the greater the system, the greater the computational effort. The proper selection of symmetry can aid in reducing the complexity of the calculations that need to be performed (CRAMER, 2004; JENSEN, 2007). Nevertheless, the use of symmetry constraints may become undesirable along a reaction coordinate, where molecular symmetry can be reduced.

In summary, in a CI calculation the molecular orbitals are determined in an initial HF-SCF calculation and held fixed in the subsequent CI calculation (ATKINS; FRIEDMAN, 2005). It optimizes only the "c" coefficients of Equation 2.15, keeping the determinants and orbitals fixed. In a MSCSCF approach, and therefore in CASSCF, the calculation optimizes not only the "c" coefficients, but also optimizes the orbitals within each determinant as well. In CASSCF, each determinant has different orbitals, while in CI the orbitals are fixed.

2.4.4.3 Multireference Configuration Interaction (MRCI)

In multireference configuration interaction (MRCI), a set of reference configurations is created from a previous MCSCF calculation, in which excited determinants are constructed to be used in a CI calculation. It explicitly considers more than one reference configuration of electrons (ATKINS; FRIEDMAN, 2005). MRCI methods are used when the molecule has multireference character and its electronic structure cannot be captured by a single determinant.

The electron correlation effects are improved by including multiple determinants. The final MRCI wavefunction can include determinants that are singly, doubly and triply excited, depending on the type of MRCI calculation chosen. The logic for multireference configuration interaction is similar to the single reference CI. The difference is that instead of using the HF wave function as a reference, an MCSCF one is used. Therefore, in order to select the reference states, usually, one performs a CASSCF calculation (ATKINS; FRIEDMAN, 2005; CRAMER, 2004). If one wants to approximately include also the energy contribution due to quadruple excitations, this can be done by using the Davidson correction. The use of this correction reduces the size-consistency error (LEVINE, 2000).

MRCI is a very sophisticated, although computationally expensive, method of calculating the electronic structure of molecules. There are several enhancements that makes MRCI

methodology even more sophisticated. One can mention Davidson-corrected MRCI (MRCI+Q) and explicitly correlated MRCI (MRCI-F12) (SZALAY et al., 2012; SHIOZAKI; KNIZIA; WERNER, 2011). Usually, MRCI calculations are only used to deal with small systems, or refining the results obtained by other less computationally demanding ones. In summary, if one is dealing with a small system and aims to obtain detailed reaction mechanisms, including finding transition states and reaction pathways, MRCI is one of the best choices of methodology. Another important aspect to be mentioned is that, since multiple configurations are considered, MRCI is very powerful when one is dealing with excited states.

Since in this work, transition and excited states are important, mainly because of the strong electron correlation effects, MRCI methodology is one that should be considered essential. Also, since in this work less computationally demanding calculation methods are used, MRCI results are very efficient for benchmarking and verifying the accuracy of the other theoretical models employed.

2.4.4.4 Coupled Cluster Theory (CC)

Coupled Cluster (CC) theory (ČÍŽEK, 1966) is a single-reference method widely used for calculating the electronic structure of molecules. Its central idea is the introduction of the so-called cluster operator, which, in exponential form, connects the exact electronic wavefunction to the HF reference. In practical applications, truncations of this operator are required: the most common variants are CCSD and CCSD(T), where the effects of higher excitations are approximated (for example, quadruple excitations can be expressed in terms of products of doubles, and doubles in terms of singles) (ATKINS; FRIEDMAN, 2005; SZABO; OSTLUND, 1989).

CC calculations start with a reference (usually a HF one), and then build a more accurate wavefunction by applying excitation operators. The cluster operator can include single (S), double (D), triple (T) and even higher excitations. This procedure, therefore, goes beyond the reference configuration. CC wavefunctions are expressed as an exponential operator acting on the reference wavefunction:

$$\psi = e^{T}\psi_{HF}, \tag{2.16}$$

in which ψ is the exact nonrelativistic ground-state molecular electronic wave function, ψ_{HF} is the normalized ground-state HF wave function, and T is the cluster operator and it is equal to T=$T_1 + T_2 + ... + T_n$, where n is the total number of excitations. The effect of the cluster operator (T) is to provide a linear combination of Slater determinants in which electrons from occupied spin-orbitals have been excited to virtual spin-orbitals (ATKINS; FRIEDMAN, 2005).

The one-particle excitation operator (T_1) and the two-particle excitation operator (T_2) can be defined, respectively as (LEVINE, 2000):

$$T_1\psi_{HF} = \sum_{a=n+1}^{\infty}\sum_{i=1}^{n} {t_i}^a {\psi_i}^a \text{and} \tag{2.17}$$

$$T_2\psi_{HF} = \sum_{b=a+1}^{\infty}\sum_{a=n+1}^{\infty}\sum_{j=i+1}^{n}\sum_{i=1}^{n-1} {t_{ij}}^{ab} {\psi_{ij}}^{ab}, \tag{2.18}$$

in which ${\psi_i}^a$ is a singly excited Slater determinant, ${\psi_{ij}}^{ab}$ is a doubly excited Slater determinant, and ${t_i}^a$ and ${t_{ij}}^{ab}$ are numerical coefficients. Similar definitions can be applied for T_3, ..., T_n. The limits of Equations 2.17 and 2.18 are chosen aiming to include all possible single and double excitations. When T_1 and T_2 (or other higher order T) operates on a ψ_{HF} that contains both occupied and virtual spin-orbitals, the resulting sum contains only determinants with excitations from those occupied spin-orbitals. ${T_1}^2\psi_{HF}$ contains only doubly excited Slater determinants, and ${T_2}^2\psi_{HF}$ only quadruply excited determinants (LEVINE, 2000).

In Equation 2.16, the exponential operator e^T is defined by the Taylor-series expansion (ATKINS; FRIEDMAN, 2005; LEVINE, 2000):

$$e^T = 1 + T + \frac{1}{2!}T^2 + \frac{1}{3!}T^3 + ... = \sum_{k=0}^{\infty}\frac{T^k}{k!}. \tag{2.19}$$

The effect of the e^T operator is to express ψ as a linear combination of Slater determinants that include ψ_{HF} and all possible excitations of electrons from occupied to virtual spin-orbitals (LEVINE, 2000).

CC theory possesses a few approximations. Among them, one is that, instead of using a complete set of basis functions, a finite set must be used in order to express the spin-orbitals in the SCF wave function. Other approximation is that, instead of including all the operators, one approximates the operator T by including only a few. Theory and practice demonstrated that the most important contribution to T is made by T_2 (LEVINE, 2000). Since,

$$e^{T_2} = 1 + T_2 + \frac{1}{2}{T_2}^2 + ..., \tag{2.20}$$

the resulting wave function contains determinants with double substitutions, quadruple ones, hextuple ones, and so on. The quadruple excitations are produced by the operator $\frac{1}{2}{T_2}^2$, so the coefficients of the quadruply substituted determinants are determined as products of the coefficients of the doubly substituted ones.

The key of CC theory is the fact that the exponential of T can be truncated. Therefore, If T= T_2, one only has the double-excitation operator. One important fact is that CC calculations are size-extensive, that is, the energy scales linearly with the size of the system. When compared to other Post-HF methods, CC theory, therefore, is more suitable for large molecules systems. Although at a higher computational cost. It can be applied in the study of reaction mechanisms

(reaction pathways, transition states and barriers), being an important ally in the study of chemical reactions (LEVINE, 2000; CRAMER, 2004; JENSEN, 2007).

CC theory with Single and Double excitations (CCSD) is a variant commonly used. If one adds a perturbative correction (corretion T), CCSD method becomes CCSD(T) (BARTLETT, 1989; BARTLETT et al., 1990; RAGHAVACHARI et al., 1989; ADLER; KNIZIA; WERNER, 2007; KNIZIA; ADLER; WERNER, 2009). CCSD(T)calculations provide very accurate results for correlation energies (LEVINE, 2000).

After presenting the theoretical background of the calculation methods and before introducing key concepts in chemical kinetics, the following section discusses the fundamentals of atomic and molecular term symbols, briefly along with molecular symmetry. These concepts are essential for interpreting electronic structure and, as will be seen later, for determining which electronic states should be considered when constructing the potential energy surfaces for the collisions investigated in this work.

2.5 Atomic/molecular term symbols and molecular symmetry

An atomic electron configuration can give rise to multiple electronic states, as different combinations of magnetic (m_l) and spin (m_s) quantum numbers may satisfy the Pauli Exclusion Principle. For example, in the ground-state configuration of carbon ($1s^2 2s^2 2p^2$), the two 2p electrons can occupy different orbitals and spin states, resulting in distinct energy levels due to electron–electron repulsion. These states are more precisely described by determining the total orbital angular momentum (L) and total spin (S), which are then combined vectorially to yield the total angular momentum (J). This approach, known as Russell–Saunders coupling, leads to the atomic term symbol (equation 2.21) (MCQUARRIE; SIMON, 1997; LEVINE, 2000):

$$^{2S+1}L_J, \tag{2.21}$$

in which $2S+1$ is the spin multiplicity and the total angular momentum J is given by $J = L+S$. The values of L are represented by the following letters: $L = 0 \rightarrow S$, $1 \rightarrow P$, $2 \rightarrow D$, $3 \rightarrow F$, $4 \rightarrow G$, etc. Table 2 shows some examples of term symbols for various electron configurations (LEVINE, 2000).

Table 2 – Possible term symbols for some electron configurations.

Electron configuration	Term symbol
s^1	^2S
p^1	^2P
p^2, p^4	^1S, ^1D, ^3P
p^3	^2P, ^2D, ^4S
p^1, p^5	^2P

To determine the lowest energy term from a given configuration, Hund's rule is applied: "For terms arising from the same electron configuration, the term with the largest value of S lies lowest; if there is more than one term with the largest S, then the term with the largest S and the largest L lies lowest" (LEVINE, 2000).

In linear molecules, term symbols follow a logic similar to that used in atoms, but they are based on the projection of angular momentum along the internuclear axis. In atomic systems, degenerate orbitals such as $2p_{+1}$, $2p_0$, and $2p_{-1}$ form a subshell. In molecular systems, these atomic orbitals can combine to generate molecular orbitals, which are grouped into shells. For example, the degenerate orbitals $2p_{\pm1}$ can combine to give rise to the π_u shell, or, depending on the phase combination, to the π_g shell in a molecule. The σ shell contains a single orbital and can accommodate up to two electrons, whereas shells like π, δ, and others contain two degenerate orbitals and can hold up to four electrons. The electronic configuration of a molecule is specified by indicating the number of electrons occupying each shell. For instance, the configuration $(\sigma_g 1s)^2(\pi_u 2p)^3$ indicates that the $\sigma_g 1s$ orbital is fully occupied with two electrons, while the $\pi_u 2p$ shell contains three electrons (LEVINE, 2000).

In diatomic molecules, the projection operator of the total orbital angular momentum along the internuclear axis, $\hat{L}_z$, commutes with the Hamiltonian, and its associated quantum number M_L can take the values $0, \pm1, \pm2, \ldots$. For one-electron systems, the corresponding molecular quantity is defined as $\Lambda \equiv |M_L|$ (MCQUARRIE; SIMON, 1997; LEVINE, 2000), and is associated with a spectroscopic term symbol that characterizes the electronic state, as shown in Table 3 (LEVINE, 2000).

Table 3 – Relationship between Λ and its corresponding spectroscopic term symbol

Λ	0	1	2	3	4
Letter	Σ	Π	Δ	Φ	Γ

For $\Lambda \neq 0$, the values $+\Lambda$ and $-\Lambda$ are degenerate due to symmetry. As in atoms, the total spin S is obtained by combining individual spins, and the multiplicity $2S + 1$ appears as a left superscript to the term symbol. Molecular terms are thus written as:

$$^{2S+1}\Lambda^{(\pm)}_{(g/u)}, \tag{2.22}$$

where $2S + 1$ is the spin multiplicity and Λ is the capital Greek letter corresponding to orbital angular momentum projection. The superscript $^+$ or $^-$ (only for Σ states) denotes symmetry under reflection through a plane containing the internuclear axis, and the subscript g (gerade) or u (ungerade) refers to parity under inversion through the molecular center, applicable only to homonuclear diatomic molecules (LEVINE, 2000).

These symmetry labels are critical for interpreting the behaviour of electronic states. In homonuclear diatomics, inversion through the center leaves the nuclear configuration unchanged, but the electronic wave function may change sign. Being a product of molecular orbitals, the

overall wave function must be either symmetric (gerade, g) or antisymmetric (ungerade, u). For Σ states ($\Lambda = 0$), a $^+$ or $^-$ superscript further distinguishes reflection symmetry. For instance, in Σ states, such as those involving σ orbitals, the wave function remains unchanged under reflection through a plane that includes the internuclear axis, which corresponds to a $^+$ symmetry label (MCQUARRIE; SIMON, 1997).

These symmetry considerations are also fundamental to quantum chemical calculations. Group theory allows the classification of molecular orbitals and electronic states based on the point group of the molecule. The use of symmetry-adapted linear combinations reduces the number of non-zero integrals and improves computational efficiency (MCQUARRIE; SIMON, 1997). The practical relevance of term symbols and molecular symmetry extends beyond electronic structure itself. These concepts underpin spectroscopic selection rules and the conservation of angular momentum in reactions, which are central to the Wigner–Witmer rules, which will be discussed in a later section.

After presenting the theoretical background of the electronic structure methods employed in this work, along with fundamental concepts of molecular symmetry and atomic and molecular term symbols, the following section will focus on key topics in Chemical Kinetics that are essential for understanding reaction mechanisms and computing rate constants.

2.6 Chemical kinetics

Chemical kinetics is a field within physical chemistry, fundamentally connected to the investigation of reaction mechanisms and the determination of rate constants for each step involved in these mechanisms (KLIPPENSTEIN; PANDE; TRUHLAR, 2014). Unlike thermodynamics, which addresses the feasibility and equilibrium position of a reaction, kinetics provides insights into the time evolution of a chemical system, therefore, it involves the quantitative analysis of the rate of a chemical reaction (OLIVEIRA et al., 2016).

Considering an hypothetical reaction of the form A+2B $\rightarrow$ 3C+D, the instantaneous rate of consumption of one of the reactants at a given moment is the derivative of the molar concentration of this reactant with respect to time. At the same time, the rate of formation of one of the products is the derivative of the molar concentration of the specific product in relation to time (ATKINS; PAULA, 2012). Thus, considering this hypothetical reaction:

$$\frac{d[D]}{dt} = \frac{1}{3}\frac{d[C]}{dt} = -\frac{d[A]}{dt} = -\frac{1}{2}\frac{d[B]}{dt}. \tag{2.23}$$

In the majority of chemical reactions, the reaction rate "v" is connected to the concentrations of the different chemical species present at time "t". The expression that relates "$v(t)$" to these concentrations is known as the rate law. The rate law of a reaction is often proportional to the reactants concentrations raised to certain powers. The power to which the concentration

of a given species is raised in the expression of the rate law is called the order of the reaction with respect in to that given species. The global order of a reaction is the sum of the individual orders of each species involved in the rate law (MCQUARRIE; SIMON, 1997; ATKINS; PAULA, 2012). An example would be:

$$v = k(T)[A]^a[B]^b, \tag{2.24}$$

where, the temperature-dependent rate constant, $k(T)$, governs the reaction rate. Assuming first-order dependence on each reactant and that the process proceeds through a single bimolecular collision, the overall reaction order is 2 ($a = b = 1$). Although intermediates may be involved, a single effective collision between reactants is sufficient to justify this second-order behaviour, which applies to all reactions examined in this work. In general, rate laws must be determined experimentally, as they cannot be reliably inferred from the stoichiometry of the overall balanced equation. In the context of reaction mechanisms, an elementary reaction (or elementary step) is one that occurs in a single event, where bonds break and form simultaneously, without intermediates (OLIVEIRA et al., 2016). These steps are classified by molecularity (uni-, bi-, or termolecular), with higher molecularities being less probable due to the low likelihood of simultaneous collisions. When one step is much slower than the others, it acts as the rate-determining step, effectively controlling the overall reaction rate (MCQUARRIE; SIMON, 1997).

Conditions such as temperature and pressure are very important in order to perform chemical kinetics studies and predict reaction rates. The rate constant is specific to a particular reaction at a given temperature. This can be influenced, apart from temperature and pressure, by the presence of a catalyst (ATKINS; PAULA, 2012). In the ISM, for instance, dust particles can sometimes act as a catalyst for some reactions.

The units of a rate constant depend on the form of the rate law. For gas phase studies, concentrations are generally expressed in molecules cm^{-3}. Thus, the $k(T)$ values for bimolecular reactions would be expressed in terms of $cm^3 molecule^{-1} s^{-1}$ (ATKINS; PAULA, 2012). Since in this work only gas phase reactions are considered, this is the way in which the rate constants will be expressed.

Understanding the global reaction order provides a basis for exploring how reaction rates vary under different conditions. One of the most critical factors influencing the rate constant is temperature. The Arrhenius equation offers a fundamental framework to describe this temperature dependence and to connect kinetic behaviour with molecular energetics. The following section will briefly introduce this fundamental equation in kinetics studies.

2.6.1 Arrhenius equation: dependence on temperature

The rate at which chemical reactions occur is typically highly sensitive to temperature. This sensitivity arises because the reaction rate constant itself varies with temperature. In several cases, the temperature dependence of the rate constant can be approximated using the following empirical equation:

$$\frac{d \ln k}{dT} = \frac{AE}{RT^2}, \tag{2.25}$$

in which AE has units of energy. If AE in Equation 2.25 is temperature independent, it can be integrated to give:

$$k(T) = A \exp^{-AE/RT}, \tag{2.26}$$

in which A is the pre-exponential factor or frequency factor (which can have a weak dependence on temperature (FERNÁNDEZ-RAMOS et al., 2006)), AE is the activation energy, R is the gas constant and T is the temperature in Kelvin. In the 1880s, Svante Arrhenius observed that the influence of temperature on reaction rates was far greater than could be accounted for solely by changes in the translational energy of the reactants (ARRHENIUS, 1889). Therefore, he concluded that a successful reaction demands more than just a simple collision between the reacting species. For his contribution, Equation 2.26 is called Arrhenius Equation (MCQUARRIE; SIMON, 1997; LECCA, 2013).

The AE represents the minimum energy necessary for reactants to successfully undergo a chemical transformation. This process is commonly illustrated through an energy diagram, where the system evolves from reactants to products along a reaction coordinate. The reaction coordinate is generally multidimensional, capturing variations in bond distances and angles throughout the transformation. A more detailed discussion of this concepts will be presented in the following section (MCQUARRIE; SIMON, 1997; LEVINE, 2000).

Equation 2.26 can also be written as:

$$ln(k) = ln(A) - \frac{AE}{RT}. \tag{2.27}$$

Equation 2.27 indicates that plotting $\ln k$ against $1/T$ produces a straight line, where the intercept corresponds to $\ln A$ and the slope is equal to $-AE/R$ (MCQUARRIE; SIMON, 1997). This can be used to predict AEs. Although the Arrhenius equation is extensively used to estimate AEs of chemical reactions, deviations from linearity in $(\ln k)$ versus $(1/T)$ plots are often observed in certain systems. Such nonlinear behaviour arises because, in these cases, the rate constants exhibit more intricate temperature dependencies (MCQUARRIE; SIMON, 1997). In astrochemical studies (WAKELAM et al., 2024; MILLAR et al., 2024; MANION et al.,

2015) equation 2.26 is more commonly found in its modified version (Equation 2.28), which accomodates such deviations. Therefore, equation 2.28 is going to be used throughout this work.

$$k(T) = \alpha \left(\frac{T}{300}\right)^{\beta} \exp\left(-\gamma/T\right), \tag{2.28}$$

in which α, β and γ are parameters used to fit the rate constants more accurately to possible experimental results or calculated values.

This approach incorporates an additional temperature dependence in the pre-exponential factor, and the inclusion of the term $\left(\frac{T}{300}\right)^{\beta}$ does not have a direct justification from first principles. However, it can improve the fitting of the data obtained in kinetics studies of astrochemical gas-phase reactions, such as the ones studied in this work. Apart from that, equation 2.28 can capture variations in the system's behaviour that are not well described by the traditional Arrhenius formula, since, as already mentioned, some reactions might possess more complex temperature dependencies (HERBST; KLEMPERER, 1973; WOODALL et al., 2007; WAKELAM et al., 2024; MILLAR et al., 2024).

The exploration of an accurate and detailed potential energy surface is essential for studying reaction mechanisms and kinetics. The following section will address fundamental concepts and key aspects related to the exploration of such surfaces.

2.6.2 Potential-energy surfaces (PESs)

In order to describe how chemical reactions proceed at the molecular level, it is essential to analyze the potential energy surface (PES), which governs the motion of nuclei during a reaction.

Under a reasonable approximation, the electronic wave function effectively defines a PES that governs the motion of the nuclei. The PES is fundamental to the study of chemical kinetics and molecular reaction dynamics, as it describes how the electronic energy of a system varies with changes in nuclear configuration. It provides critical insight into molecular structure and chemical reactivity. Within the framework of the Born-Oppenheimer approximation (section 2.4.1), electronic and nuclear motions are treated separately, allowing the PES to be obtained by solving the electronic Schrödinger equation with the nuclei held fixed. This surface then governs the motion of the nuclei, which can be modeled using either classical or quantum mechanical approaches, depending on the system and the desired level of accuracy (COLLINS, 2002; JENSEN, 2007).

For a molecule with N atoms, the PES exists in a space of $3N$ Cartesian coordinates, but only $3N - 6$ (or $3N - 5$ for linear molecules) correspond to changes in the molecule, while the others are related to rotational and translational motions. These degrees of freedom are commonly expressed in internal coordinates such as bond lengths and angles (COLLINS, 2002; CRAMER,

2004; JENSEN, 2007). Each molecular structure (represented as a point on the PES) can be described by a position vector "X", defined as:

$$X \equiv (x_1, y_1, z_1, x_2, y_2, z_2, \ldots, x_N, y_N, z_N), \tag{2.29}$$

where x_i, y_i, z_i are the Cartesian coordinates of atom "i".

Stationary points on the PES (minima and saddle points) are critical for identifying stable species, intermediates, and transition states (TSs). These points correspond to zero gradients of the potential energy and are classified based on the eigenvalues of the Hessian matrix. A local minimum has all positive eigenvalues and corresponds to a stable structure with real vibrational frequencies. A first-order saddle point, with a single negative eigenvalue, represents a TS and defines the highest-energy point along the minimum energy path (MEP), also known as the intrinsic reaction coordinate (IRC) (CRAMER, 2004; JENSEN, 2007).

Choosing an appropriate coordinate system is crucial for TS optimizations, as it enhances convergence and reduces dependence on the initial guess (JENSEN, 2007). While locating minima is generally straightforward, identifying TSs is more complex and computationally demanding. Not all minima are connected by a TS, and proving the absence of such a connection is very difficult. Symmetry can assist in this process (section 2.5), particularly in reactions involving identical reactants and products, where the TS may exhibit distinct symmetry. Constraining the geometry accordingly and performing energy minimization can yield a stationary point, which is then characterized via frequency analysis. If the result is a higher-order saddle point, the associated imaginary modes indicate how to distort the structure toward a true TS or minimum. Because symmetric calculations are typically less computationally intensive, using symmetric structures as starting points is often an efficient strategy (JENSEN, 2007; CRAMER, 2004).

A central challenge in reaction dynamics is the need for a PES that covers a wide range of molecular geometries. Traditionally, global PESs are constructed by fitting analytical functions to extensive sets of *ab initio* energies, sometimes including gradients and Hessians, and refined with experimental data such as vibrational frequencies. However, for larger systems, generating a sufficiently dense grid becomes computationally expensive, making it necessary to focus on the chemically relevant regions of the surface. In this context, reaction path methods offer a more practical solution by restricting the analysis to a one-dimensional pathway, in which one examines lower-dimensional sections of the PES by fixing one or two internal coordinates (such as a bond length or bond angle) allowing for the construction of simplified energy curves or surfaces (JENSEN, 2007; CRAMER, 2004).

Rate constant calculations typically involve generating the PES, either a single surface for adiabatic (Born–Oppenheimer) processes or multiple coupled surfaces for non-adiabatic (non-Born–Oppenheimer) reactions like photochemical ones, followed by the computation of reaction dynamics. While dynamics traditionally use analytic PES representations, direct

dynamics ("on-the-fly") approaches are becoming more common (KLIPPENSTEIN; PANDE; TRUHLAR, 2014).

The long-range interaction between two molecules depends on the distance r between their centers and their relative orientations. In many cases, rotational averaging allows the interaction to be treated as a function of r alone (MCQUARRIE; SIMON, 1997). A typical intermolecular potential combines short-range repulsion and long-range attraction, collectively known as van der Waals (vdW) interactions. These represent non-bonded interactions between atoms or fragments not connected by covalent bonds and correspond to the nonpolar component of the total interaction energy, excluding contributions from permanent electrostatic charges.

At short interatomic distances, the interaction energy becomes strongly positive due not only to orbital overlap and electron–electron repulsion, but also to the repulsion between the nuclei. At intermediate distances, a weak attractive force arises from correlated fluctuations in the electron density, known as London dispersion, which scales as r^{-6}. Higher-order contributions, such as dipole–quadrupole and quadrupole–quadrupole interactions, decay even faster (e.g., r^{-8}, r^{-10}). Overall, vdW interactions dominate in nonpolar systems and can be modelled by the general expression below (MCQUARRIE; SIMON, 1997; JENSEN, 2007):

$$E_{\mathrm{vdW}}(r^{AB}) = E_{\mathrm{repulsion}}(r^{AB}) - \frac{C^{\mathrm{AB}}}{(r^{AB})^6}, \tag{2.30}$$

in which, E_{vdW} is the vdW interaction between fragments A and B separated by a distance r^{AB}. The term $E_{\mathrm{repulsion}}(r^{AB})$ accounts for the short-range repulsion due to orbital overlap and Coulomb repulsion between the electrons of the atoms, while the attractive component $-\frac{C^{\mathrm{AB}}}{(r^{AB})^6}$ describes dispersion forces. The factor (C^{AB}) depends on the electronic properties of A and B (JENSEN, 2007).

Although the repulsive part cannot be derived analytically from first principles, it must satisfy two conditions: (1) it vanishes as $r \to \infty$ and (2) it decays faster than the r^{-6} attractive term. The Lennard-Jones (LJ) potential (LENNARD-JONES; HALL, 1924) is a widely used empirical model that satisfies these criteria (MCQUARRIE; SIMON, 1997; JENSEN, 2007):

$$E_{\mathrm{LJ}}(r^{AB}) = \frac{C_{12}}{(r^{AB})^{12}} - \frac{C_6}{(r^{AB})^6}, \tag{2.31}$$

where C_{12} and C_6 are empirical constants obtained by fitting to experimental or theoretical data. These parameters characterize the strength and balance of repulsive and attractive forces and are related to the size and polarizability of the interacting particles.

When constructing a PES for an atom–diatom collision, such as those studied in this work, certain symmetry and spin conservation considerations must be taken into account. The following subsection discusses the Wigner–Witmer rules, which are essential for this type of approach.

2.6.2.1 Wigner-Witmer rules

Beyond computational advantages, symmetry also governs the accessibility of electronic states and transitions, especially in reactions involving open-shell species or excited atoms (section 2.5). In this context, the Wigner–Witmer rules offer a group-theoretical framework to correlate atomic states with resulting molecular term symbols under the assumption of adiabatic internuclear separation (WIGNER; WITMER, 1928b; HERZBERG, 2013).

The Wigner–Witmer rules, developed by E. Wigner and E.E. Witmer, apply group theory to predict the electronic states of diatomic molecules formed adiabatically from atomic combinations, with molecular symmetries described through irreducible representations. The application of the Wigner–Witmer conservation principles enhances the understanding of chemical reactions by correlating the electronic states of reactants and products based on angular momentum conservation and selection rules. These principles imply that symmetry and energy constraints govern reaction pathways, with the electronic energy serving as an effective potential that guides nuclear motion (WIGNER; WITMER, 1928b; SILVER, 1974).

In the context of these rules, chemical reactions can be classified as "allowed", "forbidden," or "unfeasible" based on a three-level hierarchy of symmetry control: allowed reactions conserve both total and individual orbital symmetries; forbidden ones conserve only the total; and unfeasible ones conserve neither. This classification is rooted in the conservation of angular momentum and selection rules reflecting energetic viability. Grounded in the Born–Oppenheimer approximation (section 2.4.1), the rules assume separate conservation of nuclear, electronic spin, and orbital angular momentum, providing a basis for assessing reaction feasibility through symmetry and energy considerations (SILVER, 1974).

Wigner–Witmer's spin conservation rule dictates that the total spin of the system (section 2.5) must be conserved in reactions occurring on a PES, making spin-forbidden processes, such as those involving a change in spin multiplicity, less probable. It should be noted, however, that while the overall spin of the fragments combined must be conserved, the individual spin states of each fragment may change as long as the total spin remains the same (WIGNER, 1927; WIGNER; WITMER, 1928a; HERZBERG, 2013). Table 4 presents the multiplicities of molecular electronic states for given multiplicities of the separated atoms. The rules presented on Table 4 were fundamental for the construction of the PESs at all stages of this thesis.

Since this work involves the collision of an atom with a diatomic molecule throughout all stages, the following section presents key concepts related to gas-phase chemical reactions, from a microscopic to a macroscopic level. These collisions are essential not only for the construction of PESs, discussed in this section, but also for the calculation of rate constants, which will be addressed in later sections.

Table 4 – Multiplicities of molecular electronic states for given multiplicities of the separated atoms.

Separated Atoms	Molecule
Singlet + singlet	Singlet
Singlet + doublet	Doublet
Singlet + triplet	Triplet
Doublet + doublet	Singlet, triplet
Doublet + triplet	Doublet, quartet
Doublet + quartet	Triplet, quintet
Triplet + triplet	Singlet, triplet, quintet
Triplet + quartet	Doublet, quartet, sextet
Quartet + quartet	Singlet, triplet, quintet, septet

Source: Adapted from Herzberg (2013).
The total spin quantum number is $S = S_1 + S_2, S_1 + S_2 - 1, \ldots, |S_1 - S_2|$, and the multiplicity is $2S + 1$.

Singlet: $S = 0$ $\Rightarrow$ Multiplicity = 1
Doublet: $S = 1/2$ $\Rightarrow$ Multiplicity = 2
Triplet: $S = 1$ $\Rightarrow$ Multiplicity = 3
Quartet: $S = 3/2$ $\Rightarrow$ Multiplicity = 4

2.6.3 Chemical reactions: from the microscopic to the macroscopic level

In chemical reactions, the PES often features minima, representing reactants, intermediates, and products, as well as transition states (TS). Once a TS is located, it must be verified that it connects the appropriate minima, typically by analyzing the vibrational mode associated with the imaginary frequency, which defines the reaction coordinate. At the microscopic level, rate constants depend on the quantum states of the species (electronic, translational, rotational, and vibrational) while the macroscopic rate constant results from a Boltzmann-weighted average over these contributions, making it temperature-dependent. Statistical mechanics provides the essential framework to connect molecular-level dynamics with observable macroscopic behaviour (JENSEN, 2007). The change from a microscopic level to a macroscopic one will be addressed in this section.

Theory plays a key role in both interpreting and predicting chemical reaction dynamics. While collision theory provides a classical framework for estimating reaction rates, emphasizing that sufficient energy and proper molecular orientation are necessary for reactions to occur, reaction dynamics extends this perspective by exploring the microscopic behaviour of atoms and molecules during chemical transformations. This approach offers time-resolved insights into reaction pathways and elementary steps using both classical and quantum methodologies (MCQUARRIE; SIMON, 1997; OLIVEIRA et al., 2016).

A fundamental aspect of understanding these elementary steps involves analysing the PES, which helps identify the most relevant reaction pathways: those with lower energy barriers are more likely to be significant, while high-barrier processes tend to be less favorable (CRAMER, 2004). The dynamical description of gas-phase reactions has led to a standard model of chemical

reactivity, where nuclear motion is treated on a Born–Oppenheimer adiabatic PES (section 2.4.1). Although often well captured by classical mechanics, this model can be extended to include multiple electronic states when necessary (AUERBACH; TULLY; WODTKE, 2021; JENSEN, 2007).

Most experimental and theoretical investigations in chemistry operate at very different scales: while experiments are typically performed on macroscopic samples containing around 10^{23} particles, theoretical calculations usually focus on systems with far fewer species. Bridging this gap requires connecting the behaviour of individual molecules to the collective properties of large systems. These bulk properties are governed by the laws of thermodynamics, with chemical reactions and molecular behaviour commonly described through key thermodynamic quantities such as enthalpy, entropy, and free energy. Within this framework, temperature, for example, reflects the average kinetic energy of the particles ($\langle E_{\text{kin}} \rangle$, equation 2.32) (JENSEN, 2007; CRAMER, 2004):

$$\langle E_{\text{kin}} \rangle = \frac{3}{2} RT. \tag{2.32}$$

At absolute zero, molecules reside in the ground state (with zero-point energy). However, at any other temperature, they are distributed among various quantum energy levels. The relative occupation of a state with energy ε_i is proportional to the Boltzmann factor $e^{-\varepsilon_i / k_B T}$ (where k_B is the Boltzmann constant), but the actual probability is obtained from the normalized Boltzmann distribution. The exponential dependence on energy implies that the probability of finding a molecule in a high-energy state is small, though not zero. However, this lower probability is partially compensated by the fact that there are significantly more available states at higher energies than at lower ones (JENSEN, 2007).

A central concept in statistical mechanics is the partition function. Similar to how the wave function is fundamental in quantum mechanics, enabling the calculation of all observables through appropriate operators, the partition function serves as the foundation for deriving all macroscopic thermodynamic properties. For a single molecule, the canonical partition function, typically denoted by Q, is defined as a sum over all quantum states, weighted by Boltzmann factors (equation 2.33):

$$Q = \sum_{i=\text{states}}^{\infty} e^{-\varepsilon_i / k_B T}. \tag{2.33}$$

The partition function can be viewed as a statistical measure that effectively counts the average number of accessible states, weighted by their Boltzmann factors. It also acts as a normalization constant in the Boltzmann distribution, ensuring that the total probability of all possible energy states sums to one.

When energy levels are very closely spaced, quantum effects can often be neglected, allowing the system to be treated classically. In this classical approximation, the discrete sum

over quantum states is replaced by a continuous integral over the six-dimensional phase space, involving three position coordinates (x, y, z) and three momentum components (p_x, p_y, p_z). The partition function then becomes (equation 2.34):

$$Q = \int e^{-E(r,p)/k_B T} \, d^3r \, d^3p. \tag{2.34}$$

In contrast, in quantum statistical mechanics the partition function can often be simplified by separating contributions from translational, rotational, vibrational, and electronic degrees of freedom.

The partition function enables the calculation of fundamental thermodynamic functions such as the internal energy, U and the Helmholtz free energy, A. Macroscopic observables, such as pressure and the heat capacity at constant volume, C_V, can be determined from derivatives of these thermodynamic functions. From them, additional thermodynamic properties, such as enthalpy H, entropy S, and Gibbs free energy G, can also be obtained (JENSEN, 2007). For instance, the Gibbs free energy of a species can be obtained by (equation 2.35) (JENSEN, 2007):

$$G = H - TS = k_B T V \left(\frac{\partial \ln Q}{\partial V} \right)_T - k_B T \ln Q. \tag{2.35}$$

Considering a reaction, the Gibbs free energy of activation ($\Delta G^{\ddagger}$) is given by (equation 2.36):

$$\Delta G^{\ddagger} = G_{\mathrm{TS}} - G_{\mathrm{reactants}}, \tag{2.36}$$

in which G_{TS} is the Gibbs free energy of the TS and $G_{\mathrm{reactants}}$ is the Gibbs free energy of the reactants. To compute the activation free energy, it is necessary to determine both the enthalpy ($\Delta H^{\ddagger}$) and the entropy ($\Delta S^{\ddagger}$) of activation ($\Delta G^{\ddagger} = \Delta H^{\ddagger} - T\Delta S^{\ddagger}$, for isothermal processes).

To bridge the microscopic and macroscopic levels and to compute partition functions, it is essential to know all possible quantum states of the system. Although the PES is obtained through quantum chemical calculations, it serves as a classical representation of the system. When nuclear motion is treated quantum mechanically, part of the energy is stored in molecular vibrations, even at temperatures near absolute zero, due to the existence of zero-point vibrational energy (ZPE). The harmonic oscillator (HO) model offers a reasonable estimate of the ZPE, as long as vibrational frequencies are accurately computed using reliable electronic structure methods (CRAMER, 2004). However, for high-precision calculations, it is necessary to go beyond the harmonic approximation and include anharmonic effects.

In principle, these vibrational states can be derived by solving the nuclear Schrödinger equation on a well-characterized PES, but such rigorous treatments are typically limited to diatomic or small triatomic systems. For larger, isolated polyatomic molecules, energy levels are more practically estimated using the rigid-rotor harmonic-oscillator (RRHO) approximation,

which assumes separability of electronic, vibrational, and rotational motions. When treating an isolated molecule as an ideal gas, the total partition function can be computed exactly within the RRHO model, where it is expressed as the product of translational, rotational, vibrational, and electronic contributions (equation 2.37) (JENSEN, 2007):

$$Q = q_{\text{trans}} q_{\text{rot}} q_{\text{vib}} q_{\text{elec}}. \tag{2.37}$$

Each contribution can be calculated analytically or numerically for a given temperature, as long as the molecular properties are known. The vibrational term requires the full Hessian (force constant matrix), which is computationally the most demanding part (JENSEN, 2007). In gas-phase reactions, chemical reactivity depends not only on the total energy of the reactants but also on how this energy is distributed among their rotational, vibrational, and electronic states. A full understanding of reaction dynamics requires accounting for all energy storage and transfer pathways during reactive encounters (MCQUARRIE, 1976).

A great motivation for developing a microscopic understanding of chemical dynamics is to predict reaction rates, a task for which Transition State Theory (TST) has been particularly effective (AUERBACH; TULLY; WODTKE, 2021). When combined with accurate PESs and classical, quantum, or semiclassical dynamics, this approach enables the investigation of reaction mechanisms even under extreme conditions such as those in the ISM. To this end, complex reactions are broken down into elementary steps, each with its own rate law and molecularity. To further connect molecular energetics with observable reaction rates, the next section introduces TST as a statistical framework for calculating rate constants and exploring the energetics of chemical transformations.

2.6.4 Transition state theory (TST)

Transition State Theory (TST) is a statistical mechanical framework used to describe chemical reaction rates. It begins by introducing a reaction coordinate, s, which extends from negative values (representing reactants) to positive values (representing products). TST assumes that the reactants are in local thermal equilibrium and that internal vibrational energy redistributes much faster than the timescale of bond breaking or formation. In this model, motion along the reaction coordinate is treated classically, whereas motions perpendicular to it incorporate quantum effects, such as vibrational and rotational quantization. As a result, the reaction rate depends only on the total internal energy, with the population of quantum states following a Boltzmann distribution, proportional to $e^{-\Delta E/kT}$ (JENSEN, 2007).

The transition state (TS) is defined as the configuration corresponding to a fixed value of s, effectively representing a system with one fewer degree of freedom than the reactants (TRUHLAR; GARRETT, 1984). It is treated as a quasi-equilibrium ensemble of quantized states located near the top of the energy barrier, thermally populated and in equilibrium with the reactants. In the

original approach of the TST method, the TS is usually associated with a first-order saddle point on the PES, featuring a maximum along the reaction coordinate and minima in all orthogonal directions, and is characterized by a single imaginary vibrational frequency that defines the direction of the reaction (JENSEN, 2007; LEVINE, 2000; CRAMER, 2004).

This theory was first developed by Eyring, Evans, and Polanyi in the 1930s (EYRING, 1935b; EVANS; POLANYI, 1938). In their original formulation, Eyring proposed the existence of a distinct configuration, the activated complex (AC), which, once formed, would proceed to products with near certainty. In the context of this section, the AC and the TS will be treated as synonymous. In a profound conceptual advance, Eyring assumed that this AC remains in thermal equilibrium with the reactants (AUERBACH; TULLY; WODTKE, 2021; EYRING, 1938). The accuracy of Eyring's formulation for this theory (EYRING, 1935a) depends on reliable evaluation of molecular partition functions, particularly in well-defined gas-phase systems (EYRING, 1935a; OLIVEIRA et al., 2016).

The reaction coordinate, often expressed in mass-weighted terms, represents the sequence of atomic rearrangements (e.g., bond length and angle changes) that lead to product formation. The energy difference between the reactants and the TS defines the activation energy (AE), which controls the reaction rate (JENSEN, 2007). When the geometry and energy of the TS are accurately determined, TST allows reliable estimation of rate constants based on thermodynamic and kinetic parameters (CRAMER, 2004; BAO; TRUHLAR, 2017), as it will be clarified next. Figure 5 illustrates a schematic energy profile for a generic reaction, highlighting key features relevant to kinetic analysis.

Figure 5 – Potential energy profile for a generic reaction.

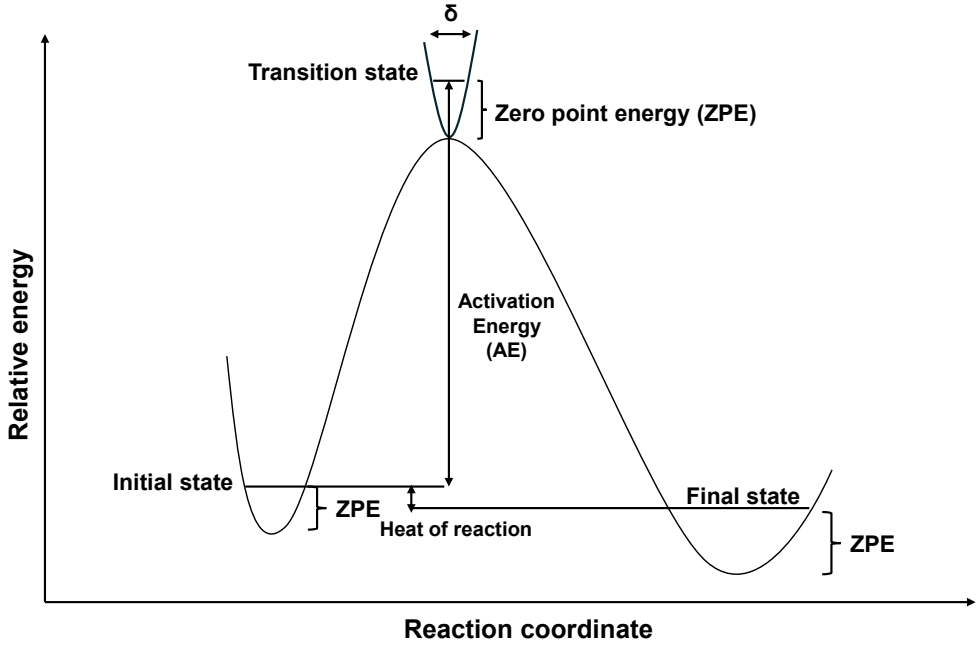

Source: Adapted from Eyring (1935a) and McQuarrie and Simon (1997).

To arrive in the final form of Eyring's equation, let's begin by considering a general bimolecular reaction of the form A + B → P (MCQUARRIE; SIMON, 1997). For this process, the rate law is given by:

$$\frac{dP}{dt} = k(T)[\mathrm{A}][\mathrm{B}]. \tag{2.38}$$

The AC theory assumes that the reactants and the TS are in equilibrium, allowing the reaction to be represented as a two-step mechanism:

$$\mathrm{A} + \mathrm{B} \rightleftharpoons \mathrm{AB}^{\ddagger} \rightarrow \mathrm{P}, \tag{2.39}$$

where $\mathrm{AB}^{\ddagger}$ is the TS. The equilibrium-constant expression between the reactants and the TS is:

$$K^{\ddagger} = \frac{[\mathrm{AB}^{\ddagger}]}{[\mathrm{A}]/[\mathrm{B}]} = \frac{[\mathrm{AB}^{\ddagger}]}{[\mathrm{A}][\mathrm{B}]}. \tag{2.40}$$

$K^{\ddagger}$ can be written in terms of partition functions (section 2.6.3):

$$K^{\ddagger} = \frac{(q^{\ddagger}/V)}{(q_{\mathrm{A}}/V)(q_{\mathrm{B}}/V)}, \tag{2.41}$$

where V is the volume of the system and q_{A}, q_{B}, and $q^{\ddagger}$ are the partition functions of A, B, and $\mathrm{AB}^{\ddagger}$, respectively.

The TS is considered to be stable within a narrow region of width δ centered at the top of the potential energy barrier (Figure 5). According to the two-step mechanism described in Equation 2.39, the reaction rate is given by the product of the concentration of the TS, $[\mathrm{AB}^{\ddagger}]$, and ν, the frequency with which these complexes proceed over the barrier. Therefore:

$$\frac{dP}{dt} = \nu[\mathrm{AB}^{\ddagger}]. \tag{2.42}$$

Considering equations 2.38 and 2.42 as equivalents expressions for the rate constant, solving equation 2.40 for $[\mathrm{AB}^{\ddagger}]$, substituting the resulting expression into equation 2.42 and finally equating the result to equation 2.38 yields:

$$\frac{dP}{dt} = k(T)[\mathrm{A}][\mathrm{B}] = \nu[\mathrm{AB}^{\ddagger}] = \nu[\mathrm{A}][\mathrm{B}]K^{\ddagger}, \tag{2.43}$$

or,

$$k(T) = \nu K^{\ddagger}. \tag{2.44}$$

In deriving Equation 2.42, it is assumed that the motion of the reacting system over the top of the potential energy barrier can be treated as a one-dimensional translational motion. The corresponding translational partition function, q_{trans}, for this one-dimensional case is given by:

$$q_{\text{trans}} = \frac{(2\pi m^{\ddagger} k_B T)^{1/2}}{h}\,\delta, \tag{2.45}$$

where $m^{\ddagger}$ is the mass of the TS, and δ represents the effective width of the region over which the complex is considered to be in quasi-equilibrium at the barrier top. The full partition function of the activated complex can be expressed as:

$$q^{\ddagger} = q_{\text{trans}}\, q^{\ddagger}_{\text{int}}, \tag{2.46}$$

where $q^{\ddagger}_{\text{int}}$ is the internal partition function, accounting for vibrational, rotational, and electronic contributions of the TS. Equation 2.41 can now be written as:

$$K^{\ddagger} = \frac{(2\pi m^{\ddagger} k_B T)^{1/2}}{h}\,\delta \frac{q^{\ddagger}_{\text{int}}/V}{(q_{\text{A}}/V)(q_{\text{B}}/V)}. \tag{2.47}$$

Substituting equation 2.47 into equation 2.44 leads to the following expression for the reaction rate constant:

$$k(T) = \nu \frac{(2\pi m^{\ddagger} k_B T)^{1/2}}{h}\,\delta \frac{(q^{\ddagger}_{\text{int}}/V)}{(q_{\text{A}}/V)(q_{\text{B}}/V)}. \tag{2.48}$$

In this latter equation, the values of ν and δ are not precisely defined and are challenging to determine independently. However, their product can be interpreted as the average velocity with which the TS crosses the barrier, denoted $\langle u_{\text{ac}} \rangle$, where $\langle u_{\text{ac}} \rangle = \nu\delta$. Since the TS is assumed to be in equilibrium with the reactants, the one-dimensional Maxwell–Boltzmann distribution can be applied to estimate $\langle u_{\text{ac}} \rangle$. After this is performed, the TST expression for the rate constant is achieved (MCQUARRIE; SIMON, 1997):

$$k(T) = \frac{k_B T}{h} \frac{(q^{\ddagger}_{\text{int}}/V)}{(q_{\text{A}}/V)(q_{\text{B}}/V)} = \frac{k_B T}{h} K^{\ddagger}. \tag{2.49}$$

We now consider the fundamental thermodynamic expressions: $\Delta G^{\ddagger} = \Delta H^{\ddagger} - T\Delta S^{\ddagger}$ and $\Delta G^{\ddagger} = -RT \ln K^{\ddagger}$, where $\Delta G^{\ddagger}$ is the Gibbs free energy of activation. Solving the latter equation for $K^{\ddagger}$ and substituting the result into Equation 2.49, the rate constant can be expressed as (MCQUARRIE; SIMON, 1997):

$$k(T) = \frac{k_B T}{h} e^{-\Delta^{\ddagger} G/RT}. \tag{2.50}$$

And, since $\Delta G^{\ddagger} = \Delta H^{\ddagger} - T\Delta S^{\ddagger}$, as:

$$k(T) = \kappa \frac{k_B T}{h} e^{\frac{\Delta S^{\ddagger}}{R}} e^{-\frac{\Delta H^{\ddagger}}{RT}}. \tag{2.51}$$

or, more compactly:

$$k(T) = \kappa \frac{k_B T}{h} \exp\left(\frac{\Delta S^{\ddagger}}{R} - \frac{\Delta H^{\ddagger}}{RT}\right), \tag{2.52}$$

which is the final form of Eyring's Equation for Transition State Theory. This formulation highlights the connection between kinetics and thermodynamics, in which the AE incorporates both enthalpic and entropic contributions. Besides that, in quantum chemical calculations $\Delta G^{\ddagger}$ can be derived from the difference in electronic energies corrected by ZPEs and thermal contributions (partition functions, section 2.6.3). This approach is fundamental for the calculations performed in this thesis using the approach of the master equation for multiple-well chemical reactions (GEORGIEVSKII et al., 2013).

The transmission coefficient κ is included in Equations 2.51 and 2.52, following Eyring's original formulation (EYRING, 1935a). It represents the fraction of activated complexes that effectively cross the transition state to yield products. For many simple reactions, κ is approximately equal to one. However, it cannot be derived from equilibrium statistical mechanics and instead requires a dynamical treatment (EYRING, 1935a). As a result, the rate constant calculated from the canonical TST expression typically represents an upper bound to the true rate constant (JENSEN, 2007; AUERBACH; TULLY; WODTKE, 2021; OLIVEIRA et al., 2016).

Including the κ factor refines the model, but the tunneling effects considered in canonical TST are sometimes insufficient for accurately describing the reaction dynamics. Consequently, despite its utility and broad applicability, TST has known limitations, particularly in accounting for barrier recrossings and quantum tunneling. These shortcomings have led to the development of more advanced approaches, such as Variational Transition State Theory (VTST), which will be briefly discussed in the next subsection.

2.6.4.1 Variational Transition State Theory

Variational Transition State Theory (VTST) refers to a class of theories that determine the optimal TS by applying either the minimum flux criterion or the condition of maximum free energy of activation. While VTST improves the location of the TS, it still relies on the local equilibrium assumption and requires additional approximations to translate the flux-through-a-hypersurface concept into a quantum mechanical context, preventing exact rate predictions. Additionally, the variational optimization is typically performed under practical constraints, such as restricting the search to a one-dimensional path in coordinate space (TRUHLAR; GARRETT, 1984).

Although TST assumes that each trajectory crosses a dividing surface only once, in reality, recrossing can occur, especially in complex systems, leading to an overestimation of reaction rates. To reduce this error, the dividing surface should ideally be placed at the dynamical bottleneck,

where recrossing is minimized (BAO; TRUHLAR, 2017). In canonical TST, the free energy of the system is computed at the TS geometry (corresponding to the activated complex), a stationary point where partition functions are evaluated using the RRHO approximation. However, this point corresponds only to the maximum potential energy along the MEP, not necessarily the maximum in free energy. In some cases, vibrational mode tightening beyond the TS can increase the ZPE, resulting in a higher free energy than at the TS. VTST addresses these issues by allowing the dividing surface to move along the MEP to locate the position that minimizes the rate constant, providing a more accurate and flexible framework for describing reaction dynamics (CRAMER, 2004; TRUHLAR; GORDON, 1990; TRUHLAR; GARRETT, 1980; TRUHLAR; GARRETT, 1984). The VTST rate can be expressed by:

$$k^{\mathrm{VTST}}(T,s) = \min_{s} \frac{k_B T}{h} \frac{Q^{\ddagger}(T,s)}{Q_R} \frac{Q_R^0}{Q_{\ddagger,0}} \exp\left(-\frac{\Delta V^{\ddagger}(s)}{k_B T}\right), \tag{2.53}$$

where s denotes a position along the MEP at which the VTST rate constant, k^{VTST}, is computed. By definition, $s = 0$ corresponds to the saddle point, while negative and positive values of s indicate displacements toward the reactant and product sides of the saddle point, respectively (CRAMER, 2004).

By optimizing the position of the dividing surface, VTST generally yields rate constants lower than those predicted by canonical TST (CRAMER, 2004). Studies by Allison and Truhlar (ALLISON; TRUHLAR, 1998), based on advanced quantum dynamics calculations for small molecular systems, have demonstrated that VTST reproduces rate constants much closer to exact results, particularly at high temperatures (CRAMER, 2004).

As temperature approaches zero, the rate constant for an exergonic reaction does not vanish but instead levels off to a small, non-zero value due to quantum tunneling from the lowest energy state of the reactants. Neglecting tunneling can lead to misinterpretation of this behaviour as zero activation enthalpy (CRAMER, 2004). To improve the treatment of tunneling, the Eckart potential (ECKART, 1930) provides an exact analytical solution for tunneling probabilities by solving the time-independent Schrödinger equation at fixed energy. Integrating these probabilities over all energies, weighted by their thermal distribution, leads to a reliable estimate of the tunneling correction factor, assuming primarily one-dimensional tunneling (CRAMER, 2004; GARRETT; TRUHLAR, 2005).

Refined approaches, such as Canonical VTST (CVT) and Variable Reaction Coordinate TST (VRC-TST), further enhance accuracy in systems with shallow or barrierless PESs. These methods account for non-classical effects in vibrational modes orthogonal to the reaction coordinate by calculating quantized vibrational frequencies and ZPEs. Additionally, multidimensional tunneling corrections become essential for high-accuracy kinetic modeling, particularly in areas like astrochemistry and excited-state reactivity, ensuring consistency with experimental data in non-classical regimes. One notable refinement is the Small Curvature Tunneling (SCT)

method (LIU et al., 1993), which incorporates multidimensional tunneling effects and improves predictions for hydrogen transfer and low-temperature reactions. The VRC-TST approach, in turn, performs variational optimization over a set of flexible dividing surfaces, making it especially effective for barrierless processes and capable of predicting capture rate constants to within 25% (KLIPPENSTEIN, 2017).

Despite its limitations, TST remains a cornerstone of chemical kinetics, offering a conceptual and computational connection between molecular-level information and macroscopic observables. When supported by high-quality *ab initio* PESs and integrated with statistical mechanics, it enables the prediction of rate constants based on electronic structure, geometry, and thermodynamic parameters, forming a robust foundation for reaction modelling across a wide range of chemical environments. In the following and final section of the theoretical framework, the Multiple-Well Master Equation theory will be introduced qualitatively. This theory served as the foundation for the calculation of rate constants using TST throughout all stages of the project developed in this thesis.

2.6.5 The Multiple-Well Master Equation

In many systems, such as the ones that involve combustion and atmospheric processes, the reactions proceed through complex mechanisms involving multiple, interconnected potential wells (KLIPPENSTEIN; MILLER, 2002). Reactions that occur in the ISM can also be included in these sort of reactions. These processes may follow chemically activated pathways or proceed via thermal dissociation and isomerization. In some cases, the intermediate complexes are extremely short-lived, resulting in effectively collisionless conditions. These reactions typically involve few atoms and shallow potential wells, which correspond to low densities of states (KLIPPENSTEIN; MILLER, 2002).

In chemical kinetics, the master equation (ME) governs the time evolution of the population or probability of finding a system in a particular energy or quantum state. Its simplest form is the time-continuous, discrete-state equation (MILLER; KLIPPENSTEIN, 2006):

$$\frac{dn_i(t)}{dt} = \sum_j \left(p_{ij} n_j(t) - p_{ji} n_i(t) \right), \tag{2.54}$$

in which $n_i(t)$ is the population of state i at time t, and p_{ij} is the transition probability per unit time from state j to state i. This formulation assumes a process where the transition rates are time-independent. Originally derived in quantum mechanics by Wolfgang Pauli (PAULI, 1928), this version of the ME is well suited for describing unimolecular reactions and energy redistribution in the low-pressure regime (MILLER; KLIPPENSTEIN, 2006).

For large polyatomic systems, the number of accessible quantum states is too great for state-resolved treatments. Therefore, a simplified approach is adopted, grouping populations by energy intervals (E to $E + dE$), or by energy and total angular momentum J (MILLER;

KLIPPENSTEIN, 2006). In this context, the ME is applied not to individual quantum states, but to energy ranges, allowing the treatment of complex intramolecular and unimolecular processes.

To construct the ME model, energy-resolved rate coefficients $k(E)$ are needed for isomerization and dissociation/recombination steps. These are calculated from the PES, often using conventional TST for isomerizations and variational TST for dissociation pathways (MILLER; KLIPPENSTEIN, 2006). Importantly, the transition probabilities and rate coefficients that appear in the ME are actually microscopic flux coefficients, representing transitions between states or energy segments (MILLER; KLIPPENSTEIN, 2006).

This equivalence holds particularly well in the collisionless limit, where reactive intermediates decay before undergoing additional collisions. In this situation, or when full thermal equilibrium exists among all species and energy levels, rate coefficients correspond directly to fluxes (MILLER; KLIPPENSTEIN, 2006). However, when multiple pathways compete, solving the full time-dependent ME becomes necessary. In such cases, rate coefficients can be extracted by integrating the ME over time (MILLER; KLIPPENSTEIN, 2006).

The ME formalism is especially valuable in systems involving multiple coupled wells and product channels. Under some assumptions, such as thermal equilibrium of bath gas, low concentrations of reactive fragments, and excess of one fragment over the other, the ME becomes linear. This simplification preserves the ability to derive accurate thermal rate coefficients while making the system tractable (MILLER et al., 2009).

In this formulation, the ME depends on internal energy E and time t, while the dependent variables are the population densities within the wells (functions of E and t) and the time-dependent populations of the deficient fragments (MILLER; KLIPPENSTEIN, 2013). The separation of timescales between fast internal energy redistribution and slower chemically significant modes is a crucial condition for phenomenological kinetics to be valid (MILLER; KLIPPENSTEIN, 2013).

In their work, Georgievskii et al. (2013) presented a reformulation and solution of the ME for Multiple-well chemical reactions and bimolecular products. Their approach was the basis for calculating the rate constants thorough this thesis. In this framework, the dynamical space is limited to the microscopic populations of the isomeric forms within the reactive complex, while the bimolecular species (reactants and products) are incorporated as boundary conditions, acting as external sources and sinks. This approach can lead to phenomenological rate coefficients governing various types of chemical transformations, including internal isomerizations, bimolecular exchanges, and conversions between isomers and bimolecular species.

In this alternative formulation, the ME is expressed in terms of energy-dependent populations of each isomer within the reactive complex, while bimolecular reactants are treated as independent external sources. Their concentrations are not explicitly expressed, but this does not prevent the derivation of complete phenomenological rate coefficients. This fact is achieved

by linking the relaxation of chemically significant eigenmodes to the observed kinetics. This methodology remains valid as long as bimolecular concentrations change more slowly than the collisional energy relaxation (GEORGIEVSKII et al., 2013).

Ultimately, the ME provides a rigorous connection between microscopic population dynamics and macroscopic rate expressions. Its ability to incorporate detailed PESs, energy transfer models, and multichannel reaction pathways makes it a fundamental tool in theoretical chemical kinetics (MILLER; KLIPPENSTEIN, 2006; KLIPPENSTEIN; MILLER, 2002; GEORGIEVSKII et al., 2013).

3 Methodology

All electronic structure calculations reported here, unless stated otherwise, were performed using the GAMESS-US (SCHMIDT et al., 1993) and MOLPRO (WERNER et al., 2012; WERNER et al., 2015) packages, being the Wxmacmolplt and Avogadro softwares used for graphic visualization and representation of the molecular geometries (BODE; GORDON, 1998; HANWELL et al., 2012).

Each system studied in this work employed its own calculation methodology, particularly for the kinetic studies. These differences arose in response to specific problems or issues encountered. Furthermore, different collaborators actively participated in each reaction studied, contributing suggestions and their calculation expertise. A general summary applicable to all reactions will be presented next, followed by the specific details used for each individual study.

1. In a first step, considered of exploratory nature, the study of the reaction mechanisms and the calculation of their respective PESs were carried out with the aim of optimizing the geometries and obtaining the respective vibration frequencies for all stationary points found. It is important to emphasize at this point, that, in all cases studied here, a mapping of the PESs was carried out rather than an analytical modeling of the multidimensional surface. Based on this mapping, stationary points were located and characterized.

2. The geometries used for mapping the PESs were obtained through systematic scans along different reaction-relevant coordinates, while keeping the remaining coordinates fixed at specific values. For each coordinate analyzed, different numbers of points and step sizes (in Ångströms or degrees, as appropriate) were employed. The choice of the number of points and their respective increments was adjusted on a case-by-case basis to best suit the characteristics of each scan. These adjustments were made iteratively as the analysis progressed and as specific issues, such as convergence difficulties, arose. These scans were performed using the MOLPRO (WERNER et al., 2012; WERNER et al., 2015) package.

3. In this exploratory part, the DFT (KOHN; SHAM, 1965),with the exchange and correlation functional M06-2X (ZHAO; TRUHLAR, 2008a; ZHAO; TRUHLAR, 2008c) and the CASSCF methods were employed. The aug-cc-pVTZ basis set of Dunning and co-workers (DUNNING, 1989; KENDALL; DUNNING; HARRISON, 1992) including additional tight-d functions (+d) for the P atom was employed. For DFT calculations, the M06-2X functional was chosen due to its known accuracy for predicting energy barrier heights (ZHAO; TRUHLAR, 2008b; MARDIROSSIAN; HEAD-GORDON, 2016; PEVERATI; TRUHLAR, 2012).

4. After this exploratory step the intention was to carry out calculations to refine the energies obtained using more sophisticated approaches such as performing single-point calculations with the internally contracted multireference configuration interaction (MRCI) method (SZALAY et al., 2012; SHIOZAKI; KNIZIA; WERNER, 2011), including the Davidson correction [MRCI(Q)] or performing single-point energy coupled cluster singles and doubles and perturbative triples (CCSD(T)) (BARTLETT, 1989; BARTLETT et al., 1990; RAGHAVACHARI et al., 1989), including explicit correlation (CCSD(T)-F12) (ADLER; KNIZIA; WERNER, 2007; KNIZIA; ADLER; WERNER, 2009), also using the basis set of Dunning and co-workers (DUNNING, 1989; KENDALL; DUNNING; HARRISON, 1992) including additional tight-d functions (+d) for the P atom.

5. Regarding the CASSCF and MRCI calculations, a complete active space was carefully selected for all systems in order to properly account for their multireference character and to ensure a comprehensive description of all relevant electronic configurations, including those of the reactants, products, and key intermediates or transition states along the reaction coordinate.

6. In order to analyse the multireference character (MR) of the systems, the T_1 diagnostic and the magnitude of the dominant configuration in the CI wave functions (C_0^2) were collected. It is known that a T_1 diagnostic higher than 0.02 (LEE; TAYLOR, 1989; LEININGER et al., 2000; LEE, 2003) and a C_0^2 smaller than 0.90 are indicatives of a significant MR character.

3.1 $P(^4S) + O_2(^3\Sigma_g^-) \rightarrow O(^3P) + PO(^2\Pi)$

The $P(^4S) + O_2(^3\Sigma^-)$ collision can proceed on doublet, quartet, or sextet potential energy surfaces. However, in the astrochemical context, particularly in the low-temperature, low-density environments of the ISM, the influence of spin-orbit coupling and intersystem crossing is expected to be minor. These conditions suppress the efficiency of nonadiabatic transitions. Therefore, based on the spin conservation rules of Wigner and Witmer (WIGNER, 1927), discussed in section 2.6.2.1, the high-spin sextet pathway was excluded from consideration, as it cannot directly yield ground-state O+PO products.

Vibrational analysis was carried out to confirm the minima and transition states (TSs) found, and to obtain the zero-point energies (ZPE) of each structure. Intrinsic reaction coordinate (IRC) calculations were performed using the Gonzales-Schlegel second-order algorithm (GONZALEZ; SCHLEGEL, 1990) for all TSs found in order to confirm the proposed mechanisms, at the DFT level. The initial objective was to later improve the DFT energies by performing single-point CCSD(T) energy calculations, including explicit correlation (CCSD(T)-F12).

However, the first explorations indicated that the DFT approach would not be suitable due to the presence of low-lying electronic states and unusually high multireference character. Due

to this result, geometry optimizations and frequencies calculations at the full valence complete active space self-consistent field (SZALAY et al., 2012; SHIOZAKI; KNIZIA; WERNER, 2011) level for all stationary points were performed, also using the aug-cc-pVTZ basis. The complete active space selected for CASSCF calulations involves a total of 17 correlated electrons in 12 active orbitals. The CAS(17,12) energies were further improved by performing single-point energies calculations with the MRCI method, including the Davidson correction [MRCI(Q)].

All the final energies reported in the *Results and discussion* chapter are ZPE corrected. The final methodology can be termed MRCI(Q)/aug-cc-pV(T+d)Z//CASSCF/aug-cc-pV(T+d)Z +ZPE(CASSCF/aug-cc-pV(T+d)Z). However, for simplicity of notation, it is reported in this work as MRCI(Q)/AVXZ+d//CAS/AVXZ+d. Within this methodology notation one / separates the calculation method and the basis that were employed, whereas two / separates the single point energy refinement and the respective optimization method.

Since, as it will be later noticed, the P+O_2 barrier is the most important quantity controlling overall reactivity, and aiming to evaluate the effect of increasing the basis sets, single-state MRCI(Q) calculations at CAS/AVXZ+d optimized cuts along the POO→P+O_2 dissociation on the ground $^2A'$ state using the basis AVXZ+d ($X = T, Q, 5$) were performed.

In order to better elucidate, the connections between the predicted transition states and associated minima, CAS/AVTZ+d PES cuts along the reactions coordinates were made. This aimed the selection of a single reaction coordinate, *i.e.*, the one which determines fully the bond-breaking/bond-forming process, while subjecting all other degrees of freedom to a constrained optimization at each point of a predefined active coordinate grid. After this procedure, IRC calculations were considered unnecessary at this level of theory.

Rate coefficients were calculated using the MRCI(Q) energies and CAS/AVTZ+d geometries and frequencies. The MESS software package (GEORGIEVSKII et al., 2013) (section 2.6.5) was used to compute nonvariational rigid rotor/ harmonic oscillator rate coefficients using standard transition state theory (TST), including a one-dimensional Eckart tunneling correction (ECKART, 1930). The final reported rate coefficients are independent of pressure at the very low pressures of the environments considered in this thesis.

3.2 $N(^4S) + PN(^1\Sigma^+) \rightarrow N_2(^1\Sigma_g^+) + P(^4S)$

The collision of ground state nitrogen ($N(^4S)$) atoms and singlet PN ($^1\Sigma^+$) molecules produces a quartet state PES. Therefore, once again taking into consideration the rules of Wigner and Witmer, other spin multiplicities were not taken into account. For this particular system, apart from the GAMESS-US (SCHMIDT et al., 1993) and MOLPRO (WERNER et al., 2015) packages, the ORCA (NEESE et al., 2020) package was also employed.

Similarly with the previous system, the first objective was to study the mechanism of the

$N(^4S)$ + $PN(^1\Sigma^+)$ collision and calculate the rate coefficient using geometry optimizations and frequencies calculations at the CASSCF level for all stationary points (15 correlated electrons in 12 active orbitals, *i.e.*, a complete active space). This was followed by single-point MRCI+Q energy calculations, also using the aug-cc-pVTZ basis set and also including additional tight-*d* functions (+*d*) for the P atom (AV*T*Z+d). For a smoother representation of the PES, two electronic states were calculated at the CASSCF level, with the state-averaged approach.

The nonvariational rigid rotor/ harmonic oscillator rate constant was calculated using standard transition state theory (TST), using the MESS software package, including a one-dimensional Eckart tunneling correction. Vibrational analysis was carried out at the CASSCF level to confirm each structure found on the PES, being the methodology briefily denoted as MRCI+Q/AVTZ+d//CASSCF/AVTZ+d. In order to increase the accuracy in the final reported rate coefficients, MRCI+Q/AVTZ+d geometry optimization and frequencies calculations for the preferred mechanism were performed. This preferred mechanism will become clearer in the *Results and discussion* chapter.

For this particular system, canonical variational transition state theory (CVT) with DFT theory and the M06-2X functional was used for comparison, with refined single point calculations using CCSD(T) theory at the complete basis set (CBS) limit. This procedure aimed to maximize the free energy with respect to the reaction coordinate and thus minimizing the rate constant. This approach considers this variational transition state optimizing the dividing surface between reactants and products improving the treatment of the no-recrossing assumption inherent to standard TST theory (section 2.6.4.1). For CVT calculations, the PILGRIM package (FERRO-COSTAS; TRUHLAR; FERNÁNDEZ-RAMOS, 2019; FERRO-COSTAS; TRUHLAR; FERNANDEZ-RAMOS, 2020) was used, being the required electronic structure calculations performed in parallel using the ORCA sofware (NEESE et al., 2020). In order to include quantum effects on the reaction motion, the small curvature tunneling method (SCT) (LIU et al., 1993) was employed.

Within the M06-2X approach, IRC calculations were performed, using the Gonzales-Schlegel second-order algorithm (GONZALEZ; SCHLEGEL, 1990), as implemented in GAMESS, and the Page e Jr (1988) method, as implemented in PILGRIM, in order to confirm the proposed mechanism, and compare with MRCI+Q/AVTZ+d//CAS/AVTZ+d results.

For benchmark purpose, single-point CCSD(T) energy calculations, including explicit correlation (CCSD(T)-F12) at the M06-2X/AVTZ+d geometries, using the VTZ-F12 basis set were performed, in order to assess the importance of using unrestricted coupled cluster wave functions (UCCSD(T)). For this particular system, apart from the T_1 diagnostic and the magnitude of the dominant configuration in the CI wave functions (C_0^2), the Multireference Diagnostic (M) (TISHCHENKO; ZHENG; TRUHLAR, 2008) of all stationary points were obtained. The M Diagnostic is given by:

$$M = \frac{1}{2}[2 - n(MCDONO) + \sum_{j=1}^{n_{SOMO}} |n(j) - 1| + n(MCUNO)], \tag{3.1}$$

where n_{SOMO} is the number of singly occupied molecular orbitals in the dominant electronic configuration of the ground state.

Following the formulation proposed by the authors in Tishchenko, Zheng e Truhlar (2008), the occupation numbers appearing in Equation 3.1 correspond to three key natural orbitals: the most correlated doubly occupied natural orbital (MCDONO), a singly occupied molecular orbital (SOMO), and the most correlating unoccupied natural orbital (MCUNO), denoted respectively as n(MCDONO), n(SOMO), and n(MCUNO). The MCDONO is defined as the doubly occupied orbital in the dominant configuration with the lowest occupation number, while the MCUNO is the virtual orbital (i.e., unoccupied in the dominant configuration) with the highest occupation number. The SOMOs are indexed by $j = 1, \ldots, n_{\mathrm{SOMO}}$.

3.3 $P(^4S)+NH(^3\Sigma^-) \rightarrow H(^2S)+PN(^1\Sigma^+)$ and $N(^4S)+PH(^3\Sigma^-) \rightarrow H(^2S) + PN(^1\Sigma^+)$

When it comes to the $P(^4S)$ + $NH(^3\Sigma^-)$ and $N(^4S)$ + $PH(^3\Sigma^-)$ reactions, DFT theory was also used for a preliminary exploratory work, also with the aug-cc-pV(T+d)Z basis set (AVXZ+d) and the exchange and correlation functional M06-2X. Vibrational analysis was also carried out within the DFT approach in order to confirm the minima and TSs found.

After this exploratory part, differently from the other two systems, all of the DFT stationary structures were fully reoptimized and refined using CASSCF and CCSD(T) methods. Vibrational analysis was also carried out within both approaches. Once again, for the CASSCF calculations a complete active space of 11 correlated electrons in 9 active orbitals was selected. After this reoptimization, the energies were further refined through the perfomance of single-point energy calculations at the MRCI-F12 method, including the Davidson correction and also using the AVTZ+d basis set. The CCSD(T) calculations were used to benchmark the computed energies, and the structures were reoptimized and using the AVTZ+d basis set. This was followed by a single point energy refinement using the CCSD(T)-F12 (ADLER; KNIZIA; WERNER, 2007; KNIZIA; ADLER; WERNER, 2009) with the cc-pVQZ-F12 basis set (hereafter, denoted as VQZ-F12).

Unlike the previous reactions, the ones explored here do not present an energy barrier, and thus require a different TST treatment. Therefore, for these collisions, the capture rate coefficients were calculated using direct variable reaction coordinate transition state theory (VRC-TST) (KLIPPENSTEIN, 1991; KLIPPENSTEIN, 1992), as implemented in the distributed computer code VaReCoF (HARDING; GEORGIEVSKII; KLIPPENSTEIN, 2005). Fragment

interaction energies were calculated using CAS(5e,5o)PT2/CBS with the CBS limit estimated using a two-point formula (MARTIN; UZAN, 1998) and AV*T*Z and AV*Q*Z basis sets.

The MESS software was employed to calculate the overall reaction rate coefficients, which were proven to be equivalent to the rate of the first step (capture). This software was also used to calculate the backward reaction rates up to 4889 K, in order to analyse the possibility that the H+PN collision could lead to PN destruction in environments of high temperatures of the ISM, such as shock and star forming regions. Another possible barrierless channel on the N+PH collisions (N+PH $\rightarrow$ P+NH) was also evaluated within this approach to check its influence in the branching ratio of the overall N+PH reactivity.

3.4 CPN system

For the CPN system, the DFT energy values, were improved with single-point energy calculations at the CCSD(T)-F12/cc-pVTZ-F12 level. Being this procedure hereafter namely as CCSD(T)-F12/VTZ-F12//M06-2X/AV*T*Z+d + ZPE(M06-2X/AV*T*Z+d).

Once again, in order to account for a possible multiconfigurational character of the system, all the previously obtained results were fully re-optimised within the CASSCF approach, also with the AV*T*Z+d basis set. The complete active space was set as 12 orbitals with 14 electrons. Vibrational analysis was also carried out and ZPEs were obtained for all stationary points on the CASSCF PES. The accuracy of the energy values was further enhanced by performing single-point energy calculations over all structures with the MRCI-F12 method, including the relaxed-reference Davidson correction to approximate quadruple excitations and also using the AV(T+d)Z basis set. Being this methodology reported as MRCI-F12/AV*T*Z+d//CAS/AV*T*Z+d + ZPE(CAS/AV*T*Z+d). The C_0^2 and the T_1 diagnostic values of all stationary points, were also collected.

The rigid rotor/harmonic oscillator rate coefficients using standard TST and including the Eckart tunnelling correction (ECKART, 1930) employing the MESS software package (GEORGIEVSKII et al., 2013) were computed for all possible situations. Within a barrierless reaction path approach, phase space theory (PST) (PECHUKAS; LIGHT, 1965; CHESNAVICH, 1986), as implemented in MESS, was used for the capture steps. In these cases, the MRCI-F12/AV*T*Z+d energies were fitted as a function of the internuclear separation "r" to the $-C_6/r^6$ (section 2.6.2) function to obtain " C_6", which was then used in the PST calculation.

4 Results and discussion

All results that are going to be presented and discussed in this chapter have been published elsewhere. The papers are entitled: "*Formation of phosphorus monoxide through the* $P(^4S) + O_2(^3\Sigma^-) \rightarrow O(^3P) + PO(^2\Pi)$ *reaction*" (GOMES et al., 2022), "*Destruction of phosphorus nitride through the* $N(^4S) + PN(^1\Sigma^+) \rightarrow N_2(^1\Sigma^+) + P(^4S)$ *reaction*" (GOMES et al., 2023b), "*The* $P(^4S) + NH(^3\Sigma^-)$ *and* $N(^4S) + PH(^3\Sigma^-)$ *reactions as sources of interstellar phosphorus nitride*" (GOMES et al., 2023a), and "*New routes for PN destruction and formation in the ISM via neutral-neutral gas-phase reactions and an extended database for reactions involving phosphorus*" (SILVA et al., 2025). See Appendix A for detailed references.

4.1 $P(^4S) + O_2(^3\Sigma_g^-) \rightarrow O(^3P) + PO(^2\Pi)$

4.1.1 Potential energy surface and reaction mechanism

In collisions between $P(^4S) + O_2(^3\Sigma^-)$, the reactants can approach each other in one doublet, one quartet, and one sextet electronic states. However, as already mentioned, the sextet electronic state cannot lead to the products in their ground state. Instead, the ground state products $O(^3P) + PO(^2\Pi)$ correlate with six doublet ($3^2A' + 3^2A''$) and six quartet ($3^4A' + 3^4A''$) electronic states. Therefore, an adiabatic path from ground state reactants to products can occur in the $1^2A'$ state as well as the $1^4A'$ state. The overall reaction was first explored with CAS calculations considering only the lowest doublet and lowest quartet PESs. For each step along a grid of small P-O bond lengths, the other degrees of freedom were optimized, resulting in the MEP presented in Figure 6.

Figure 6 presents the entrance barriers for the $P+O_2$ reaction in both spin states, ultimately leading to a nonlinear POO minimum. In the quartet state, a second barrier appears en route to the products, characterizing the mechanism as an overall oxygen abstraction. In contrast, the doublet state exhibits a discontinuity along the pathway, seemingly directing the system toward the OPO isomer, which corresponds to the global minimum. Despite various attempts, it was not possible to achieve a smooth potential energy profile using a single doublet electronic state.

Figure 6 – Minimum energy path for the P(^{4}S) + O$_2$($^3\Sigma_g^-$) → O(^{3}P) + PO($^2\Pi$) reaction calculated at CAS/AVTZ+d level for both doublet and quartet PESs.

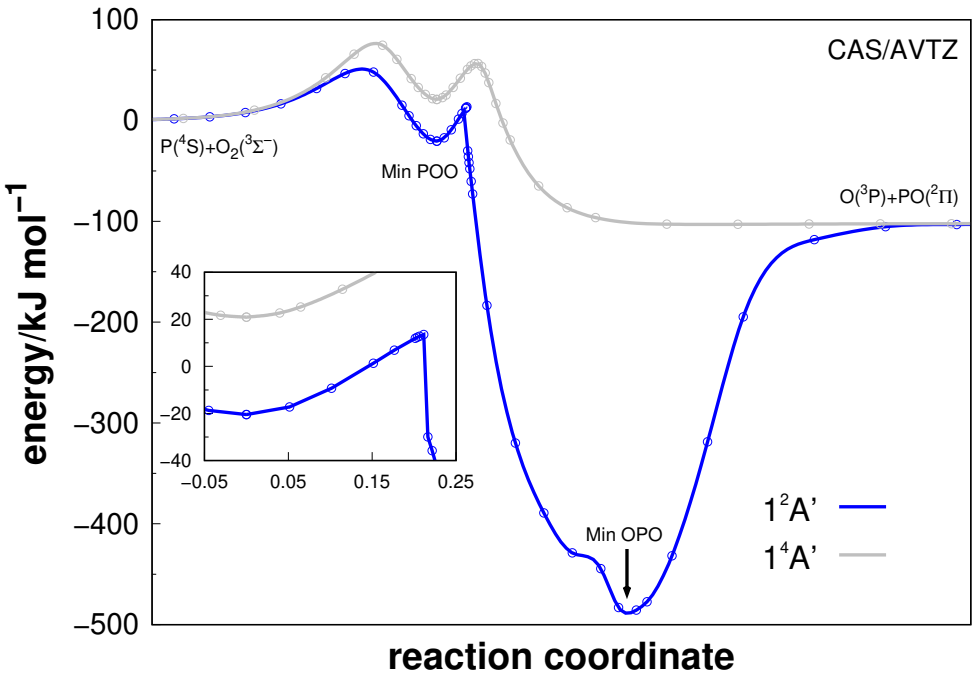

Caption: The inset shows the predicted discontinuity of the single-state CAS wave function for the POO→O+PO dissociation on the doublet PES.

As the convergence problems could be caused by the presence of low lying excited states, the decision to assess this possibility by including more electronic states was made. Reasonable results could only be obtained after performing state averaged calculations with four doublet states (see Figure 7).

From Figure 7, the doublet POO minimum, like its quartet counterpart, dissociates directly into the products rather than undergoing isomerization to OPO. The inclusion of four electronic states was required only for the description of this particular TS. Accordingly, the single-point MRCI(Q) energy for this structure was computed using a state-averaged CAS wave function. All other minima and transition states were treated at the single-state level using both CAS and MRCI(Q) methods.

The B3LYP-level calculations reported by Douglas et al. (2019), which considered only the doublet state, propose a reaction pathway proceeding as P+O$_2$ → POO → OPO → O+PO. However, DFT methods such as B3LYP may not reliably capture the dissociation behaviour of the POO intermediate. In contrast, the multistate CAS calculations carried out in this work, particularly those involving four electronic states, are expected to provide a more accurate description. Beyond these mechanistic differences, obtaining reliable values for the potential energy barriers is crucial for a proper understanding of the system's reactivity. For this reason, all energetic values presented from this point onward correspond to single-point MRCI(Q) calculations, including ZPE corrections.

Figure 7 – State-averaged CAS/AVTZ+d optimized cuts along the POO→O+PO dissociation including four A' doublet states.

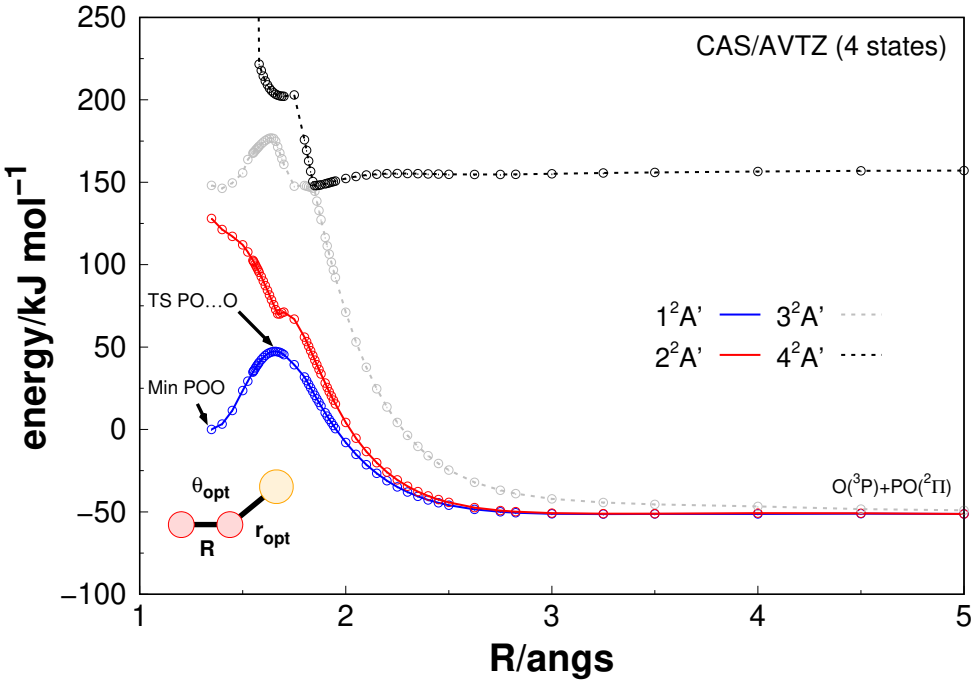

Caption: The reaction coordinate is defined as the O-O distance which is held fixed in the constrained optimizations.

An overall view of the doublet and quartet PESs is presented at the MRCI(Q) level in the potential energy diagram of Figure 8. The entrance barrier is predicted to be 10.1 kJ mol^{-1} for the doublet state and 28.9 kJ mol^{-1} for the quartet one, which is $\sim 3\times$ higher than the B3LYP one reported in Ref. Douglas et al. (2019).

In terms of the reaction mechanism, both the doublet and quartet PESs follow the same sequence of steps leading to the products, although the stationary points on the quartet surface consistently exhibit higher energies. While OPO minima were identified for both spin states, these intermediates do not actively participate in the reaction pathway. Instead, they dissociate directly and without a barrier into O+PO.

As shown in Figure 8, the initial step of the reaction (P+O_2 → POO)is the most critical in determining the overall mechanism. The energy barrier along the doublet potential energy surface (PES) for this step is expected to dominate the computed rate coefficient. Therefore, it was essential to verify the reliability of this barrier by performing MRCI(Q) PES scans along the POO → P+O_2 dissociation coordinate using larger basis sets (see Figure 9).

Figure 8 – Potential energy diagram for the formation of PO at the MRCI(Q)/AVTZ+d//CAS/AVTZ+d level.

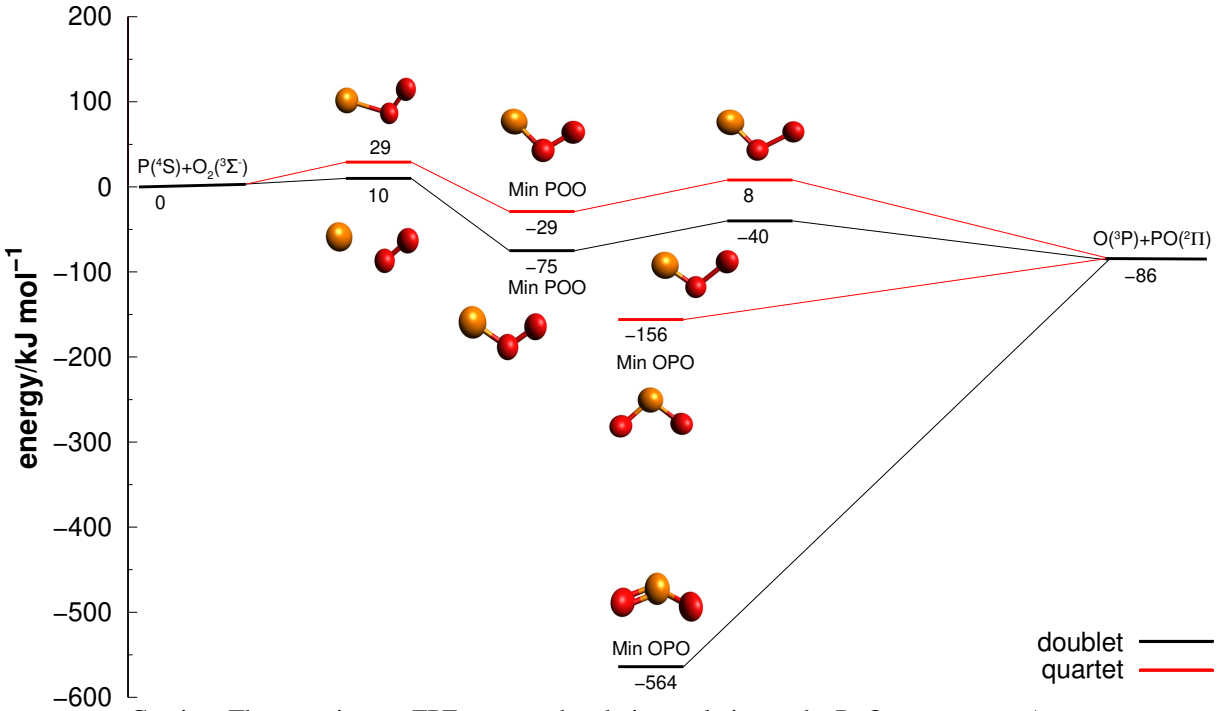

Caption: The energies are ZPE corrected and given relative to the P+O_2 asymptote. Atoms are colored as: oxygen (red); phosphorus (orange).

Without including ZPE, the predicted barriers were 15.2, 13.7 and 13.2 kJ mol^{-1}, using the AVTZ+d, AVQZ+d, AV5Z+d basis sets, respectively (see Figure 9). This shows that the results are converged within 4 kJ mol^{-1}. For both PESs, it was not possible to find a TS that connected the reactants to the OPO, or a barrier of isomerization from the POO minima to the OPO ones. The path that follows the formation of the POO minima, for both states, leads to the dissociated products. However, the activation barriers for the formation of the POO structures are very high, and their formation are unlikely of occuring, considering the low temperatures of the ISM. Unless, as it will be later mentioned, one is dealing with high temperature regions of space.

Figure 9 – Single-state MRCI(Q)/AVXZ+d//CAS/AVXZ+d ($X = T, Q, 5$) optimized cuts along the POO→P+O_2 dissociation on the ground $^2A'$ state.

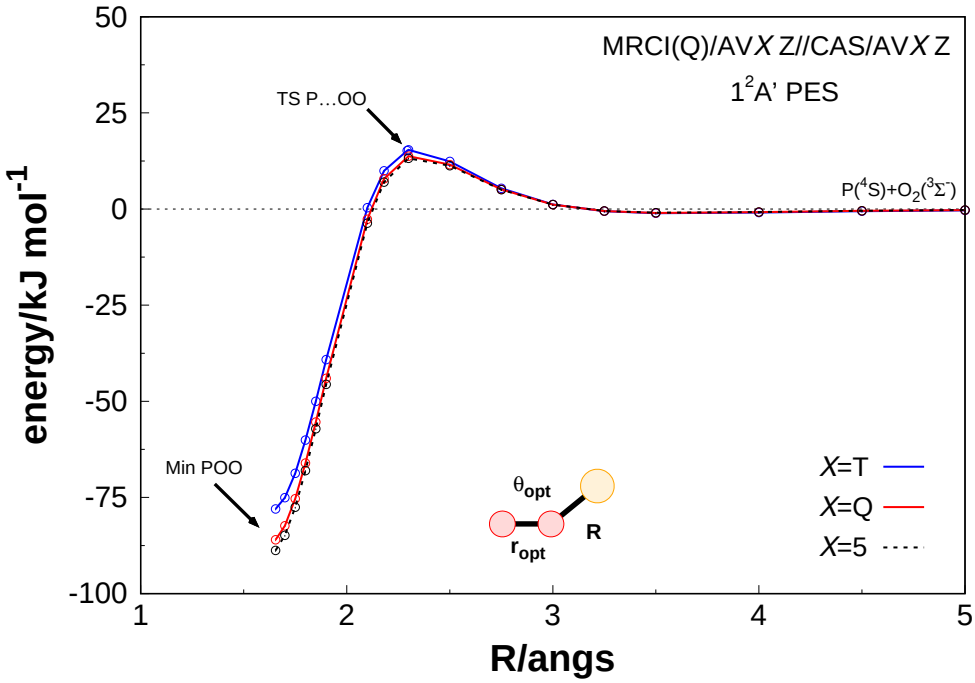

Caption: The reaction coordinate is defined as the P-O distance which is held fixed in the constrained optimizations.

4.1.2 Comparison between methods

The results using different levels of theory are gathered in Tables 5 and 6. They also include the B3LYP/AVQZ+d results reported by Douglas et al. (2019). To verify the possible multiconfigurational character of each structure, CCSD(T)-F12 calculations were performed at the optimized CAS geometries to obtain the T_1 diagnostic (LEE; TAYLOR, 1989; LEININGER et al., 2000; LEE, 2003). The coefficients (C_0^2) were also obtained from CASSCF calculations.

A T_1 diagnostic value exceeding 0.02 is generally taken as an indication of significant multireference character. Similarly, systems with strong multireference behavior typically exhibit C_0^2 values below 0.90. Based on these criteria, it was observed that (aside from the OPO minimum) all doublet-state structures display a notably high T_1 value alongside a low C_0^2 parameter. It is important to emphasize that the entrance barrier ($TS_{P+O_2 \rightarrow POO}$) on the doublet surface plays a crucial role in determining the reaction rate coefficient. This transition structure presents a pronounced multiconfigurational character, suggesting that both DFT and coupled-cluster methods may yield suboptimal performance in accurately describing it.

Table 5 – Properties of the stationary points of $1^2A'$ PESs at differents levels of theory and the $O(^3P)$+$PO(^2\Pi)$ asymptotic limit[a].

Structure	Method	E	T_1^b	C_0^{2c}
Min OPO	MRCI(Q)/AVTZ+d//CAS/AVTZ+d	-564.3		0.922
	CCSD(T)-F12/VTZ-F12//CAS/AVTZ+d	-604.3	0.028	
	M06-2X/AVTZ+d	-592.1		
	B3LYP/AVQZ+d[e]	-572.0		
Min POO	MRCI(Q)/AVTZ+d//CAS/AVTZ+d	-75.3		0.738
	CCSD(T)-F12/VTZ-F12//CAS/AVTZ+d	-90.1	0.064	
	M06-2X/AVTZ+d	-97.8		
	B3LYP/AVQZ+d[e]	-97.3		
$TS_{P+O_2\rightarrow POO}$	MRCI(Q)/AVTZ+d//CAS/AVTZ+d	10.1		0.467
	CCSD(T)-F12/VTZ-F12//CAS/AVTZ+d	-4.16	0.115	
	M06-2X/AVTZ+d	9.1		
	B3LYP/AVTZ+d[e]	3.1		
$TS_{POO\rightarrow O+PO}$ [d]	MRCI(Q)/AVTZ+d//CAS/AVTZ+d	-40.3		0.424
	CCSD(T)-F12/VTZ-F12//CAS/AVTZ+d	-51.4	0.061	
	M06-2X/AVTZ+d	0.9		
	B3LYP/AVQZ+d[e]	-		
$O(^3P)$+$PO(^2\Pi)$	MRCI(Q)/AVTZ+d//CAS/AVTZ+d	-86		
	CCSD(T)-F12/VTZ-F12//CAS/AVTZ+d	-98.5		
	M06-2X/AVTZ+d	-97.0		
	B3LYP/AVQZ+d[e]	-		

[a] All energies are given in kJ mol^{-1} relative to the P+O_2 asymptotic limit including ZPE correction.
[b] T_1 diagnostic.
[c] Magnitude of the dominant configuration in the CASSCF wave functions.
[d] State-averaged CAS with four A' states
[e] From reference Douglas et al. (2019)

Regarding the reaction energy, all levels of theory agree within 12 kJ mol^{-1}. For the barrier heights it can be noted that MRCI(Q) results agree well with the M06-2X ones, and a difference of only $\sim$ 1 kJ mol^{-1} in the doublet entrance barrier $TS_{P+O_2\rightarrow POO}$ was obtained. This is an interesting result, because even though this functional performs well for energy barriers, it does not show a good performance for cases with high multireference character (PEVERATI; TRUHLAR, 2012). The CCSD(T)-F12 method does not show an entrance barrier, while B3LYP predicts a barrier of only 3 kJ mol^{-1}. In the quartet state, the difference between the calculated entrance barriers at M06-2X and MRCI(Q) is 29 kJ mol^{-1}, while the difference between MRCI(Q) and CCSD(T)-F12 is 4 kJ mol^{-1}.

In the following step ($TS_{POO\rightarrow O+PO}$), while the doublet barrier lies below the reactants energy in MRCI (-40.3 kJ mol^{-1}), the quartet one is a little bit above it (8.4 kJ mol^{-1}). On contrary, at the M06-2X level, the doublet POO $\rightarrow$ O + PO barrier lies above the reactants (+0.9 kJ mol^{-1}), while the quartet one lies below (-7 kJ mol^{-1}). This TS, besides the fact that possesses a high T_1 diagnostic (0.061), also possesses an even lower C_0^2 parameter (0.424). The M06-2X path agrees with the MRCI ones in that the isomerization of POO into OPO is not accessible. This is not the case for the B3LYP results presented by Douglas et al. (2019).

Table 6 – Properties of the stationary points of $1^4A'$ PESs at differents levels of theory[a].

Structure	Method	E[a]	T_1^b	C_0^{2c}
Min OPO	MRCI(Q)/AVTZ+d//CAS/AVTZ+d	-156		0.926
	CCSD(T)-F12/VTZ-F12//CAS/AVTZ+d	-182.5	0.069	
	M06-2X/AVTZ+d	-188.3		
Min POO	MRCI(Q)/AVTZ+d//CAS/AVTZ+d	-29.2		0.935
	CCSD(T)-F12/VTZ-F12//CAS/AVTZ+d	-43.7	0.035	
	M06-2X/AVTZ+d	-63.9		
$TS_{P+O_2\rightarrow POO}$	MRCI(Q)/AVTZ+d//CAS/AVTZ+d	28.9		0.804
	CCSD(T)-F12/VTZ-F12//CAS/AVTZ+d	25.35	0.044	
	M06-2X/AVTZ+d	58.3		
$TS_{POO\rightarrow O+PO}$	MRCI(Q)/AVTZ+d//CAS/AVTZ+d	8.4		0.861
	CCSD(T)-F12/VTZ-F12//CAS/AVTZ+d	-2.58	0.033	
	M06-2X/AVTZ+d	-7.1		

[a] All energies are given in kJ mol^{-1} relative to the P+O_2 asymptotic limit including ZPE correction.
[b] T_1 diagnostic
[c] Magnitude of the dominant configuration in the CASSCF wave functions.

4.1.3 Reaction rates coefficients

$P(^4S) + O_2(^3\Sigma^-) \rightarrow O(^3P) + PO(^2\Pi)$ reaction has been experimentally studied by several groups (HUSAIN; NORRIS, 1977; HUSAIN; SLATER, 1978; CLYNE; ONO, 1982; HENSHAW et al., 1987; DOUGLAS et al., 2019), mostly at room temperature. The most recent experiments (DOUGLAS et al., 2019), however, provide the temperature dependence, which is essential to comprehend the role of this reaction in environments that possess high temperatures in space such as cirmcunstellar envelopes. Nevertheless, no accurate computations from first principles have been reported on this reaction, as far as it was searched on reference literature. For this reason, the MRCI(Q)/AVTZ+d//CAS/AVTZ+d results presented above were used to calculate the rate coefficients as a function of temperature using the MESS package. The results are presented in Figure 10, where both the calculated rate coefficients of this work and previously measured ones are compared for different temperatures. The lines are fit to the experimental/computational data, and the experimental one (in black) were taken from Douglas et al. (2019).

The results presented in this work show good agreement with the experimental findings of Douglas et al. (2019), Clyne and Ono (1982), and Henshaw et al. (1987). Nonetheless, it is important to note that the computational outcomes are highly sensitive to the height of the entrance barrier on the doublet potential energy surface, which was estimated to be 10 kJ mol^{-1}. This value could be subject to refinement with the inclusion of additional effects, such as core-electron correlation. Furthermore, employing methods like variational transition state theory (VTST) or quasi-classical trajectory simulations may lead to improved estimates of the reaction rates.

Figure 10 – Rate coefficients as a function of temperature for the $P(^4S) + O_2(^3\Sigma_g^-) \rightarrow O(^3P) + PO(^2\Pi)$ reaction.

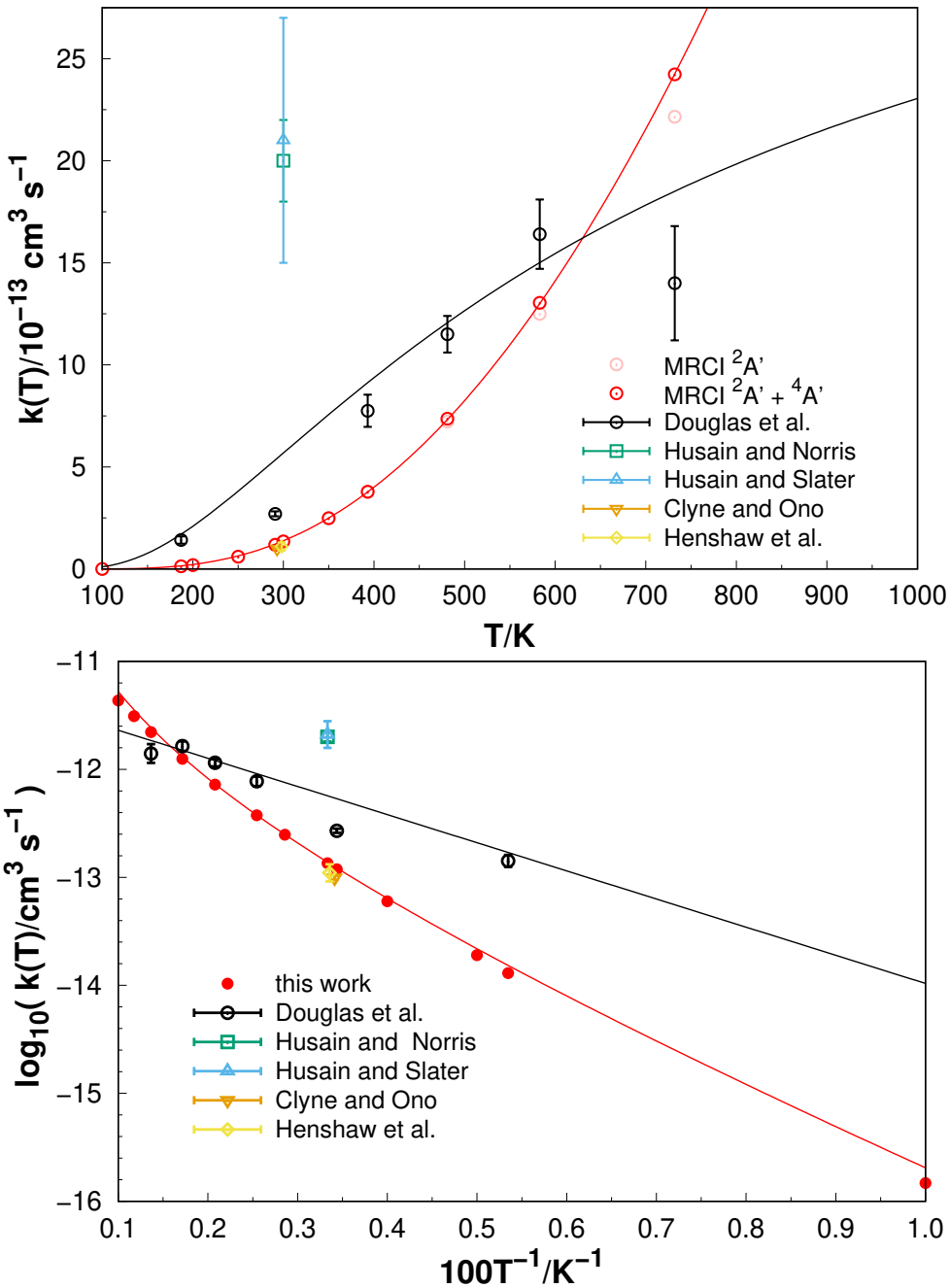

Caption: Experimental data refers to the following references: Douglas et al. (2019); Husain and Norris (1977); Husain and Slater (1978); Clyne and Ono (1982); Henshaw et al. (1987). The red lines corresponds to a fit to the results found in this work using a modified Arrhenius formula while the black one is the reported experimental temperature dependence of Douglas et al. (2019). The lower panel presents the same data in an Arrhenius plot.

Considering these two points, it is possible to arrive at interesting conclusions using the results obtained here. First, the quartet state will have a relevant contribution for higher temperatures, as shown in the upper panel of Figure 10. This is very relevant for the high temperatures achieved in CEs and shock regions of the ISM. A markedly different temperature dependence was observed when compared to the results reported by Douglas et al. (2019). However, it is important to highlight that the experimental data themselves exhibit some irregularities, and the trend inferred from their results may not extrapolate reliably to higher temperatures.

Their reported Arrhenius form $k(T) = (4.20 \times 10^{-12}) \exp(-600/\mathrm{T})\mathrm{cm}^3\mathrm{s}^{-1}$ suggests a barrier of 5 kJ mol^{-1}. However, it seems to be premature to make an assertive extrapolation of the rate coefficients for very high temperatures, and further progress on both computational and experimental sides would be welcome. Nevertheless, at 1000K the experiments point to a rate coefficient of $k(T) = 2.30 \times 10^{-11}\mathrm{cm}^3\mathrm{s}^{-1}$ while the calculations performed in this work yield $k(T) = 0.53 \times 10^{-11}\mathrm{cm}^3\mathrm{s}^{-1}$. A fit of the results to the Arrhenius equation yields $k(T) = 3.59 \times 10^{-11}\exp(-1939/\mathrm{T})\mathrm{cm}^3\mathrm{s}^{-1}$, which indicates a larger pre-exponential factor, and also a larger barrier. A fit of the results to the modified Arrhenius formula led to $\alpha = 1.44 \times 10^{-12}\mathrm{cm}^3\ \mathrm{s}^{-1}$, $\beta = 1.44$ and $\gamma = 704$ K.

After the results presented in this section were published (GOMES et al., 2022), two papers regarding this reactions came out in literature. In the paper published by Chen et al. (2023), they found a mechanism in accordance with the one reported here. Their barrier height is also consistent with the one presented here. Which in turn, led to the conclusion that their method is accurate. They did not consider the contribution from the quartet state, because of the high computational cost. Therefore the constants found at very high temperatures may be underestimated. Finally, they concluded that their results are consistent with the Arrhenius linear behaviour at relatively low temperatures found in this work and encourage further experiments for the calculation of the rate constants of this reaction.

In the work of Concepción et al. (2024), they revisited the reaction studied in this section, also from a theoretical aspect. Although there are some differences in the results found by this group, such as the existence of prereactive complex for both doublet and quartet PESs (which cannot be stabilized in low and medium pressure regimes, and therefore, do not possess great influence on the kinetics of the reaction), they found a similar entrance barrier height for the doublet state (8.5 kJ mol^{-1}). Their results also supports the fact that, at high temperatures, the quartet state reaction is relevant, and should be considered. Their final reported rate coefficient can be expressed, using the modified Arrhenius Equation, as $\alpha = 1.5 \times 10^{-12}\mathrm{cm}^3\ \mathrm{s}^{-1}$, $\beta = 1.8$ and $\gamma = 516.5$ K, which is in good agreement with the one reported here. Applying their results to a chemical model, they reachead the conclusion that the abundance of PO in high-velocity shocks is dominated by the reaction P+OH, and in regions where shock speeds are slower, the reaction studied in this section of this work dominates the formation of PO. In the end, like

the previous work mentioned (CHEN et al., 2023), they also state that additional experiments, particularly at low temperatures, are needed.

4.2 $N(^4S) + PN(^1\Sigma^+) \rightarrow N_2(^1\Sigma_g^+) + P(^4S)$

4.2.1 Potential energy surface and reaction mechanism

The potential energy diagram presented in Figure 11 summarizes the possible mechanisms and compares the different computational approaches used in this section of the work. The discussion that follows is based on MRCI+Q/AVTZ+d//CAS/AVTZ+d results unless stated otherwise.

Figure 11 – Potential energy diagram for the destruction of PN by nitrogen atoms.

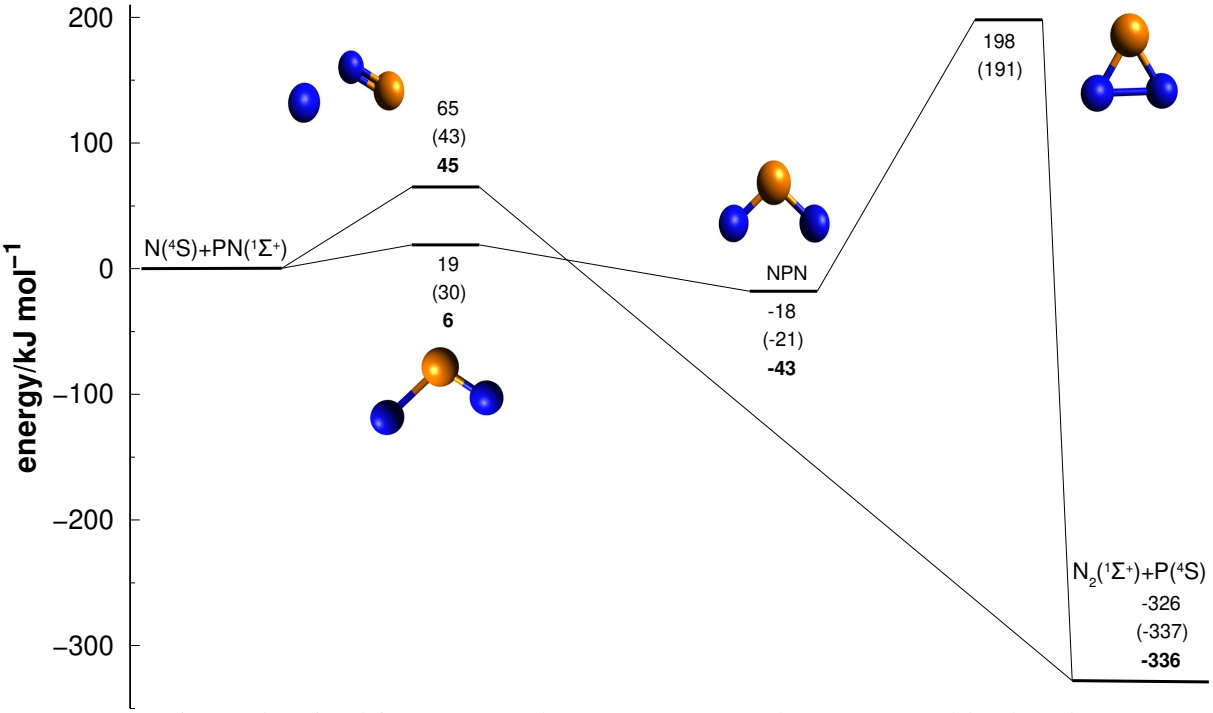

Caption: Values in plain text are at the MRCI+Q/AVTZ+d//CAS/AVTZ+d level, under parenthesis at the CCSD(T)-F12/VTZ-F12 and bold are M06-2X/AVTZ+d. The energies are ZPE corrected and given relative to the $N(^4S) + PN(^1\Sigma^+)$ asymptote. Atoms are colored as: nitrogen (blue); phosphorus (orange).

Regarding the thermochemistry of the reaction, it can be noted that the $N(^4S) + PN(^1\Sigma^+)$ reaction is very exothermic, releasing 326 kJ mol^{-1} after the formation of the strong triple bond of molecular nitrogen. Therefore, one can say that this reaction is thermodynamically favorable. However, as it will be noticed later, the kinetics of the reaction provides a different outcome.

Analysing Figure 11, it can be noted that there are two possible mechanisms for the destruction of PN molecules and formation of $N_2(^1\Sigma^+) + P(^4S)$: a direct N-atom abstraction mechanism and another passing through the NPN intermediate. Beggining from the N+PN reactants, the entrance barrier for the formation of the NPN minimum is the lowest (19 kJ mol^{-1}

above reactants). However, this minimum has the two nitrogen atoms farther apart and the formation of the N_2 molecule from there needs to surpass a high potential energy barrier of 198 kJ mol^{-1} above reactants. Even though the direct mechanism also possesses an activation barrier, this is the preferred mechanism, since the overall activation energy is 65 kJ mol^{-1}.

The T_1 diagnostic, the M diagnostic and the magnitude of the dominant configuration in the CI wave functions (C_0^2) were collected for this system, which are given in Table 7, in order to verify the multireference character of the system. As already mentioned, a T_1 diagnostic higher than 0.02, a C_0^2 lower than 0.90 and, for this particular system, a M diagnostic higher than 0.10 are considered indicatives that the system possesses multireference character.

Table 7 – Properties of the stationary points of $1^4A'$ PES at differents levels of theory[a].

Structure	Method	E[a]	T_1[b]	C_0^2[c]	M[d]
Min NPN	MRCI+Q/AVTZ+d//CAS/AVTZ+d	-18		0.763	0.146
	CCSD(T)-F12/VTZ-F12//M06-2X/AVTZ+d	-21	0.048		
	M06-2X/AVTZ+d	-43			
$TS_{N+PN\rightarrow N_2+P}$	MRCI+Q/AVTZ+d//CAS/AVTZ+d	65		0.768	0.125
	CCSD(T)-F12/VTZ-F12//M06-2X/AVTZ+d	43	0.036		
	M06-2X/AVTZ+d	45			
	CCSD(T)/CBS//M06-2X/AVTZ+d	69			
$TS_{N+PN\rightarrow NPN}$	MRCI+Q/AVTZ+d//CAS/AVTZ+d	19		0.773	0.113
	CCSD(T)-F12/VTZ-F12//M06-2X/AVTZ+d	30	0.033		
	M06-2X/AVTZ+d	6			
$TS_{NPN\rightarrow N_2+P}$	MRCI+Q/AVTZ+d//CAS/AVTZ+d	198		0.753	0.154
	CCSD(T)-F12/VTZ-F12//CAS/AVTZ+d	191	0.089		
	M06-2X/AVTZ+d	-			
$N_2(^1\Sigma^+) + P(^4S)$	MRCI+Q/AVTZ+d//CAS/AVTZ+d	-326			
	CCSD(T)-F12/VTZ-F12//CAS/AVTZ+d	-337			
	M06-2X/AVTZ+d	-326			
	CCSD(T)/CBS//M06-2X/AVTZ+d	-341			

[a] All energies are given in kJ mol^{-1} relative to the N+PN asymptotic limit including ZPE correction.
[b] T_1 diagnostic
[c] Magnitude of the dominant configuration in the CI wave functions .
[d] M diagnostic

Analysing the values for the NPN minimum and the $TS_{NPN\rightarrow N_2+P}$, which are related with the less favorable mechanism, a very high MR character could be detected. This TS, actually, could not be found in the DFT approach, and the CCSD(T) approach would not be reasonable. On contrary, the direct mechanism, considered the preferred one, passing through the $TS_{N+PN\rightarrow N_2+P}$ demonstrates a substantial MR character, but not as great as the other structures. For this preferred mechanism, the energies were calculated using different levels of *ab initio* calculations for comparison.

Table 7 and Figure 11 demonstrate that, for the two steps mechanism, passing through the NPN minimum, the MRCI+Q energies agree reasonably well with the CCSD(T)-F12 ones (within 11 kJ mol^{-1}). The TS from NPN $\rightarrow$ N_2 + P could not be found within the DFT approach and the CCSD(T)-F12/VTZ-F12 energy for this structure was obtained with the CASSCF/AVTZ+d

geometry. Nevertheless, this TS possesses the highest MR character of all the structures involved in the potential energy surface.

When it comes to the direct mechanism, the N + PN $\rightarrow$ N_2 + P barrier at the CCSD(T)-F12 level deviates more when compared with the MRCI+Q one, being 22 kJ mol^{-1} lower. However, besides the fact that the high MR character makes CCSD and DFT methodologies not trustworthy for describing this system, the CCSD(T)-F12/VTZ-F12 calculations are unrestricted but based on a restricted open shell Hartree-Fock reference (the only option in MOLPRO). This fact can explain the difference for the N + PN $\rightarrow$ N_2 + P barriers showed in Figure 11, when the CCSD(T)-F12/VTZ-F12 results are compared with the MRCI-F12/AVTZ+d//CAS/AVTZ+d ones.

To verify if this was indeed the motive for this difference, CCSD(T)/CBS//M06-2X/AVTZ+d calculations were performed on ORCA (which allows using UHF as a reference) and they provided a barrier in perfect agreement with the MRCI+Q one (69 kJ mol^{-1}). Therefore, an important conclusion that can be made from these results is that the N + PN $\rightarrow$ N_2 + P barrier of 65 kJ mol^{-1} is reliable. It is important to remember that this is the preferred mechanism, and this barrier height will dominate the quality of the rate coefficients results. In the next section, a further improvement made in this barrier height will be presented.

4.2.2 Reaction rates coefficients

Figure 12 shows the calculated rate coefficients for the abstraction mechanism from 900 to 4500 K using different *ab initio* data and TST methods. The upper panel presents an Arrhenius plot and the lower one shows a conventional $k \times T$ version of the same data.

It can be noticed from Figure 12 that the rate coefficients are highly temperature dependent, and are not relevant under temperatures lower than 1000 K. This result means that this collision can only be effective in environments of high temperatures, such as CEs and shock regions. The rate coefficient available in the astrochemical databases (MILLAR et al., 2024; WAKELAM et al., 2024) is fixed at 1.00×10^{-18}cm^3 s^{-1} and does not present a temperature dependency, and for this reasons the models performed so far neglected this reaction. However, the results presented in this section of the work show that this reaction cannot be neglected, since, given the fact that observations indicate that the maximum temperature in molecular shocks can reach values as high as 4000 K or more (LEFLOCH et al., 2016; DOUGLAS; GOBRECHT; PLANE, 2022), this reaction is relevant at such high temperatures, and should be included in the astrochemical models, with potential impact on the abundance of PN.

Figure 12 – Rate coefficients as a function of temperature for the N + PN → N_2 + P reaction.

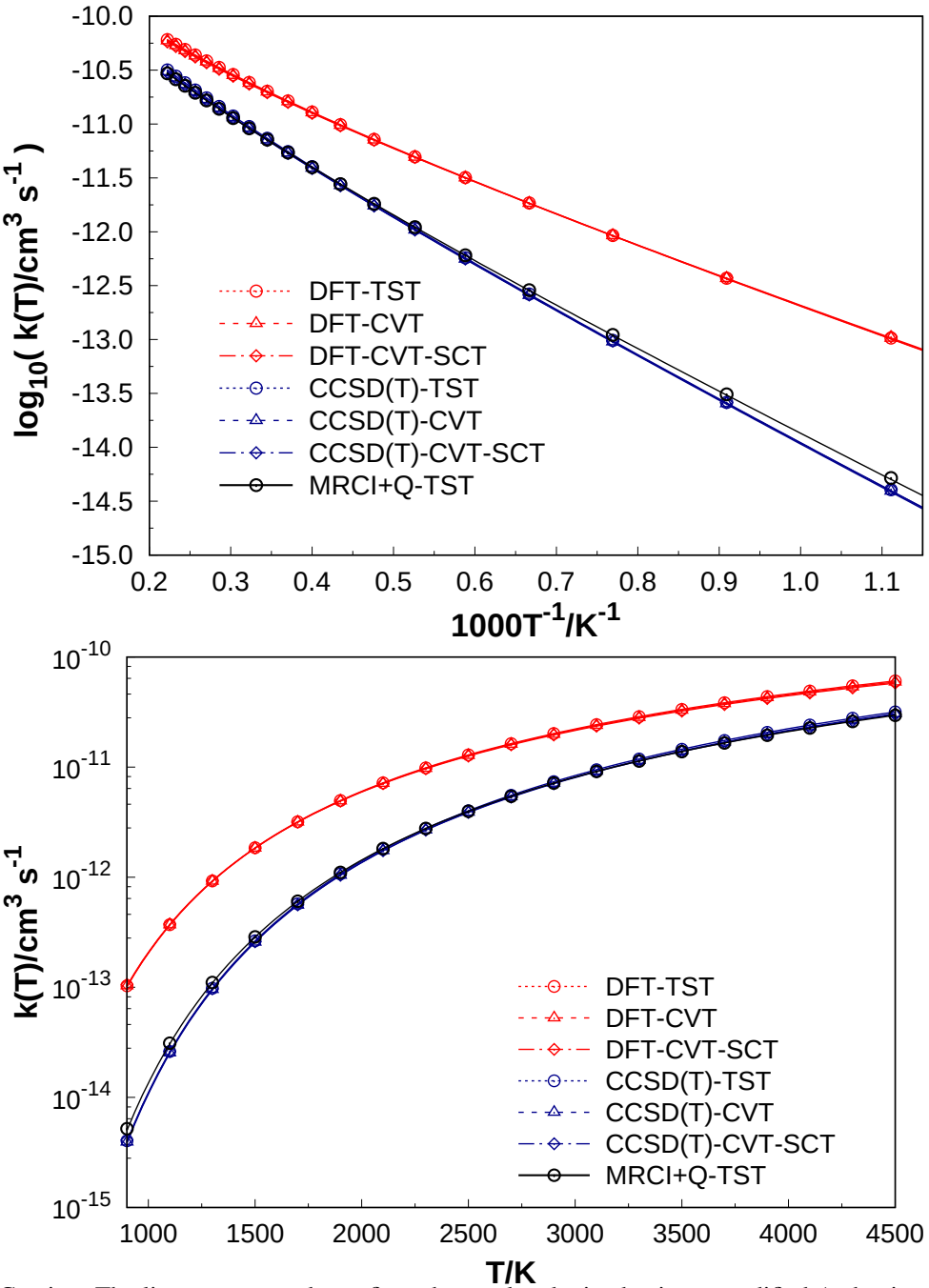

Caption: The lines correspond to a fit to the results obtained using a modified Arrhenius formula. The lower panel presents the same data for a better visualization of temperature dependence.

Another result that can be seen in Figure 12 is that both DFT and CCSD(T) methodologies demonstrate that tunneling effects and variational treatment of this system do not influence in the final result. This is important, since TST calculations are more computationally feasible and can be performed using the MRCI+Q results as well. Aiming to obtain an extra precision in the value of the rate, geometry optimizations and frequencies calculations at the MRCI+Q/AVTZ+d level for this mechanism (instead of relying on CASSCF geometries) were performed. With the new

obtained energies there was an increase of ~ 2 kJ mol^{-1} in the barrier height. Considering the precision of the methods, this is a satisfactory result.

At the higher temperature of 4500 K, the DFT-CVT-SCT rate coefficient is 5.79×10^{-11}cm^3 s^{-1}, the CCSD(T)-CVT-SCT is 2.99×10^{-11}cm^3 s^{-1}. With MRCI+Q/AVTZ+d energies and frequencies, the rate is 2.95×10^{-11}cm^3 s^{-1}, which agrees well with the CCSD(T) ones. Considering all the results and methodologies employed in this reaction, it can be considered that the best estimate for the rate coefficient is given by the MRCI+Q/AVTZ+d optimized level using the standard TST method.

The reaction rate coefficients obtained were fitted to the modified Arrhenius equation. Table 8 gathers the results using the different methodologies employed in this section of the work. As it can be noticed, all TST methodologies agreed very well, converging to the same results at the high temperature limit.

Table 8 – Rate coefficients as a function of temperature for the different methodologies studied in this section of the work using a Modified Arrhenius equation fit (NPN).

	k(T) / cm^3 s^{-1}
DFT-CVT-SCT	$1.35\times10^{-11}(T/300)^{0.98}\exp(-5350/T)$
CCSD(T)-CVT-SCT	$1.33\times10^{-11}(T/300)^{0.98}\exp(-8280/T)$
MRCI+Q-TST	$1.04\times10^{-11}(T/300)^{1.02}\exp(-7659/T)$
MRCI+Q-TST[a]	$1.09\times10^{-11}(T/300)^{1.02}\exp(-7919/T)$
UMIST and KIDA[b]	1.00×10^{-18}

[a] Improved by geometry optimization and frequencies also at the MRCI+Q level.
[b] Millar, Bennett and Herbst (1987)

When the different methods of calculation are compared, the difference between the DFT curves and the other comes from the fact that DFT methodology led to a smaller barrier. However, as it was already discussed, the MRCI+Q results are more reliable. It is also worth mentioning that, with MRCI+Q/AVTZ+d energies, the results became even closer to the CCSD(T)/CBS//M06-2X/AVTZ+d ones.

4.3 $P(^4S)+NH(^3\Sigma^-) \rightarrow H(^2S)+PN(^1\Sigma^+)$ and $N(^4S)+PH(^3\Sigma^-) \rightarrow H(^2S) + PN(^1\Sigma^+)$

4.3.1 Potential energy surface and reaction mechanisms

Although these reactions can occur either on doublet, quartet or sextet potential energy surfaces (PESs), the ground state products [$H(^2S)+PN(^1\Sigma^+)$] can only be achieved adiabatically in the doublet state (Wigner-Witmer rules), and therefore the discussion focuses mainly on the doublet PES. The main stationary structures obtained in this work and their connections are summarized in Figure 13, while Table 9 gathers the geometries, energies and parameters of multireference character of all minima and TSs found.

Figure 13 – Potential energy diagram for the doublet state state of HPN.

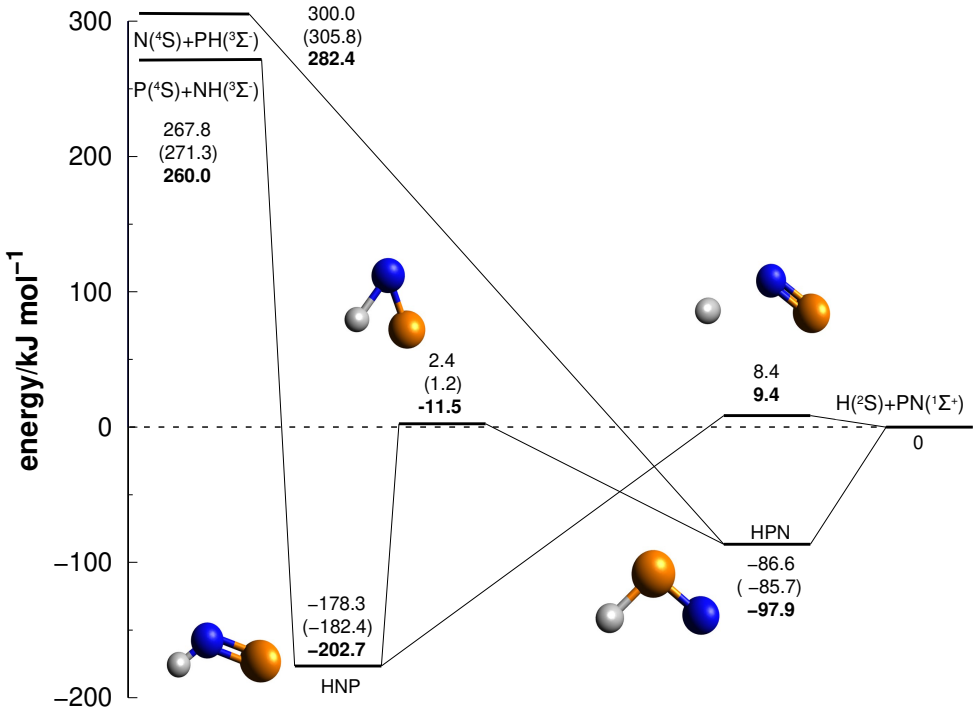

Caption: Energies are given relatively to the H+PN asymptote and are ZPE corrected. The MRCI-F12 energies are given as plain numbers, while the CCSD(T)-F12 and M06-2X ones results given under parenthesis and in boldface, respectively. Atoms are colored as: hydrogen (white); nitrogen (blue); phosphorus (orange).

As it can be seen in Figure 13, the CCSD(T)-F12 and MRCI-F12 energies agree well, with deviations in the relative energies lying below 6 kJ mol^{-1}, which is about the expected accuracy of these high level methods. The M06-2X results are also in qualitative agreement, with the exception of the HNP structure.

Table 9 – Properties of the stationary structures of the doublet HPN PES[a].

	R_{PH}	R_{NH}	R_{PN}	E	$C_0^{2\ b}$	T_1 [c]
Stationary points						
HNP	2.26	1.03	1.57	-178.3	0.931	0.025
HPN	1.45	2.35	1.58	-86.6	0.919	0.041
$TS_{HNP\rightarrow HPN}$	1.49	1.46	1.62	2.4	0.903	0.036
$TS_{HNP\rightarrow H+PN}$	2.77	1.67	1.52	8.4	0.879	-
Asymptotic limits						
$N(^4S)+PH(^3\Sigma^-)$	1.44	-	-	300.0	-	-
$P(^4S)+NH(^3\Sigma^-)$	-	1.05	-	267.8	-	-
$H(^2S)+PN(^1\Sigma^+)$	-	-	1.51	0	-	-

[a] Interatomic distances are given in Å and energies in kJ mol^{-1} relative to the H+PN limit. The energies are ZPE corrected and given at the MRCI-F12/AV*T*Z+d//CAS/AV*T*Z+d level.
[b] Magnitude of the dominant configuration in the CASSCF wave functions.
[c] T_1 diagnostic obtained through CCSD(T)/AV*T*Z+d calculations.

As it can be seen in Table 9, the HPN system does not possesses a high MR character when we analyse the C_0^2 parameter. The only exception is the $TS_{HNP\rightarrow H+PN}$. However, regarding the T_1 diagnostic both HPN minimum and $TS_{HNP\rightarrow HPN}$ structures possess a considerable MR character. Interestingly, the CCSD(T)-F12 results are nevertheless very close to the MRCI-F12 ones. Since the two high level methods agree very well, for simplicity, only the MRCI-F12/AVTZ+d//CAS/AVTZ+d values will be used in the following discussion.

The N+PH → H+PN and P+NH → H+PN reactions are exothermic by 300 and 268 kJ mol^{-1}, respectivelly. The difference between the two numbers is due to NH having a deeper potential well than PH. Given the isovalency of nitrogen and phosphorus, both reactions are analogous to the N+NH → H+N_2 one. However the latter is more than two times more exothermic, due to the strong triple bond present in molecular nitrogen. Another difference is the presence of two deep minima in the HPN PES, while HN_2 only displays a shallow minimum which lies higher in energy than the H+N_2 limit (WALCH; DUCHOVIC; ROHLFING, 1989; MOTA; VARANDAS, 2007; MOTA; VARANDAS, 2008; MOTA et al., 2020).

In principle, collisions starting on the quartet PES, which is also possible, could contribute to the overall reactivity if they could achieve the doublet state after a collision complex is formed, and from there dissociate to the ground state products. This would be more likely if the quartet and doublet PESs crossed each other along the reaction coordinate, and for this reason, such a crossing was searched.

Figure 14 – Search for intersystem crossing regions between doublet and quartet potential energies surfaces (N+PH).

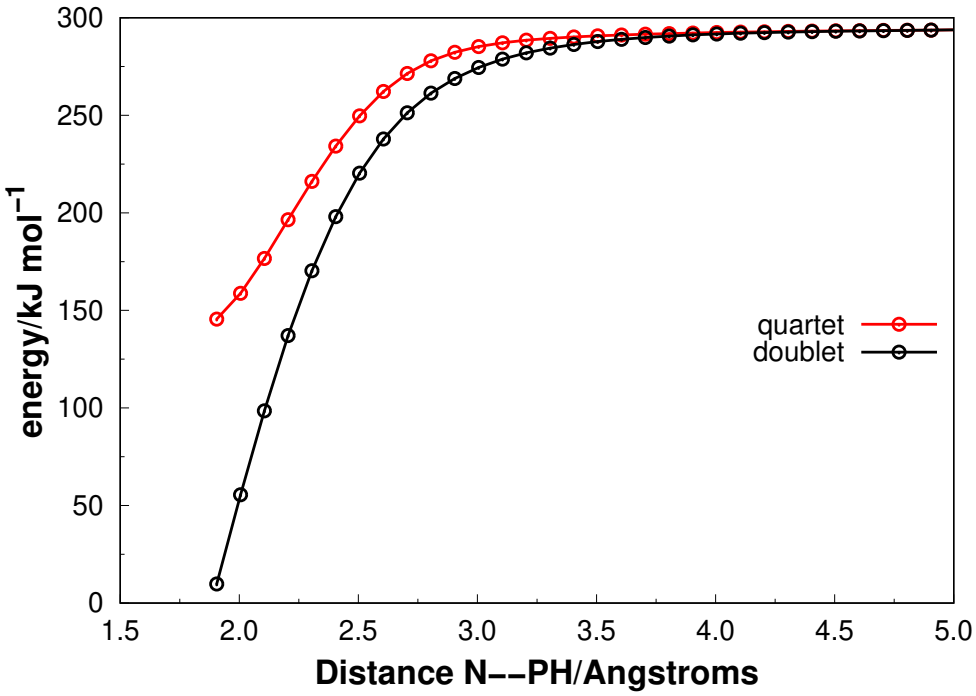

Caption: Energies are given relative to the H(^{2}S)+PN($^1\Sigma^+$) channel.

At the MRCI-F12/AV*T*Z+d//CAS/AV*T*Z+d level, potential energy surface scans for the N+PH → HPN and P+NH → HNP attacks were performed by relaxing the valence angle and diatomic distance along the path for the quartet state, followed by a single point energy calculation for both doublet and quartet states (at the optimized quartet geometries). This would allow to show a crossing lying on the MEP from the reactants to the quartet minima. However, as it can be noted in Figures 14 and 15, no such crossing could be found. It was also found that the quartet minima lie much higher in energy than the doublet ones.

For reaction N+PH it was found that the mechanism begins with a barrierless capture towards the formation of the HPN minimum, which lies 387 kJ mol^{-1} below the initial reactants. This structure may go through a barrierless hydrogen loss, or isomerize to the global minimum HNP with a barrier of 89 kJ mol^{-1} (2.4 kJ mol^{-1} relative to the final products). If isomerization occurs, the HPN structure can either suffer a hydrogen loss, leading to an indirect mechanism such as N+PH → HPN → PNH → H+PN, or alternatively yield P+NH. The latter process will lead to different and less exoergic products than formation of PN, and should occur with a lower probability. It is worth recalling that the destruction of the PH molecule via N+PH towards H+PN is available in the astrochemical databases, and these results supports the assumption that this reaction is fast at low temperatures, since it does not involve any step requiring energies higher than that of the reactants.

Figure 15 – Search for intersystem crossing regions between doublet and quartet potential energies surfaces (P+NH).

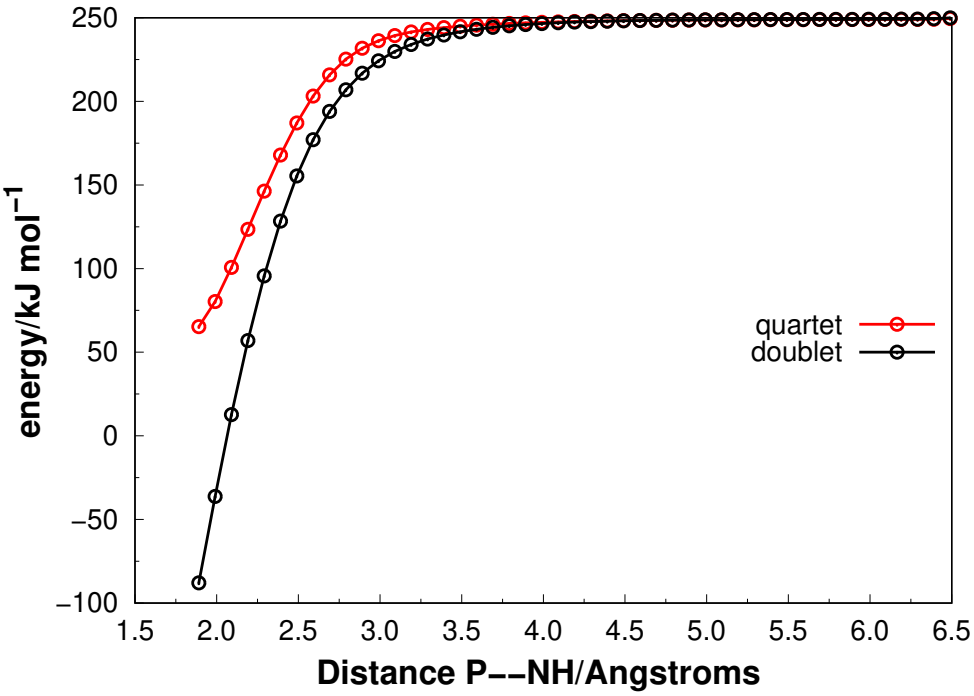

Caption: Energies are given relative to the H(^{2}S)+PN($^1\Sigma^+$) channel.

A negligible barrier for hydrogen loss from HPN above the H+PN channel of 2.3 kJ mol^{-1} was found (Figure 16), lying below the accuracy of the calculations performed here and, therefore, is not given in Figure 13. The presence of such barrier would not change the final rate coefficients, as it lies well below reactants.

For the P+NH collisions, it was found that they also occur without an initial activation barrier and lead to the HNP global minimum. Similarly to the previous one, after HNP formation, it may go directly to the PN products by hydrogen loss, but this time with a barrier of 187 kJ mol^{-1} (8.4 kJ mol^{-1} relative to the final products), or either isomerize with a barrier of 181 kJ mol^{-1}. Within the CCSD(T) approach the $TS_{HNP\rightarrow H+PN}$ was not found, maybe due to its MR character. The destruction of the NH molecule by atomic phosphorus may be an important source of interstellar PN, and this reaction is not available in most astrochemical database yet. As it will be discussed later, these rate coefficients have been very recently estimated (DOUGLAS; GOBRECHT; PLANE, 2022).

Figure 16 – Minimum energy path from HPN towards the H+PN channel.

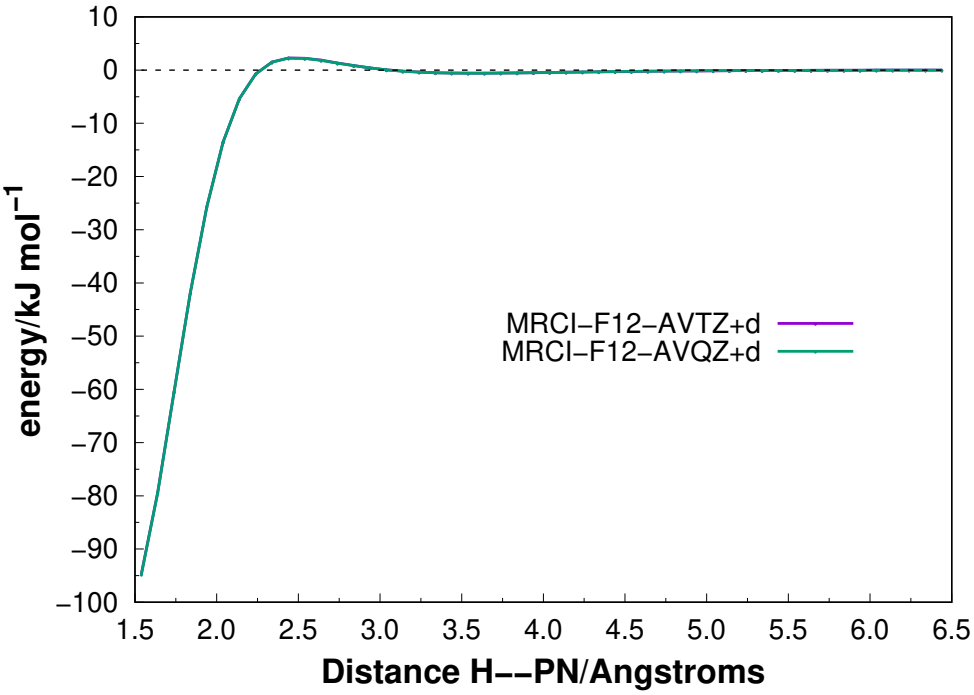

4.3.2 Reaction rates coefficients

The rate coefficient for the N(^{4}S) + PH($^3\Sigma^-$) reaction found in the astrochemical databases was estimated (SMITH; HERBST; CHANG, 2004) mainly based on the chemical similarity with the reaction N(^{4}S) + NH($^3\Sigma^-$). This latter had its rate coefficient studied theoretically (CARIDADE et al., 2005; MILLER et al., 1985) and experimentally (HACK; WAGNER; ZASYPKIN, 1994; MILLER et al., 1985).

Using the modified Arrhenius formula, the rate coefficient reported by Smith, Herbst and Chang (2004), at the temperature range of 10-300 K, is of $\alpha = 5.00 \times 10^{-11}$cm^3 s^{-1} ($\beta$ and $\gamma = 0.00$ K). This high rate coefficient that has been estimated indicates that this reaction is possibly relevant in the cold environments of the ISM. However, accurate theoretical calculations or experimental data are relevant for a confirmation of the assumptions made and for a better understanding of the role of this reaction in modelling the PN abundance in the ISM. The rates were calculated in this work using direct variable reaction coordinate transition state theory (KLIPPENSTEIN, 1991; KLIPPENSTEIN, 1992) (VRC-TST). Figure 17 shows the rate coefficients for both N+PH $\rightarrow$ H+PN and P+NH $\rightarrow$ H+PN reactions.

Figure 17 – Rate coefficients as a function of temperature (HPN).

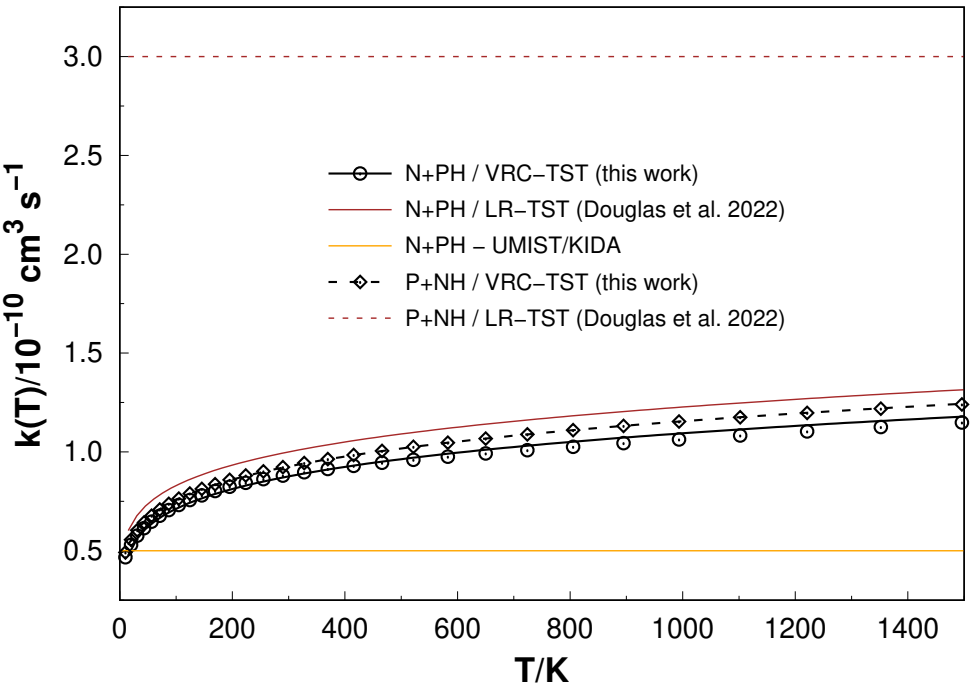

Caption: The points refer to the calculated values at fixed temperatures, while the curves are fits to the modified Arrhenius expressions. Solid lines correspond to the N+PH → H+PN reaction, while dashed lines correspond to the P + NH → H+PN. The VRC-TST results obtained in this work are shown in black, while those calculated by Douglas, Gobrecht and Plane (2022) are brown. The values currently in use in the major astrochemical databases for N+PH reaction is in orange.

The results indicate that both have similar rate coefficients, with the P+NH slighly higher, possibly due to a more attractive interaction between reactants due to the higher polarizability of the P atom. A fit to the modified Arrhenius equation led to $\alpha = 0.88 \times 10^{-10}$cm^3 s^{-1}, $\beta = 0.18$ and $\gamma = 1.01$ K for N+PH and $\alpha = 0.93 \times 10^{-10}$cm^3 s^{-1}, $\beta = 0.18$ and $\gamma = 0.24$ K for P+NH. The low values of β indicate a proximity to a simple Arrhenius behavior, while the low values of γ reflect the barrierless character of the reaction.

A recent work by Douglas, Gobrecht and Plane (2022) calculated the rate coefficients for both reactions studied in this section, using long-range transition state theory (GEORGIEVSKII; KLIPPENSTEIN, 2005) (LR-TST). Their reported rates are also given in Figure 17 for comparison. Differently from the VRC-TST results obtained in this section of the work, their values show that the rate coefficient for reaction P+NH is about three times higher than N+PH, with no temperature dependence for the former. Nevertheless, their results for N+PH agree well with the ones presented here. Since the VRC-TST method is more reliable, one can say that the results presented here should be more accurate. While the results already in use in the UMIST (MILLAR et al., 2024) and KIDA (WAKELAM et al., 2024) databases agree well with the calculated ones for the N+PH reaction below 100 K, for high temperatures the results are about twice as high.

The possibility of N+PH → P+NH (which is also slighly exothermic and barrierless) and its reverse one were also checked, and the rate coefficients are gathered in Figure 18. However

the results found here show that the rate coefficient for this reaction at the temperature of 328 K (0.57×10^{-12}cm^3 s^{-1}) is 157 × lower than the N+PH → H+PN one, and therefore should not be relevant and contribute to the branching ratio. The reverse reaction is slightly endothermic and shows a typical Arrhenius behavior of a reaction that possesses an activation energy.

Figure 18 – Rate coefficients as a function of temperature for the P+NH → N+PH (black) and N+PH → P+NH (blue) reactions.

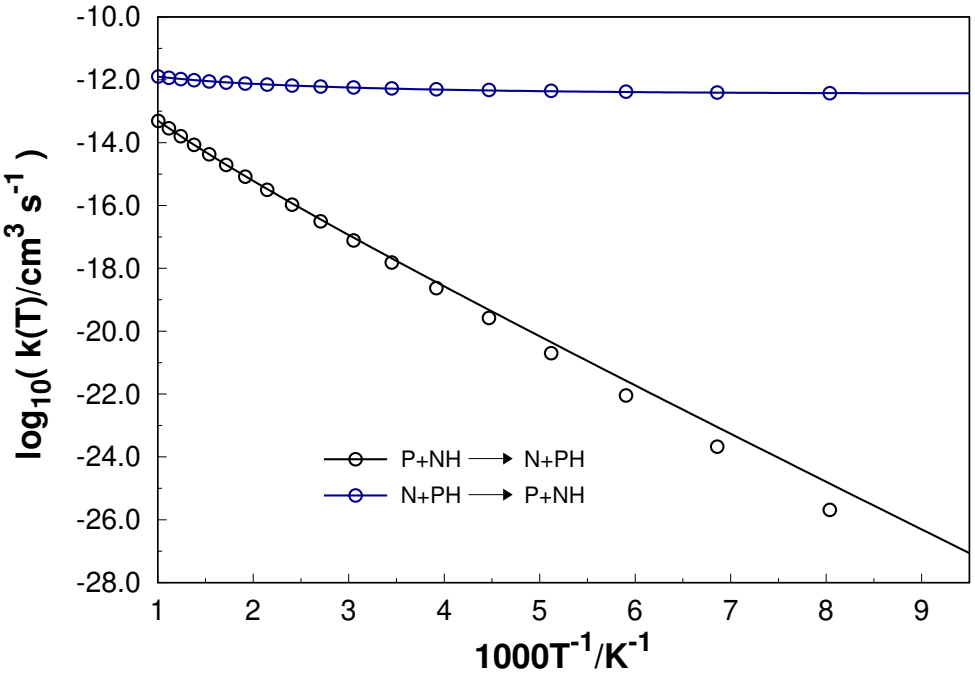

Caption: The points refer to the calculated values at fixed temperatures, while the curves are fits to the modified Arrhenius expressions.

4.3.3 Destruction of PN by H atoms in high temperature regions

PN is also present in high temperature environments. A recent work published regarding one of the reactions discussed and treated on this thesis (N+PN) (GOMES et al., 2023b) showed for the first time that in such high temperature environments, atomic nitrogen plays an important role in the destruction, and therefore, the respective abundance of PN molecules. That being noticed, it would be interesting to see at what temperature this molecule can be destructed by H atoms, which is the most abundant atomic species in space. However, as it can be seen in Figure 19, the rate coefficients are very low, even at 5000 K, making this destruction route a not particularly important one. A comparison of these results with the ones reported by Douglas, Gobrecht and Plane (2022) was made, and apart the expected differences coming from the different methods of calculation, the same qualitatively conclusions can be achieved.

Figure 19 – Rate coefficients as a function of temperature for the destruction of PN by H atoms.

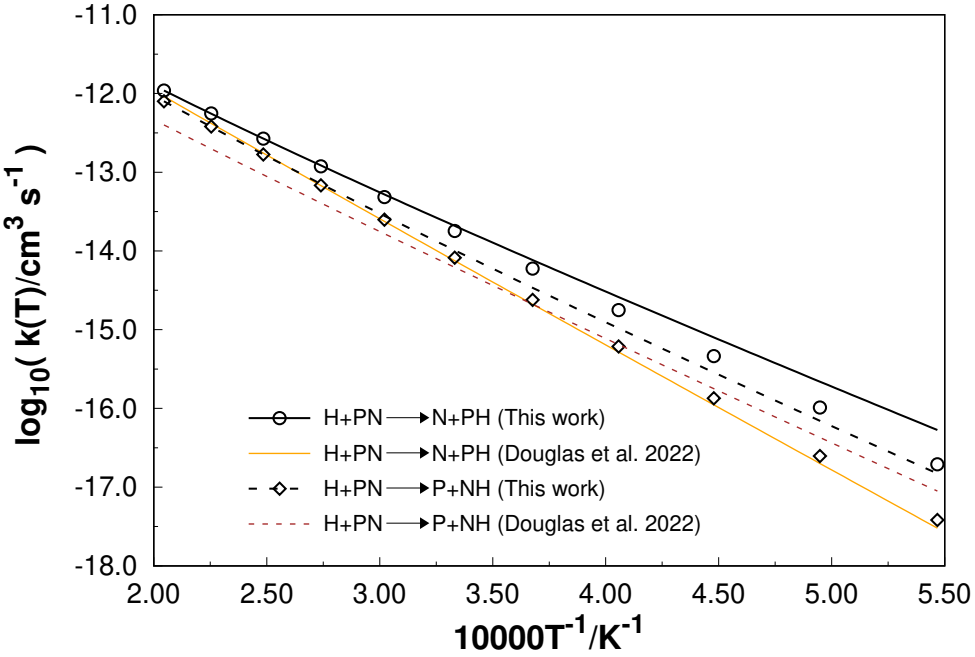

Caption: The points refer to the calculated values at fixed temperatures, while the curves are fits to the modified Arrhenius expressions. Solid lines correspond to the H+PN → N+PH reaction, while dashed lines correspond to the H+PN → P+NH. MESS results calculated here are shown in black, while those calculated by Douglas, Gobrecht and Plane (2022) are orange and brown for the respective mentioned reactions.

Table 10 gathers the rate coefficients as a function of temperature for all reactions studied in this part of the work and discussed in this and in the previous sections, using a modified Arrhenius equation fit.

Table 10 – Rate coefficients as a function of temperature for all reactions studied in this section of the work using a modified Arrhenius equation fit (HPN).

	k(T) / $cm^3\ s^{-1}$
N+PH → H+PN	$0.88\times10^{-10}(T/300)^{0.18}\exp(-1.01/T)$
P+NH → H+PN	$0.93\times10^{-10}(T/300)^{0.18}\exp(-0.24/T)$
N+PH → P+NH	$5.62\times10^{-13}(T/300)^{0.63}$
P+NH → N+PH	$1.93\times10^{-13}(T/300)^{1.63}\exp(-3298/T)$
H+PN → N+PH	$2.63\times10^{-13}(T/300)^{2.25}\exp(-25333/T)$
H+PN → P+NH	$6.52\times10^{-13}(T/300)^{1.91}\exp(-23525/T)$

4.4 CPN system

4.4.1 Potential energy surface and reaction mechanisms

Given that the reactants C(^{3}P) and PN($^1\Sigma^+$) predominantly exist in their electronic ground states, only triplet electronic states of the CPN system were considered in this section. The C_s point group symmetry of the system was taken into account, and the lowest electronic state of each irreducible representation ($^3A'$ and $^3A''$) was computed. To explore the possible reaction pathways of the CPN system, the $^3A'$ and $^3A''$ potential energy surfaces (PESs) were investigated, leading to the identification of four key minima and four transition states. Table 11 summarizes their geometries and energies, while Figure 20 displays the overall reaction diagram. The gas-phase reactions examined in this section were:

$$\mathrm{C}(^3\mathrm{P}) + \mathrm{PN}(^1\Sigma^+) \rightarrow \mathrm{P}(^4\mathrm{S}) + \mathrm{CN}(^2\Sigma^+) \tag{4.1}$$

$$\mathrm{C}(^3\mathrm{P}) + \mathrm{PN}(^1\Sigma^+) \rightarrow \mathrm{P}(^4\mathrm{S}) + \mathrm{CN}(^2\Pi) \tag{4.2}$$

$$\mathrm{C}(^3\mathrm{P}) + \mathrm{PN}(^1\Sigma^+) \rightarrow \mathrm{N}(^4\mathrm{S}) + \mathrm{CP}(^2\Sigma^+) \tag{4.3}$$

$$\mathrm{N}(^4\mathrm{S}) + \mathrm{CP}(^2\Sigma^+) \rightarrow \mathrm{P}(^4\mathrm{S}) + \mathrm{CN}(^2\Sigma^+) \tag{4.4}$$

Among the possible products formed from the C+PN reaction, only the P+CN channel is thermodynamically favourable (see Figure 20). It is worth noting that the generation of the CN radical in its excited electronic state, CN($^2\Pi$), is also energetically favorable. The cyano radical has been extensively detected in various astrophysical environments (MCKELLAR, 1940; FRAY et al., 2005; HAN et al., 2015; PARON et al., 2021), suggesting its frequent participation in high-energy astrochemical processes. In fact, based on the processes considered in this section, CN is not expected to be depleted through collisions with atomic phosphorus, as such interactions do not yield exoergic products.

The results show that CP, previously detected in space (GUÉLIN et al., 1990), can be efficiently destroyed by neutral nitrogen atoms through the highly exoergic N+CP → P+CN reaction. Another exoergic pathway, N+CP → C+PN ($\Delta E = -83$ kJ mol^{-1}, where ΔE is the electronic energy including ZPE), supports the conclusion of Chantzos et al. (2020) that this reaction may significantly contribute to PN formation. However, while Chantzos et al. (2020) suggest P+CN → C+PN as a key PN formation route in early diffuse and translucent clouds, the results obtained here indicate that this reaction is strongly endoergic and thus unlikely to proceed in such cold environments.

Figure 20 – Potential energy diagram for the $^3A'$ (red) and $^3A''$ (black) electronic states of the CPN system.

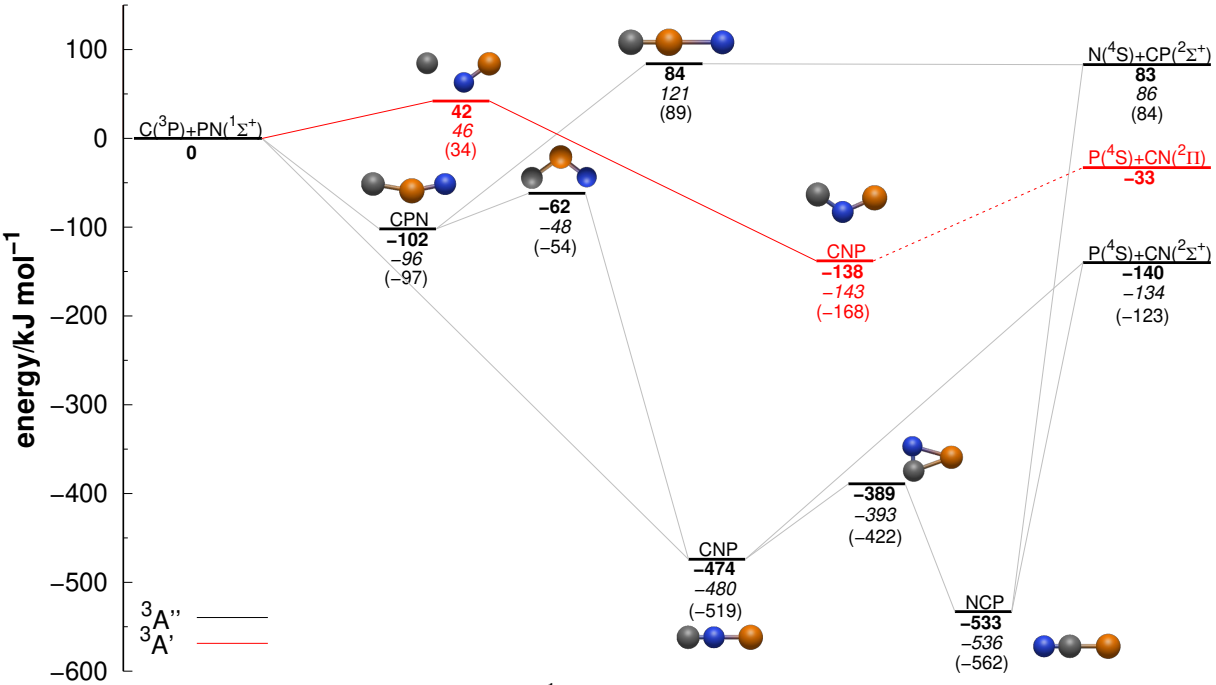

Caption: Energies are given in kJ mol^{-1} relative to the C+PN limit and are ZPE corrected. The MRCI-F12 energies are given in boldface, CCSD(T)-F12 results are given in italics and M06-2X ones are given under parenthesis. Atoms are coloured as: carbon (grey); phosphorus (orange); nitrogen (blue).

Chantzos et al. (2020) incorporated the N+CP → C+PN and P+CN → C+PN reactions into their phosphorus chemical network, based on the model by Agúndez, Cernicharo and Guélin (2007), which adopted the same rate coefficient as the nitrogen analogue reaction, N+CN → C+N_2. A value of $k = 3 \times 10^{-10}$ cm^3 s^{-1} was recommended for 300–2500 K, although low-temperature measurements show variations across four orders of magnitude (BAULCH et al., 1992). Despite its frequent use, the N+CN reaction is highly exothermic ($\Delta E = -205$ kJ mol^{-1}) and has a reaction profile (MOSKALEVA; LIN, 2001) that differs significantly from those of the P-bearing analogues studied in this work. Therefore, employing this nitrogen analogue likely misrepresents the true chemistry of P-bearing species in cold interstellar environments.

Starting from the C+PN reactants, both P+CN and N+CP ground-state products can be accessed adiabatically only on the $^3A''$ surface, whereas the CN radical in its excited state can form on the $^3A'$ surface. Although the formation of CN($^2\Pi$) is exoergic, it requires overcoming a 42 kJ mol^{-1} barrier, making it unlikely under low-temperature ISM conditions.

Table 11 – Properties of the asymptotic limits and stationary points of $^3A'$ and $^3A''$ PESs[a].

	R_{PN}	R_{PC}	R_{CN}	E[b]
$^3A'$				
CNP	1.59	2.59	1.40	-138
$TS_{C+PN\rightarrow CNP}$	1.54	3.05	2.04	42
$^3A''$				
CPN	1.54	1.77	3.26	-102
CNP	1.70	2.89	1.19	-474
NCP	2.95	1.77	1.18	-533
$TS_{CPN\rightarrow N+CP}$	2.50	1.59	4.10	84
$TS_{CPN\rightarrow CNP}$	1.63	1.75	2.72	-62
$TS_{CNP\rightarrow NCP}$	2.01	1.99	1.21	-389
Asymptotic limits				
$C(^3P) + PN(^1\Sigma^+)$	1.51	-	-	0
$N(^4S) + CP(^2\Sigma^+)$	-	1.58	-	83
$P(^4S) + CN(^2\Pi)$	-	-	1.25	-33
$P(^4S) + CN(^2\Sigma^+)$	-	-	1.18	-140

[a] Interatomic distances are in given in Å and energies in kJ mol^{-1} relative to the C+PN limit.
[b] At the MRCI-F12/AV(T+d)Z level including ZPE correction calculated at the CASSCF/AV(T+d)Z level.

Figure 20 shows good agreement between CCSD(T)-F12 and MRCI-F12 relative energies, with deviations generally below 6 kJ mol^{-1}, except for $TS_{CPN\rightarrow CNP}$ and $TS_{CPN\rightarrow N+CP}$, likely due to strong multireference character (T_1 = 0.056 and 0.080, respectively). M06-2X results align qualitatively with MRCI-F12, with most deviations within 10%, although the largest deviation (22%, or 30 kJ mol^{-1}) was observed for the CNP ($^3A'$) minimum. The following discussion is thus based on the more reliable MRCI-F12/AV*T*Z+d//CAS/AV*T*Z+d+d+ZPE(CAS/AV*T*Z+d) results.

Regarding PN destruction, carbon atom attack on the P-end of PN leads barrierlessly to a bent CPN intermediate on the $^3A''$ surface. This species can isomerize to CNP or dissociate to $N(^4S)$+$CP(^2\Sigma^+)$, but the latter path requires overcoming an 84 kJ mol^{-1} barrier and leads to products 83 kJ mol^{-1} above the reactants, making it unlikely under cold ISM conditions. Isomerization from CPN to CNP proceeds via a TS 40 kJ mol^{-1} above CPN, while the CNP → NCP conversion involves another submerged TS. Both CNP and NCP can dissociate to $P(^4S)$+$CN(^2\Sigma^+)$ without an exit barrier, making this a feasible PN destruction route. Alternatively, this same product channel can be accessed more directly via carbon attack on the N-end of PN, forming CNP and dissociating barrierlessly.

For N+CP collisions, two exoergic pathways are available: C+PN and P+CN. The P+CN channel proceeds through the formation of the global minimum (NCP) in a barrierless way. The C+PN channel involves a small 1 kJ mol^{-1} entrance barrier, within the uncertainty margin of the calculations, and can also occur without activation via the NCP → CNP → C+PN sequence.

4.4.2 Reaction rates coefficients

Among the reactions examined, only P+CN → C+PN and N+CP → C+PN have rate constants listed in the UMIST database (MILLAR et al., 2024), both with a value of $k = 3 \times 10^{-10}\,\mathrm{cm^3\,s^{-1}}$, while neither is currently found in KIDA (WAKELAM et al., 2024). However, the results obtained here show that the P+CN reaction is endoergic, and the UMIST value (based on the analogous N+CN → N_2+C reaction) may mislead astrochemical models. Unlike N_2, PN is less thermodynamically stable, and the results reveal distinct reaction mechanisms and energy landscapes. The P+CN process is significantly endoergic and should not exhibit such a high, temperature-independent rate coefficient. For N+CP → C+PN, although the reaction is exoergic, a small entrance barrier absent in the nitrogen analogue was predicted (MOSKALEVA; LIN, 2001), suggesting a lower rate constant than currently listed.

Accurate rate coefficients for reactions 4.1, 4.3, 4.4 and their reverse processes using MRCI-F12/AV*T*Z+d//CAS/AV*T*Z+d + ZPE(CAS/AV*T*Z+d) energies and the MESS code were computed. These were fitted to the modified Arrhenius equation, and the resulting curves for the exoergic reactions are shown in Figure 21. As expected for barrierless exoergic processes, the rates show minimal temperature dependence. The results also indicate that, for typical ISM conditions, the branching ratio of N+CP strongly favors P+CN over C+PN by about two orders of magnitude, despite only the latter being included in UMIST.

The C+PN → P+CN reaction (Equation 4.1) may significantly impact PN abundance, as it is the only neutral-neutral pathway for PN destruction. Its calculated rate coefficients are nearly constant across a wide temperature range, with an average of $k = 1.35 \times 10^{-10}\,\mathrm{cm^3\,s^{-1}}$. At low temperatures (<200 K), however, the rates increase, which can be attributed to the population of the lowest fine-structure level of the ^{3}P carbon atom, which is the one that correlates to the ground state PES of the CPN system. As the population shifts to lower-J states with higher statistical weights at lower temperatures, the rate coefficients increase accordingly.

Previous work by Douglas, Gobrecht and Plane (2022) also addressed the C+PN and reverse reactions, estimating the rate coefficient for the forward reaction using long-range transition state theory (GEORGIEVSKII; KLIPPENSTEIN, 2005) and applying detailed balance for the reverse. Although their model considers only the CNP intermediate and neglects other paths, their results (shown as dashed lines in Figures 21 and 22) agree well with the results obtained here.

Figure 21 – Rate coefficients as a function of temperature obtained for the exoergic reactions (CPN).

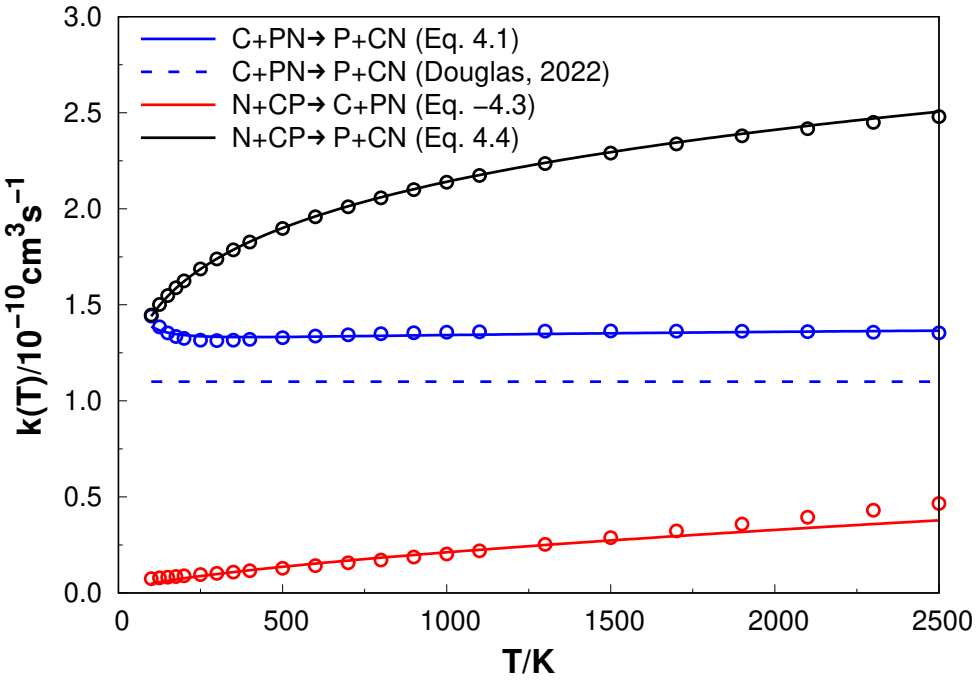

Caption: The points refer to the calculated values at fixed temperatures and the curves correspond to a fit to the results obtained here using the modified Arrhenius formula. The rate coefficient proposed by Douglas, Gobrecht and Plane (2022) for the C+PN → P+CN reaction is shown as a dashed line for comparison.

For the endoergic reactions (Equations −4.1, 4.3, and −4.4), Figure 22 displays Arrhenius plots illustrating their strong temperature dependence. Notably, the UMIST rate constant for P+CN → C+PN is vastly overestimated; the results show that this reaction reaches only $k = 1.0\times10^{-17}$ cm^3 s^{-1} at 1000 K (seven orders of magnitude lower than the UMIST value (BAULCH et al., 1992; AGÚNDEZ; CERNICHARO; GUÉLIN, 2007)). While high-temperature conditions may be relevant to exoplanetary atmospheres (AL-REFAIE et al., 2022; FLEURY et al., 2025), the focus in this section of the work lies on the colder regions of the ISM, where these endoergic processes are unlikely to contribute significantly to the chemistry of P-bearing species. Table 12 gathers the rate coefficients as a function of temperature for all reactions studied in this part of the work using a modified Arrhenius equation fit.

Table 12 – Rate coefficients as a function of temperature for all reactions studied in this section of the work using a modified Arrhenius equation fit (CPN).

	k(T) / cm^3 s^{-1}
C+PN → P+CN	$1.29\times10^{-10}(T/300)^{0.025}\exp(10/T)$
P+CN → C+PN	$2.15\times10^{-10}(T/300)^{0.118}\exp(-17000/T)$
N+CP → P+CN	$1.74\times10^{-10}(T/300)^{0.172}$
N+CP → C+PN	$9.86\times10^{-12}(T/300)^{0.634}$
C+PN → N+CP	$1.09\times10^{-11}(T/300)^{1.18}\exp(-9669/T)$
P+CN → N+CP	$6.01\times10^{-10}(T/300)^{0.014}\exp(-27394/T)$

Figure 22 – Rate coefficients as a function of inverse temperature obtained for the endoergic reactions (CPN).

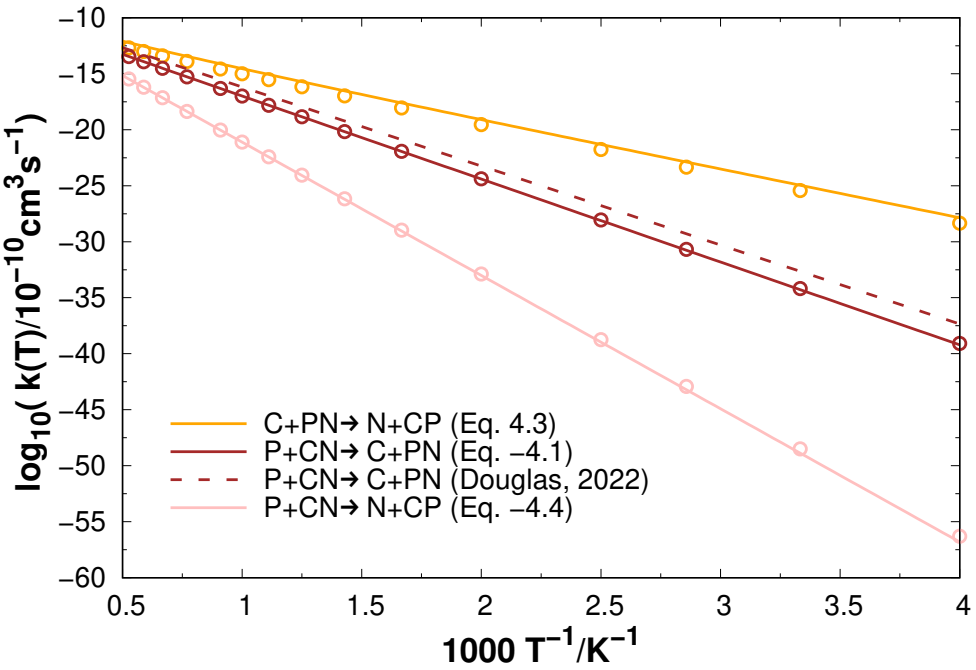

Caption: The points refer to the calculated values at fixed temperatures and the curves correspond to a fit to the results obtained here using the modified Arrhenius formula. The rate coefficient proposed by Douglas, Gobrecht and Plane (2022) for the C+PN → P+CN reaction is shown as a dashed line for comparison.

4.5 Astrochemical modeling

Assessing the behaviour of computed reactions in astrochemical models is crucial for understanding their influence on the abundances of phosphorus-bearing species (PBSs). In the most recent article published by our group (SILVA et al., 2025), focused on the astrochemistry of phosphorus, and whose results are part of the present thesis, developed in collaboration with several researchers from Brazil, Spain, Portugal, and China, two collaborators from Spain, Edgar Mendoza and Miguel Carvajal (both from the Universidad de Huelva) developed chemical models capable of predicting the abundances of PBSs, especifically PO, PN, and PH, under varying astrophysical conditions (diffuse and translucent cloud model; and dense cloud conditions).

Based on these models, all the reactions studied and presented throughout this thesis could be quantitatively analyzed. The primary goal of the models was to investigate the time evolution of all new reactions and to estimate the resulting abundances of PO, PN, and PH under physical conditions simulating the transition from diffuse to denser interstellar cloud environments. For details on the methodology used to develop the models, see Ref. Silva et al. (2025).

The gas-phase chemical network used in the models was based on the comprehensive *kida.uva.2014* database (WAKELAM et al., 2015), which compiles an extensive set of reaction pathways and kinetic parameters. Although the updated *kida.uva.2024* version includes new species and reaction channels, it retains the original treatment of phosphorus chemistry (WAKE-

LAM et al., 2024). To overcome this limitation, the chemical network was extended to incorporate revised reaction pathways involving PBSs. This refinement enabled more accurate predictions of the abundances of key astrochemical molecules such as PO and PN, whose formation mechanisms under extreme astrophysical conditions remain poorly understood. Among the reactions already present in the KIDA database and examined in this work, the following had their rate coefficients updated based on the results obtained here: $N(^4S) + PH(^3\Sigma^-) \rightarrow H(^2S) + PN(^1\Sigma^+)$, $N(^4S) + PN(^1\Sigma^+) \rightarrow N_2(^1\Sigma^+) + P(^4S)$, and $P(^4S) + O_2(^3\Sigma^-) \rightarrow O(^3P) + PO(^2\Pi)$. Table 13 presents a list of all the chemical reactions involving PBSs that were included in the models. As shown in Table 13, all the processes investigated throughout this PhD work were incorporated into the models. The main results are going to be addressed in the next subsections.

Table 13 – List of chemical reactions involving phosphorus-bearing species explored in the models (SILVA et al., 2025).

Reaction	Rate coefficients			Remark	Method
	α (cm^3s^{-1})	β	γ (K)		
PN + C ⟶ CN + P	1.29×10^{-10}	0.025	−10.0	this work	MESS[a]
P + CN ⟶ PN + C	2.15×10^{-10}	0.118	17000	this work	MESS[a]
N + CP ⟶ P + CN	1.74×10^{-10}	0.172	0	this work	MESS[a]
N + CP ⟶ C + PN	9.86×10^{-12}	0.634	0	this work	MESS[a]
C + PN ⟶ N + CP	1.09×10^{-11}	1.18	9669	this work	MESS[a]
P + CN ⟶ N + CP	6.01×10^{-10}	0.014	27394	this work	MESS[a]
N + PN ⟶ P + N_2	1.09×10^{-11}	1.02	7919	this work	MESS[a]
N + PH ⟶ P + NH	5.62×10^{-13}	0.63	0	this work	MESS[a]
P + NH ⟶ N + PH	1.93×10^{-13}	1.63	3298	this work	MESS[a]
P + NH ⟶ PN + H	9.3×10^{-11}	0.18	0.24	this work	VRC-TST[b]
PN + H ⟶ P + NH	6.52×10^{-13}	1.91	23525	this work	MESS[a]
PH + N ⟶ PN + H	8.8×10^{-11}	0.18	1.01	this work	VRC-TST[b]
PN + H ⟶ PH + N	2.63×10^{-13}	2.25	25333	this work	MESS[a]
P + O_2 ⟶ PO + O	1.44×10^{-12}	1.66	704	this work	MESS[a]
PO + O ⟶ P + O_2	1.8×10^{-13}	0.79	10054	Douglas, Gobrecht and Plane (2022)	Detailed balance[c]
P + OH ⟶ PO + H	2.28×10^{-10}	0.16	0.37	Concepción et al. (2021)	MESS[a]
PO + H ⟶ P + OH	4.2×10^{-13}	0.82	16791	Douglas, Gobrecht and Plane (2022)	Detailed balance[c]
PH + OH ⟶ P + H_2O	1.0×10^{-10}	0.167	0	Douglas, Gobrecht and Plane (2022)	Collision capture rate[c]
P + H_2O ⟶ PH + OH	9.0×10^{-10}	0	24319	Douglas, Gobrecht and Plane (2022)	Detailed balance[c]
PH + O ⟶ PO + H	2.0×10^{-10}	0	0	Douglas, Gobrecht and Plane (2022)	Collision capture rate[c]
PO + H ⟶ PH + O	2.8×10^{-10}	0.26	34462	Douglas, Gobrecht and Plane (2022)	Detailed balance[c]
PO + NH ⟶ PN + OH	1.0×10^{-10}	0	0	Douglas, Gobrecht and Plane (2022)	Collision capture rate[c]
PN + OH ⟶ PO + NH	2.6×10^{-10}	0	13002	Douglas, Gobrecht and Plane (2022)	Detailed balance[c]
PO + Si ⟶ P + SiO	2.1×10^{-10}	0.10	0	Douglas, Gobrecht and Plane (2022)	MESMER[d]
P + H_2 ⟶ PH + H	6.7×10^{-10}	0	17349	Douglas, Gobrecht and Plane (2022)	Transition state theory[c]
PH + H ⟶ P + H_2	6.7×10^{-11}	0	346	Douglas, Gobrecht and Plane (2022)	Detailed balance[c]
P + NO ⟶ PN + O	7.1×10^{-11}	0	6427	Douglas, Gobrecht and Plane (2022)	MESMER[d]
PN + O ⟶ P + NO	1.0×10^{-10}	0	3158	Douglas, Gobrecht and Plane (2022)	MESMER[d]
PN + O ⟶ PO + N	2.7×10^{-10}	0	744	Douglas, Gobrecht and Plane (2022)	MESMER[d]
PO + N ⟶ P + NO	2.55×10^{-12}	0	0	Millar, Bennett and Herbst (1987)	Estimation
PO + N ⟶ PN + O	1.53×10^{-11}	−0.31	0	Silva et al. (2025)	MESS[a]

[a] Calculated using the master equation system solver package.
[b] Variable reaction coordinate transition state theory.
[c] See the associated reference for further details.
[d] Calculated using the Master Equation Solver for Multi-Energy well Reactions program. See the associated reference for further details.

4.5.1 [PO]/[PN] ratios

Figure 23 shows the calculated ratios of [PO]/[PN] as a function of time in the diffuse/translucent cloud model. In the caption of this Figure, ζ_{CR} stands for cosmic ray ionization rate and ζ_X stands for X-ray ionization rates. By analyzing the abundances of PO and PN under varying cosmic-ray and X-ray ionization rates, it can be identified corresponding variations in their abundance ratios. In the early stages of the simulation ($t < 10^2$ yr), the influence of ionization on the ratio is relatively minor. However, as the system evolves, the differences between the models become increasingly evident. In the later stages ($t > 10^5$ yr), the [PO]/[PN] ratios stabilize within a range of approximately 15 to 60, corresponding to cosmic-ray ionization rates increasing from 1.3×10^{-17} s^{-1} to 1.3×10^{-16} s^{-1}. These findings suggest that elevated ionization rates and other energetic processes can significantly impact PO chemistry, thereby altering the [PO]/[PN] abundance ratio.

Figure 23 – Ratios of [PO]/[PN] as a function of time in the diffuse/translucent cloud model.

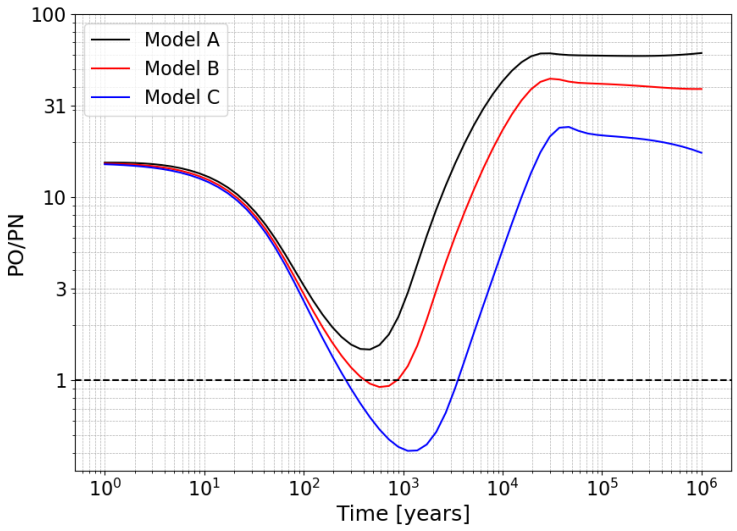

Caption: A) ζ_{CR}=1.3 × 10^{-16} s^{-1} and ζ_X=1 × 10^{-17} s^{-1}; B) ζ_{CR}=6.3 × 10^{-17} s^{-1} and ζ_X=5 × 10^{-18} s^{-1}; and C) ζ_{CR}=1.3 × 10^{-17} s^{-1} and ζ_X=1 × 10^{-18} s^{-1}. The dashed line signifies the threshold at which [PO]/[PN] equals 1.

4.5.2 Abundances of phosphorus-bearing species as a function of time

The time-dependent abundances of PBSs were computed under the physical conditions for diffuse and translucent clouds, where the gas temperature and density were kept constant. In order to evaluate the effect of ionisation, Model B (see Figure 23), characterised by intermediate ionisation rates was selected as a representative case. The results are shown in Figures 24 and 25, which displays the abundance evolution of atomic phosphorus P, PO, PN, and PH over a timescale of 10^6 years.

Analysing Figure 24, it can be seen that elemental phosphorus remains the most abundant PBSs throughout the simulation and PO consistently exhibits higher abundances than PN. The abundance of PH is represented by a dashed line in Figure 24. Although species like PH are transient and highly reactive, posing challenges for observational detection, they play a central role in phosphorus chemistry. Notably, PH contributes to the formation of both PO and PN via neutral-neutral reactions: PH + O → PO + H and PH + N → PN + H (see Table 13).

Figure 24 – Evolution of the abundances of P, PO, PN and the radical PH (dashed line) in the diffuse/translucent cloud model.

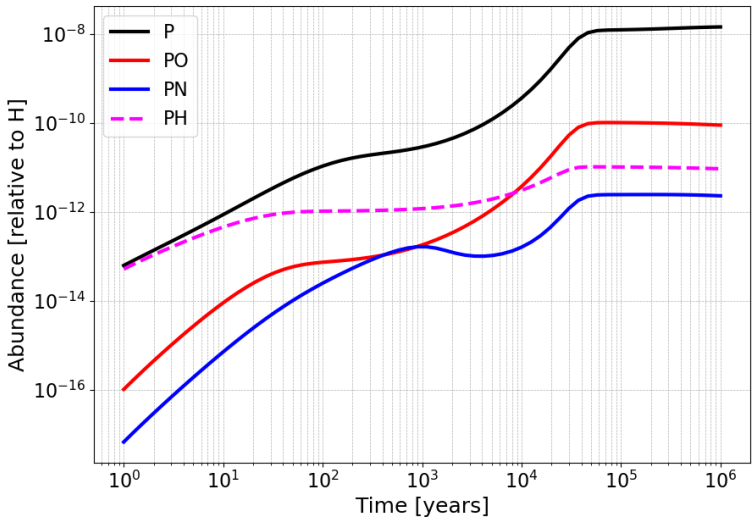

To further explore phosphorus chemistry, a second model simulating dense cloud conditions was constructed. In this case, the final abundances obtained from the diffuse/translucent model served as the initial input. As dense molecular clouds provide strong shielding against UV and X-ray radiation, an extinction value of $A_V = 10$ mag was adopted and applied the lowest ionisation rates tested in this study, as defined in Model C ($\zeta_{CR} = 1.3 \times 10^{-17}$ s^{-1} and $\zeta_X = 1 \times 10^{-18}$ s^{-1}). With this context in mind, the objectives of the dense cloud model was to investigate the temporal evolution of PBSs, identify dominant chemical pathways, assess steady-state conditions, and examine the dynamical balance of the chemical network over an extended period from 10^6 to 10^8 years. The abundance results are presented in Figure 25. The curves reveal that PO and PN follow similar trends, with abundances fluctuating between $\sim 5 \times 10^{-11}$ and 5×10^{-8}. Aside from the initial stages, PO maintains higher abundances than PN throughout the simulation. At the final stage, PO stabilizes around 3.3×10^{-10}, while PN, alongside PH, settles near 1.3×10^{-10}.

Figure 25 – Evolution of the abundances of P, PO, PN and the radical PH (dashed line) in the dense cloud model.

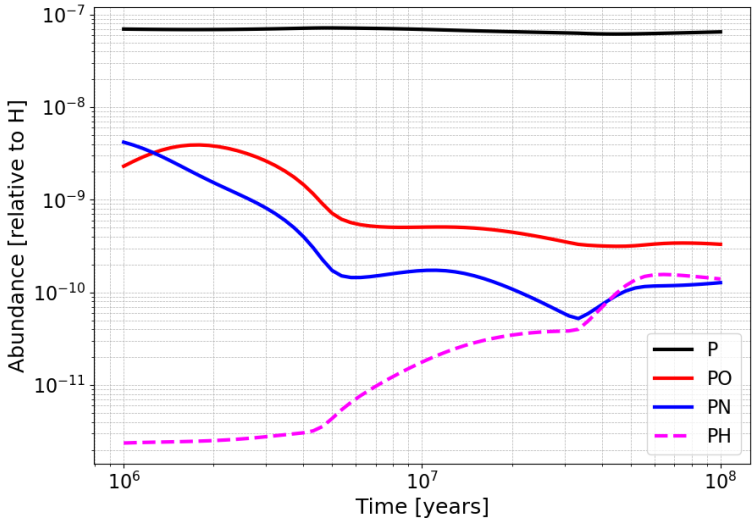

4.5.3 Key reactions that influence the abundances of PN and PO

The main chemical pathways governing the formation and destruction of PN and PO, are presented in Figures 26 and Figures 27. For PN (Figure 26), the dominant formation route is the PO + N reaction, which initially accounts for nearly all PN production but gradually declines to about 50% over time. Meanwhile, the PH+N reaction (studied in this work), though initially minor, gains relevance and reaches a comparable contribution in later stages. Regarding destruction, PN is primarily depleted through reactions with H^+ and atomic C, with the latter being one of the key mechanisms investigated in this thesis. PH is primarily formed via dissociative recombination of molecular ions with electrons, as in the reactions $HPO^+ + e^- \rightarrow O + PH$ and $HPN^+ + e^- \rightarrow N + PH$. Its main destruction pathways, in turn, contribute to the synthesis of PO and PN.

For PO (Figure 27), the main formation pathway is the P + OH reaction, initially responsible for about 88% of PO production. Over time, however, its contribution diminishes, while the PH + O reaction becomes increasingly important, with both curves intersecting at around $t = 6 \times 10^6$ yr. A minor formation route via $HPO^+ + e^-$ is also present but remains less significant. In terms of destruction, PO is primarily consumed via reactions with N and H^+. Initially, PO + N dominates, but as time progresses, PO + H^+ becomes the main depletion pathway. Overall, the results suggest a dynamic balance between formation and destruction processes. The interplay between P + OH and PH + O for PO formation, and between PO + N and PO + H^+ for its destruction, regulates the steady-state abundance of PO, thereby influencing PN chemistry as well.

Our chemical modeling of diffuse and translucent clouds consistently show higher PO abundances than PN. Both species were found to be sensitive to environmental factors such as visual extinction and ionisation rates. In particular, the [PO]/[PN] ratio increases with the cosmic

ray ionisation rate, while lower ionisation conditions can drive the ratio below 1. This variability highlights the critical role of ionisation in shaping phosphorus chemistry in the ISM. In a denser cloud model, using a standard ionisation rate ($\zeta_{CR} = 1.3 \times 10^{-17}$ s^{-1}), the predicted abundances of PO and PN reached $\sim 3 \times 10^{-10}$ and 1×10^{-10}, respectively. A key result of this model is the identification of PO + N as the main formation pathway for PN, consistent with the finding that PO destruction is largely driven by its reaction with atomic nitrogen, forming PN (see Figure 26). Ultimately, it can be concluded that gas-phase reactions are fundamental to explain the observed PO and PN abundances across different environments.

It is important to highlight that the models above simulate only cold clouds. As discussed throughout this chapter, the P+O_2 (section 4.1.3) and N+PN (section 4.2.2) reactions, due to their activation barriers, are only expected to be relevant in shock regions, where the temperatures are higher. Thus, it is no surprise that these two reactions were not seen as important for abundances of PO and PN in the models of cold clouds presented above.

When considering the individual reactions studied in this work, and considering the physical conditions applied in the models, the N+PH (section 4.3.2) and C+PN (section 4.4.2) reactions demonstrated greater impact when evaluating their influence on the abundance of PN. It is evident from the results that gas-phase neutral-neutral reactions should also be considered and studied for a better understanding of phosphorus astrochemistry and the observed abundances of species containing this element in space.

Figure 26 – Major reactions for PN.

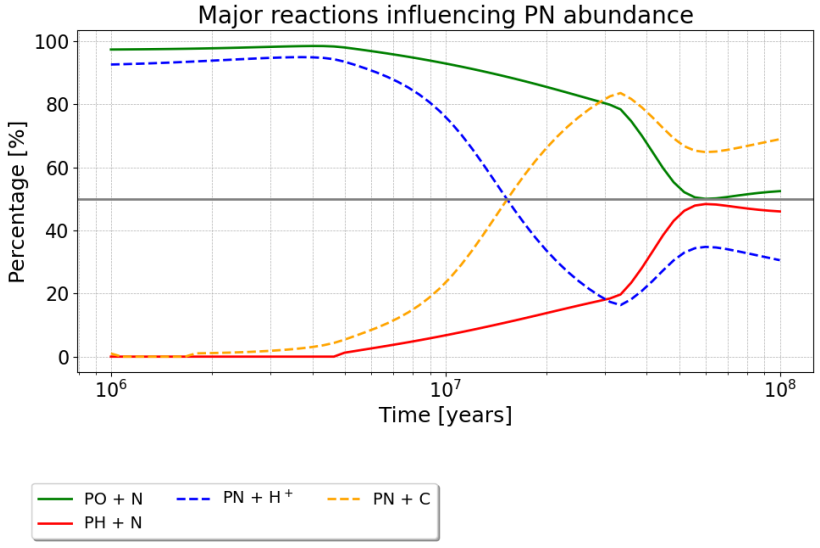

Caption: The contributions of each reaction are represented as percentages over time. Solid and dashed lines differentiate production and destruction mechanisms, respectively. The time is presented on a logarithmic scale to highlight contributions beyond 10^6 years, with a horizontal gray line at 50% for assessing balance throughout the duration of the long-term trends in the chemical network.

Figure 27 – Major reactions for PO.

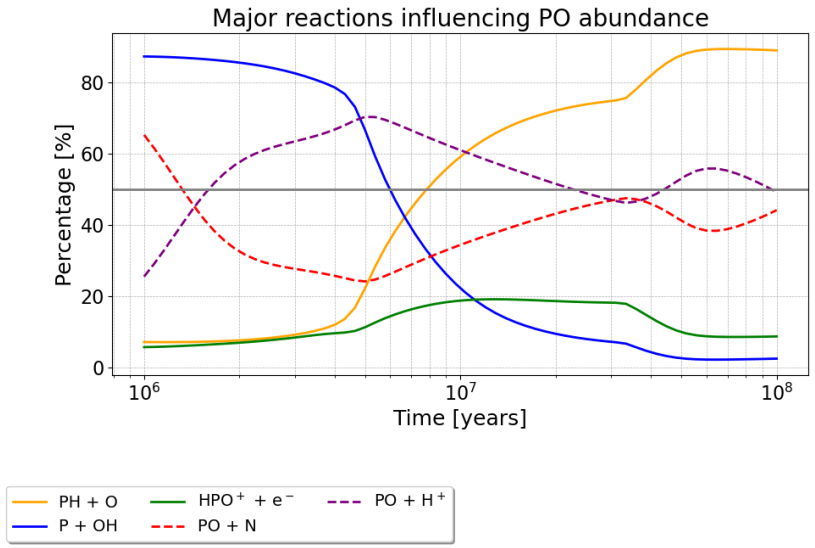

Caption: The contributions of each reaction are represented as percentages over time. Solid and dashed lines differentiate production and destruction mechanisms, respectively. The time is presented on a logarithmic scale to highlight contributions beyond 10^6 years, with a horizontal gray line at 50% for assessing balance throughout the duration of the long-term trends in the chemical network.

5 Concluding remarks and future directions

The mechanisms and kinetics of key neutral-neutral gas-phase reactions relevant to phosphorus astrochemistry were successfully investigated from a theoretical perspective. High-level electronic structure calculations were performed to elucidate the reaction pathways and to compute temperature-dependent rate constants using various formulations of Transition State Theory. As a result, new theoretical data were generated that can be incorporated into widely used astrochemical databases. Furthermore, astrochemical modeling was employed to assess the individual impact of each studied reaction on the broader phosphorus chemistry in the interstellar medium (ISM).

Considering the $P(^4S) + O_2(^3\Sigma_g^-) \rightarrow O(^3P) + PO(^2\Pi)$ reaction, high-accuracy theoretical calculations employing the multireference configuration interaction method have been performed in order to better understand the mechanism and kinetics of the formation of PO molecules in the interstellar medium (ISM) via this reaction. CCSD(T)-F12 and DFT energies were also computed for comparison. It is shown that the OPO system possesses a very high multiconfigurational character, making both DFT and CCSD methods not reliable for the study of its potential energy surfaces and rate constants. An exploration of the potential energy surface reveals that PO formation can occur in both the doublet and quartet states. The reactivity is dominated by an entrance barrier on both states, followed by formation of a POO structure which then decomposes to O+PO. The rate coefficients and its temperature dependence were calculated with the master equation approach based on transition state theory with the MESS software. This has shown the relevance of the quartet state for temperatures higher than 700K. Our results were also used to discuss the experimentally available ones, and analyse the behavior at the high temperatures achieved in the upper atmosphere and in circumstellar envelopes.

For the $N(^4S) + PN(^1\Sigma^+) \rightarrow N_2(^1\Sigma_g^+) + P(^4S)$ reaction, high-accuracy calculations using the explicitly correlated multireference configuration interaction method (MRCI+Q) were performed aiming to better elucidade the kinetics and relevance of this reaction in the destruction of phosphorus nitride. CCSD(T)-F12 and DFT energies were calculated for comparison. It was found that the NPN system possesses a considerable multireference character, especially for the two steps mechanism towards $N_2(^1\Sigma_g^+) + P(^4S)$. The latter cannot be properly described using DFT and CCSD(T) methodologies. Nevertheless, the direct mechanism can be described by all methodologies. The high energy of the NPN $\rightarrow N_2 + P$ barrier makes the two steps mechanism closed. In order to compare standard transition state theory rate coefficients with variational ones, apart from the MRCI+Q results, DFT-CVT-SCT and CCSD(T)-CVT-SCT rate coefficients were also computed, showing their respective temperature dependence. The MRCI+Q-TST coefficients were compared with CCSD(T) ones. At high temperatures (above 4000K), both converged to similar results, that is, even though the title reaction possesses an activation energy barrier, their

thermal rate coefficients approach 10^{-10}cm^3 s^{-1} at high temperatures, and thus may be important to astrochemical models of shocks and other high temperature regions. Given the fact that it is becoming more clear that atomic nitrogen plays an important role in such environments, these results might considerably change our knowledge regarding the chemistry of phosphorus in shock and high temperature regions, since this reaction was assumed to not occur.

Regarding P(^4S) + NH($^3\Sigma^-$) $\rightarrow$ H(^2S) + PN($^1\Sigma^+$) and N(^{4}S) + PH($^3\Sigma^-$) $\rightarrow$ H(^2S) + PN($^1\Sigma^+$) reactions, MRCI-F12/AVTZ+d//CAS/AVTZ+d calculations were performed in order to study the potential energy surfaces of two reactions that lead to the important phosphorus bearing molecule PN. Their rate coefficients were also calculated, using direct variable reaction coordinate transition state theory (VRC-TST), leading to the conclusion that both reactions proceed without an activation barrier being relevant for PN formation in the interstellar medium. The P+NH reacion is not incorporated in the databases and, therefore, should be included for better modeling the abundances of PN. Regarding the kinetics, collision N(^{4}S) + PH($^3\Sigma^-$) possesses a rate coefficient that can be expressed as $\alpha = 0.88 \times 10^{-10}$cm^3 s^{-1}, $\beta = -0.18$ and $\gamma = 1.01$ K, while P(^4S) + NH($^3\Sigma^-$) the rate coefficient is given by $\alpha = 0.93 \times 10^{-10}$cm^3 s^{-1}, $\beta = -0.18$ and $\gamma = 0.24$ K. Therefore, both reactions can be similarly fast. The other barrierless channel (N+PH $\rightarrow$ P+NH) possesses a much lower rate constant, and can be considered negligible for the total branching ratio. The results for the destruction of PN by hydrogens atoms support previous assumptions that this can only happen in cold environments of the ISM through ion-molecule reactions.

In the CPN system, several reaction pathways for the destruction of PN through collisions with atomic carbon were identified, leading to the formation of P(^{4}S) + CN($^2\Sigma^+$) without an activation barrier. This was found to be the only accessible product channel for the C(^{3}P) + PN($^1\Sigma^+$) reaction, regardless of the collision energy involved. Regarding kinetics, for the PN-destruction reaction C(^{3}P) + PN($^1\Sigma^+$) $\rightarrow$ P(^{4}S) + CN($^2\Sigma^+$), the obtained parameters were $\alpha = 1.29 \times 10^{-10}$cm^3 s^{-1}, $\beta = 0.025$, and $\gamma = -10.0$ K, highlighting its role as a relevant pathway that should be included in astrochemical models of phosphorus chemistry. In contrast, formation routes of CP from N(^{4}S) + PN were found to be considerably endoergic, indicating that CP formation via this mechanism is only viable at very high temperatures. However, CP destruction by collisions with nitrogen atoms is expected to occur efficiently even under low-temperature conditions. For the N(^{4}S) + CP($^2\Sigma^+$) $\rightarrow$ P(^{4}S) + CN($^2\Sigma^+$) reaction, the fitted rate coefficient possesses $\alpha = 1.74$cm^3 s^{-1}, $\beta = 0.172$, and $\gamma = 0$. This value is significantly higher than that obtained for the competing channel N(^{4}S) + CP($^2\Sigma^+$) $\rightarrow$ C(^{3}P) + PN($^1\Sigma^+$), with $\alpha = 9.86$cm^3 s^{-1}, $\beta = 0.634$, and $\gamma = 0$. Furthermore, the results demonstrated that the energy landscape of the CPN system is markedly different from that of the NCN analogue, indicating that the use of nitrogen-based analogies is not appropriate for accurately describing the reaction dynamics within the CPN system.

Chemical modeling has demonstrated that ionization levels play a crucial role in shaping phosphorus chemistry in the ISM. Higher ionization promotes the formation of PO and increases the [PO]/[PN] ratio. In diffuse clouds, PO becomes the dominant PBSs under strong ionizing conditions, while PN may slightly prevail when ionization is weaker. In contrast, PO consistently remains more abundant in dense clouds. Its formation primarily proceeds through the P+OH and O+PH reactions, whereas its destruction is mainly driven by interactions with atomic nitrogen and H^+. For PN, the dominant formation route involves the N+PO reaction, with N+PH also contributing significantly. PN is primarily depleted through reactions with H^+ and atomic carbon. A key outcome of this study is the identification of two neutral–neutral reactions as particularly important for PN destruction and formation in interstellar environments: $N(^4S) + PH(^3\Sigma^-) \rightarrow H(^2S) + PN(^1\Sigma^+)$ (formation) and $C(^3P) + PN(^1\Sigma^+) \rightarrow P(^4S) + CN(^2\Sigma^+)$ (destruction). The rate coefficients for these reactions, determined in this work, highlight their relevance to the broader modeling of phosphorus chemistry. Most importantly, the overall findings of the models emphasize the importance of incorporating gas-phase neutral–neutral reactions into astrochemical models. Their role is especially significant in the chemistry of PBSs, where accounting for both formation and destruction mechanisms, particularly those involving PO and PN, is essential for accurately reproducing the observed interstellar abundances.

As part of both ongoing and future research efforts, the investigation of the $C(^3P) + PH(^3\Sigma^-) \rightarrow CP(^2\Sigma^+) + H(^2S)$ and $C(^3P) + PO(^2\Pi) \rightarrow CO(^1\Sigma^+) + P(^4S)$ reactions, initiated during my time at Qufu Normal University (曲阜师范大学), China, is nearing completion, and we expect to publish the corresponding results in the near future.

6 Final Acknowledgements

The author would like to express sincere gratitude to all the collaborating researchers (Carlos M. R. Rocha, André C. Souza, Ahren W. Jasper, René F. K. Spada, Bertrand Lefloch, Mateus X. Silva, Edgar Mendoza, Fábio S. L. Ferreira, Miguel Carvajal, and António J. C. Varandas) who contributed to the development of this work. The contribution of each of these remarkable researchers was essential to the completion of this thesis.

The author would also like to once again thank the financial support provided by the Coordenação de Aperfeiçoamento de Pessoal de Nível Superior (CAPES) - Finance Code 001, the Centro Federal de Educação Tecnológica de Minas Gerais (CEFET-MG), and its Programa de Pós-Graduação Multicêntrico em Química de Minas Gerais (PPGMQ-MG). Rede Mineira de Química (RQ-MG) is also acknowledged.

Bibliography

ADLER, T. B.; KNIZIA, G.; WERNER, H.-J. A simple and efficient ccsd(t)-f12 approximation. *J. Chem. Phys.*, American Institute of Physics, v. 127, n. 22, p. 221106, 2007. Cited 3 times on pages 41, 63, and 66.

AGÚNDEZ, M. et al. Confirmation of circumstellar phosphine. *Astrophys. J.*, v. 790, p. L27, 2014. Cited on page 27.

AGÚNDEZ, M.; CERNICHARO, J.; GUÉLIN, M. Discovery of phosphaethyne (hcp) in space: Phosphorus chemistry in circumstellar envelopes. *Astrophys. J.*, v. 662, p. L91–L94, 2007. Cited 4 times on pages 27, 30, 91, and 94.

AGÚNDEZ, M. et al. Tentative detection of phosphine in irc+ 10216. *Astronomy & Astrophysics*, EDP Sciences, v. 485, n. 3, p. L33–L36, 2008. Cited on page 27.

AGÚNDEZ, M.; WAKELAM, V. Chemistry of dark clouds: Databases, networks and models. *Chem. Rev.*, v. 113, p. 8710–8737, 2013. Cited 2 times on pages 18 and 31.

AL-REFAIE, A. F. et al. A comparison of chemical models of exoplanet atmospheres enabled by taurex 3.1. *The Astrophysical Journal*, IOP Publishing, v. 932, n. 2, p. 123, 2022. Cited on page 94.

ALLISON, T. C.; TRUHLAR, D. G. Testing the accuracy of practical semiclassical methods: Variational transition state theory with optimized multidimensional tunneling. In: *Modern methods for multidimensional dynamics computations in chemistry*. [S.l.]: World Scientific, 1998. p. 618–712. Cited on page 58.

ALTWEGG, K. et al. Prebiotic chemicals—amino acid and phosphorus—in the coma of comet 67p/churyumov-gerasimenko. *Sci. Adv.*, American Association for the Advancement of Science, v. 2, n. 5, p. e1600285, 2016. Cited 2 times on pages 17 and 25.

ANDREAZZA, C.; ALMEIDA, A. de; BORIN, A. The radiative association of p and o atoms. *Mon. Not. R. Astron. Soc.*, Oxford University Press, v. 457, n. 3, p. 3096–3100, 2016. Cited on page 26.

AOTA, T.; AIKAWA, Y. Phosphorus chemistry in the shocked region l1157 b1. *Astrophys. J.*, v. 761, p. 74, 2012. Cited 2 times on pages 26 and 29.

ARRHENIUS, S. Über die reaktionsgeschwindigkeit bei der inversion von rohrzucker durch säuren. *Zeitschrift für physikalische Chemie*, De Gruyter Oldenbourg, v. 4, n. 1, p. 226–248, 1889. Cited on page 45.

ATKINS, P.; PAULA, J. D. *Físico-Química*. Rio de Janeiro: LTC, 2012. v. 2. Cited 2 times on pages 43 and 44.

ATKINS, P.; PAULA, J. D. *Físico-Química*. Rio de Janeiro: LTC, 2015. v. 1. Cited 2 times on pages 32 and 33.

ATKINS, P. W.; FRIEDMAN, R. S. *Molecular quantum mechanics*. The University of Tokyo Tokyo, Japan: Oxford university press, 2005. Cited 10 times on pages 31, 32, 33, 34, 35, 36, 37, 38, 39, and 40.

AUERBACH, D. J.; TULLY, J. C.; WODTKE, A. M. Chemical dynamics from the gas-phase to surfaces. *Natural Sciences*, Wiley Online Library, v. 1, n. 1, p. e10005, 2021. Cited 4 times on pages 51, 53, 54, and 57.

BAO, J. L.; TRUHLAR, D. G. Variational transition state theory: theoretical framework and recent developments. *Chemical Society Reviews*, Royal Society of Chemistry, v. 46, n. 24, p. 7548–7596, 2017. Cited 2 times on pages 54 and 58.

BARTLETT, R. J. Coupled-cluster approach to molecular structure and spectra: a step toward predictive quantum chemistry. *J. Phys. Chem.*, ACS Publications, v. 93, n. 5, p. 1697–1708, 1989. Cited 2 times on pages 41 and 63.

BARTLETT, R. J. et al. Non-iterative fifth-order triple and quadruple excitation energy corrections in correlated methods. *Chem. Phys. Lett.*, North-Holland, v. 165, n. 6, p. 513–522, 1990. Cited 2 times on pages 41 and 63.

BASU, N. *Essential Guide to Astrophysics*. [S.l.]: Educohack Press, 2025. Cited on page 22.

BAULCH, D. et al. Th. just, ja kerr, mj pilling, j. troe, rw walker and j. warnatz. *J. Phys. Chem. Ref. Data*, v. 21, n. 3, p. 411–569, 1992. Cited 2 times on pages 91 and 94.

BECK, E. D. et al. Po and pn in the wind of the oxygen-rich agb star ik tauri. *Astronomy & Astrophysics*, EDP Sciences, v. 558, p. A132, 2013. Cited 2 times on pages 17 and 27.

BERGNER, J. B. et al. Detection of phosphorus-bearing molecules toward a solar-type protostar. *Astrophys. J.*, v. 884, p. L36, 2019. Cited 2 times on pages 26 and 27.

BERNAL, J.; KOELEMAY, L.; ZIURYS, L. Detection of po in orion-kl: phosphorus chemistry in the plateau outflow. *The Astrophysical Journal*, IOP Publishing, v. 906, n. 1, p. 55, 2021. Cited 2 times on pages 26 and 27.

BODE, B. M.; GORDON, M. S. Macmolplt: a graphical user interface for gamess. *J. Mol. Graphics Modell.*, Elsevier, v. 16, n. 3, p. 133–138, 1998. Cited on page 62.

BORN, M.; OPPENHEIMER, J. R. [S.l.: s.n.], 1927. v. 84. 457 p. Cited on page 31.

CARIDADE, P. et al. Unimolecular and bimolecular calculations for hn2. *J. Phys. Chem. A*, ACS Publications, v. 109, n. 10, p. 2356–2363, 2005. Cited 3 times on pages 27, 29, and 86.

CARTECHINI, L. et al. Dynamics of the c+ c 2 h 2 reaction from differential and integral cross-section measurements in crossed-beam experiments. *The Journal of chemical physics*, American Institute of Physics, v. 116, n. 13, p. 5603–5611, 2002. Cited on page 18.

CHANTZOS, J. et al. The first steps of interstellar phosphorus chemistry. *Astron. Astrophys.*, v. 633, p. A54, 2020. Cited 4 times on pages 17, 27, 90, and 91.

CHEN, G. et al. Reaction dynamics of p (4 s)+ o 2 (x 3 σ g-)$\rightarrow$ o (3 p)+ po (x 2 π) on a global chipr potential energy surface of po 2 (x 2 a 1): implications for atmospheric modelling. *Atmospheric Chemistry and Physics*, Copernicus Publications Göttingen, Germany, v. 23, n. 18, p. 10643–10659, 2023. Cited 2 times on pages 76 and 77.

CHESNAVICH, W. J. Multiple transition states in unimolecular reactions. *The Journal of chemical physics*, AIP Publishing, v. 84, n. 5, p. 2615–2619, 1986. Cited on page 67.

ČÍŽEK, J. On the correlation problem in atomic and molecular systems. calculation of wavefunction components in ursell-type expansion using quantum-field theoretical methods. *The Journal of Chemical Physics*, AIP Publishing, v. 45, n. 11, p. 4256–4266, 1966. Cited on page 39.

CLARY, D. et al. Interstellar carbon chemistry: Reaction rates of neutral atomic carbon with organic molecules. *Astrophysical Journal, Part 1 (ISSN 0004-637X), vol. 422, no. 1, p. 416-422*, v. 422, p. 416–422, 1994. Cited on page 18.

CLYNE, M. A.; ONO, Y. Kinetic studies of ground-state phosphorus atoms. *Journal of the Chemical Society, Faraday Transactions 2: Molecular and Chemical Physics*, Royal Society of Chemistry, v. 78, n. 8, p. 1149–1164, 1982. Cited 3 times on pages 28, 74, and 75.

COLLABORATION, P. et al. Planck 2013 results. xvi. cosmological parameters. *A&A*, v. 571, p. A16, 2014. Cited on page 22.

COLLINS, M. A. Molecular potential-energy surfaces for chemical reaction dynamics. *Theoretical Chemistry Accounts*, Springer, v. 108, n. 6, p. 313–324, 2002. Cited 2 times on pages 46 and 47.

CONCEPCIÓN, J. G. de la et al. Relevance of the p+ o2 reaction for po formation in astrochemical environments: Electronic structure calculations and kinetic simulations. *The Astrophysical Journal*, IOP Publishing, v. 963, n. 2, p. 142, 2024. Cited on page 76.

CONCEPCIÓN, J. G. de la et al. Formation of phosphorus monoxide (po) in the interstellar medium: Insights from quantum-chemical and kinetic calculations. *The Astrophysical Journal*, IOP Publishing, v. 922, n. 2, p. 169, 2021. Cited 4 times on pages 17, 25, 27, and 96.

CRAMER, C. J. *Essentials of computational chemistry: theories and models*. [S.l.]: John Wiley & Sons, 2004. Cited 13 times on pages 34, 35, 36, 37, 38, 41, 46, 47, 50, 51, 52, 54, and 58.

DALGARNO, A. A serendipitous journey. *Annu. Rev. Astron. Astrophys.*, Annual Reviews, v. 46, n. 1, p. 1–20, 2008. Cited on page 21.

DOUGLAS, K. M. et al. Experimental study of the removal of ground-and excited-state phosphorus atoms by atmospherically relevant species. *J. Phys. Chem. A*, ACS Publications, v. 123, n. 44, p. 9469–9478, 2019. Cited 8 times on pages 28, 69, 70, 72, 73, 74, 75, and 76.

DOUGLAS, K. M.; GOBRECHT, D.; PLANE, J. M. Experimental study of the removal of excited state phosphorus atoms by h2o and h2: implications for the formation of po in stellar winds. *Mon. Not. R. Astron. Soc.*, Oxford University Press, v. 515, n. 1, p. 99–109, 2022. Cited 10 times on pages 29, 79, 85, 87, 88, 89, 93, 94, 95, and 96.

DUNNING, T. H. Gaussian Basis Sets for Use in Correlated Molecular Calculations. I. The Atoms Boron through Neon and Hydrogen. *J. Chem. Phys.*, v. 90, n. 2, p. 1007–1023, 1989. Cited 2 times on pages 62 and 63.

ECKART, C. The penetration of a potential barrier by electrons. *Phys. Rev.*, APS, v. 35, n. 11, p. 1303, 1930. Cited 3 times on pages 58, 64, and 67.

EVANS, M.; POLANYI, M. Inertia and driving force of chemical reactions. *Transactions of the Faraday Society*, Royal Society of Chemistry, v. 34, p. 11–24, 1938. Cited on page 54.

EYRING, H. The activated complex and the absolute rate of chemical reactions. *Chemical Reviews*, ACS Publications, v. 17, n. 1, p. 65–77, 1935. Cited 2 times on pages 54 and 57.

EYRING, H. The activated complex in chemical reactions. *The Journal of chemical physics*, American Institute of Physics, v. 3, n. 2, p. 107–115, 1935. Cited on page 54.

EYRING, H. The theory of absolute reaction rates. *Transactions of the Faraday Society*, Royal Society of Chemistry, v. 34, p. 41–48, 1938. Cited on page 54.

FERNÁNDEZ-RAMOS, A. et al. Modeling the kinetics of bimolecular reactions. *Chemical reviews*, ACS Publications, v. 106, n. 11, p. 4518–4584, 2006. Cited on page 45.

FERNÁNDEZ-RUZ, M.; JIMÉNEZ-SERRA, I.; AGUIRRE, J. A theoretical approach to the complex chemical evolution of phosphorus in the interstellar medium. *The Astrophysical Journal*, IOP Publishing, v. 956, n. 1, p. 47, 2023. Cited 4 times on pages 17, 27, 28, and 30.

FERRO-COSTAS, D.; TRUHLAR, D. G.; FERNÁNDEZ-RAMOS, A. Pilgrim v1. 0. 2019. Cited on page 65.

FERRO-COSTAS, D.; TRUHLAR, D. G.; FERNANDEZ-RAMOS, A. Pilgrim 2020.1. 2020. Cited on page 65.

FLEURY, B. et al. High-temperature measurements of acetylene vuv absorption cross sections and application to warm exoplanet atmospheres. *Astronomy & Astrophysics*, EDP Sciences, v. 693, p. A82, 2025. Cited on page 94.

FONTANI, F. et al. Origin of the pn molecule in star-forming regions: the enlarged sample. *Mon. Not. R. Astron. Soc.*, Oxford University Press, v. 489, n. 4, p. 4530–4542, 2019. Cited on page 26.

FRAY, N. et al. The origin of the cn radical in comets: A review from observations and models. *Planetary and Space Science*, Elsevier, v. 53, n. 12, p. 1243–1262, 2005. Cited on page 90.

GARRETT, B. C.; TRUHLAR, D. G. Variational transition state theory. In: *Theory and applications of computational chemistry*. [S.l.]: Elsevier, 2005. p. 67–87. Cited on page 58.

GEORGIEVSKII, Y.; KLIPPENSTEIN, S. J. Long-range transition state theory. *J. Chem. Phys.*, American Institute of Physics, v. 122, n. 19, p. 194103, 2005. Cited 3 times on pages 29, 87, and 93.

GEORGIEVSKII, Y. et al. Reformulation and solution of the master equation for multiple-well chemical reactions. *J. Phys. Chem. A*, ACS Publications, v. 117, n. 46, p. 12146–12154, 2013. Cited 5 times on pages 57, 60, 61, 64, and 67.

GOLDFORD, J. E. et al. Remnants of an ancient metabolism without phosphate. *Cell*, v. 168, p. 1126–1134, 2017. Cited 2 times on pages 17 and 25.

GOMES, A. C. et al. Formation of phosphorus monoxide through the $P(^4S) + O_2(^3\sigma^-) \rightarrow O(^3P) + PO(^2\pi)$ reaction. *Journal of Molecular Modeling*, Springer, v. 28, n. 9, p. 259, 2022. Cited 2 times on pages 68 and 76.

GOMES, A. C. et al. The P(^{4}S) + NH($^3\Sigma^-$) and N(^{4}S) + PH($^3\Sigma^-$) reactions as sources of interstellar phosphorus nitride. *Publications of the Astronomical Society of Australia*, Cambridge University Press, v. 40, p. e011, 2023. Cited on page 68.

GOMES, A. C. et al. Destruction of phosphorus nitride through the N(^{4}S) + PN($^1\sigma^+$) $\rightarrow$ N$_2$($^1\sigma^+$) + P(^{4}S) reaction. *Monthly Notices of the Royal Astronomical Society*, Oxford University Press, v. 518, n. 4, p. 5991–5996, 2023. Cited 2 times on pages 68 and 88.

GONZALEZ, C.; SCHLEGEL, H. B. Reaction path following in mass-weighted internal coordinates. *J. Phys. Chem.*, ACS Publications, v. 94, n. 14, p. 5523–5527, 1990. Cited 2 times on pages 63 and 65.

GUÉLIN, M. et al. Free cp in irc + 10216. *Astron. Astrophys.*, v. 230, p. L9–L11, 1990. Cited 2 times on pages 27 and 90.

HAASLER, D. et al. First extragalactic detection of a phosphorus-bearing molecule with alchemi: Phosphorus nitride (pn). *Astronomy & Astrophysics*, EDP Sciences, v. 659, p. A158, 2022. Cited on page 27.

HACK, W.; WAGNER, H. G.; ZASYPKIN, A. Elementary reactions of nh (a1δ) and nh (x3σ) with n, o and no. *Berichte der Bunsengesellschaft für physikalische Chemie*, Wiley Online Library, v. 98, n. 2, p. 156–164, 1994. Cited 3 times on pages 27, 29, and 86.

HAN, X. et al. Combination of cn (1-0), hcn (1-0), and hnc (1-0): A possible indicator for a high-mass star formation sequence in the milky way. *Astronomy & Astrophysics*, EDP Sciences, v. 576, p. A131, 2015. Cited on page 90.

HANWELL, M. D. et al. Avogadro: an advanced semantic chemical editor, visualization, and analysis platform. *J. Cheminform.*, BioMed Central, v. 4, n. 1, p. 1–17, 2012. Cited on page 62.

HARDING, L. B.; GEORGIEVSKII, Y.; KLIPPENSTEIN, S. J. Predictive theory for hydrogen atom- hydrocarbon radical association kinetics. *J. Phys. Chem. A*, ACS Publications, v. 109, n. 21, p. 4646–4656, 2005. Cited on page 66.

HENSHAW, T. et al. The p (4su)+ n3 (2iig) reaction: chemical generation of a new metastable state of pn. *Journal of Physical Chemistry*, ACS Publications, v. 91, n. 11, p. 2838–2842, 1987. Cited 3 times on pages 28, 74, and 75.

HERBST, E.; JR, J. T. Y. *Introduction: astrochemistry*. [S.l.]: ACS Publications, 2013. 8707–8709 p. Cited on page 21.

HERBST, E.; KLEMPERER, W. The formation and depletion of molecules in dense interstellar clouds. *Astrophysical Journal, Vol. 185, pp. 505-534 (1973)*, v. 185, p. 505–534, 1973. Cited on page 46.

HERBST, E. et al. The effect of rapid neutral-neutral reactions on chemical models of dense interstellar clouds. *Monthly Notices of the Royal Astronomical Society*, Oxford University Press Oxford, UK, v. 268, n. 2, p. 335–344, 1994. Cited 2 times on pages 18 and 30.

HERZBERG, G. *Molecular Spectra and molecular structure-Vol I.* [S.l.]: Read Books Ltd, 2013. v. 1. Cited 2 times on pages 49 and 50.

HINSHAW, G. et al. Nine-year wilkinson microwave anisotropy probe (wmap) observations: cosmological parameter results. *The Astrophysical Journal Supplement Series*, IOP Publishing, v. 208, n. 2, p. 19, 2013. Cited on page 22.

HOHENBERG, P.; KOHN, W. Inhomogeneous electron gas. *Physical review*, APS, v. 136, n. 3B, p. B864, 1964. Cited on page 34.

HUNTER, T. Why nature chose phosphate to modify proteins. *Philosophical Transactions of the Royal Society B: Biological Sciences*, The Royal Society, v. 367, n. 1602, p. 2513–2516, 2012. Cited 2 times on pages 17 and 25.

HUSAIN, D.; NORRIS, P. E. Reactions of phosphorus atoms, p (3 4 s [fraction three-over-two]), studied by attenuation of atomic resonance radiation in the vacuum ultraviolet. *Journal of the Chemical Society, Faraday Transactions 2: Molecular and Chemical Physics*, Royal Society of Chemistry, v. 73, n. 7, p. 1107–1115, 1977. Cited 3 times on pages 28, 74, and 75.

HUSAIN, D.; SLATER, N. K. Time-resolved resonance fluorescence studies of ground state phosphorus atoms, p [3 p 3 (4 s [fraction three-over-two])]. *Journal of the Chemical Society, Faraday Transactions 2: Molecular and Chemical Physics*, Royal Society of Chemistry, v. 74, p. 1627–1643, 1978. Cited 3 times on pages 28, 74, and 75.

JENSEN, F. *Introduction to computational chemistry*. [S.l.]: John wiley & sons, 2007. Cited 14 times on pages 35, 36, 37, 38, 41, 46, 47, 48, 50, 51, 52, 53, 54, and 57.

JIMÉNEZ-SERRA, I. et al. The chemistry of phosphorus-bearing molecules under energetic phenomena. *Astrophys. J.*, v. 862, p. 128, 2018. Cited 2 times on pages 27 and 30.

KAISER, R. I. et al. A combined crossed molecular beam and ab initio investigation of c 2 and c 3 elementary reactions with unsaturated hydrocarbons—pathways to hydrogen deficient hydrocarbon radicals in combustion flames. *Faraday discussions*, Royal Society of Chemistry, v. 119, p. 51–66, 2002. Cited on page 18.

KENDALL, R. A.; DUNNING, T. H.; HARRISON, R. J. Electron Affinities of the First-Row Atoms Revisited. Systematic Basis Sets and Wave Functions. *J. Chem. Phys.*, v. 96, n. 9, p. 6796–6806, 1992. Cited 2 times on pages 62 and 63.

KLIPPENSTEIN, S. J. A bond length reaction coordinate for unimolecular reactions. ii. microcanonical and canonical implementations with application to the dissociation of ncno. *J. Chem. Phys.*, American Institute of Physics, v. 94, n. 10, p. 6469–6482, 1991. Cited 2 times on pages 66 and 86.

KLIPPENSTEIN, S. J. Variational optimizations in the rice–ramsperger–kassel–marcus theory calculations for unimolecular dissociations with no reverse barrier. *J. Chem. Phys.*, American Institute of Physics, v. 96, n. 1, p. 367–371, 1992. Cited 2 times on pages 66 and 86.

KLIPPENSTEIN, S. J. From theoretical reaction dynamics to chemical modeling of combustion. *Proc. Combust. Inst.*, Elsevier, v. 36, n. 1, p. 77–111, 2017. Cited on page 59.

KLIPPENSTEIN, S. J.; MILLER, J. A. From the time-dependent, multiple-well master equation to phenomenological rate coefficients. *The Journal of Physical Chemistry A*, ACS Publications, v. 106, n. 40, p. 9267–9277, 2002. Cited 2 times on pages 59 and 61.

KLIPPENSTEIN, S. J.; PANDE, V. S.; TRUHLAR, D. G. Chemical kinetics and mechanisms of complex systems: A perspective on recent theoretical advances. *Journal of the American Chemical Society*, ACS Publications, v. 136, n. 2, p. 528–546, 2014. Cited 2 times on pages 43 and 48.

KNIZIA, G.; ADLER, T. B.; WERNER, H.-J. Simplified ccsd(t)-f12 methods: Theory and benchmarks. *J. Chem. Phys.*, American Institute of Physics, v. 130, p. 054104, 2009. Cited 3 times on pages 41, 63, and 66.

KOELEMAY, L. et al. Laboratory and astronomical detection of the sip radical (x2π i): more circumstellar phosphorus. *The Astrophysical Journal Letters*, IOP Publishing, v. 940, n. 1, p. L11, 2022. Cited on page 27.

KOELEMAY, L.; GOLD, K.; ZIURYS, L. Phosphorus-bearing molecules po and pn at the edge of the galaxy. *Nature*, Nature Publishing Group UK London, v. 623, n. 7986, p. 292–295, 2023. Cited on page 26.

KOHN, W.; SHAM, L. J. Self-consistent equations including exchange and correlation effects. *Physical review*, APS, v. 140, n. 4A, p. A1133, 1965. Cited 2 times on pages 34 and 62.

LECCA, P. Stochastic chemical kinetics: A review of the modelling and simulation approaches. *Biophysical reviews*, Springer, v. 5, p. 323–345, 2013. Cited on page 45.

LEE, J. D. *Química inorgânica não tão concisa*. [S.l.]: Edgard Blucher, 1999. Cited on page 25.

LEE, T. J. Comparison of the t1 and d1 diagnostics for electronic structure theory: a new definition for the open-shell d1 diagnostic. *Chem. Phys. Lett.*, v. 372, p. 362–367, 2003. Cited 2 times on pages 63 and 72.

LEE, T. J.; TAYLOR, P. R. A diagnostic for determining the quality of single-reference electron correlation methods. *Int. J. Quant. Chem. Symp.*, v. 23, p. 199–207, 1989. Cited 2 times on pages 63 and 72.

LEFLOCH, B. et al. Phosphorus-bearing molecules in solar-type star-forming regions: First po detection. *Mon. Not. R. Astron. Soc.*, v. 462, p. 3937–3944, 2016. Cited 5 times on pages 17, 26, 27, 29, and 79.

LEININGER, M. L. et al. A new diagnostic for open-shell coupled-cluster theory. *Chem. Phys. Lett.*, v. 328, p. 431–436, 2000. Cited 2 times on pages 63 and 72.

LENNARD-JONES, J.; HALL, G. Je lennard-jones proc. In: *Roy. Soc. Lond. A*. [S.l.: s.n.], 1924. v. 106, p. 441. Cited on page 48.

LEVINE, I. N. *Quantum Chemistry*. Upper Saddle River, New Jersey: Prentice Hall, 2000. Cited 14 times on pages 31, 32, 33, 34, 35, 36, 37, 38, 39, 40, 41, 42, 45, and 54.

LIU, Y. P. et al. Molecular modeling of the kinetic isotope effect for the [1, 5]-sigmatropic rearrangement of cis-1, 3-pentadiene. *J. Am. Chem. Soc*, ACS Publications, v. 115, n. 6, p. 2408–2415, 1993. Cited 2 times on pages 59 and 65.

MACIÁ, E. The role of phosphorus in chemical evolution. *Chem. Soc. Rev.*, v. 34, p. 691–701, 2005. Cited 2 times on pages 17 and 25.

MANION, J. A. et al. Nist chemical kinetics database, nist standard reference database 17, version 7.0 (web version), release 1.6.8, data version 2015.09, national institute of standards and technology. National Institute of Standards and Technology, Gaithersburg, Maryland, p. 20899–8320, 2015. Cited 2 times on pages 45 and 46.

MARDIROSSIAN, N.; HEAD-GORDON, M. How accurate are the minnesota density functionals for noncovalent interactions, isomerization energies, thermochemistry, and barrier heights involving molecules composed of main-group elements? *J. Chem. Theory Comput.*, ACS Publications, v. 12, n. 9, p. 4303–4325, 2016. Cited on page 62.

MARTIN, J. M.; UZAN, O. Basis set convergence in second-row compounds. the importance of core polarization functions. *Chem. Phys. Lett.*, Elsevier, v. 282, n. 1, p. 16–24, 1998. Cited on page 67.

MCGUIRE, B. A. 2021 census of interstellar, circumstellar, extragalactic, protoplanetary disk, and exoplanetary molecules. *The Astrophysical Journal Supplement Series*, IOP Publishing, v. 259, n. 2, p. 30, 2022. Cited 3 times on pages 17, 26, and 27.

MCKELLAR, A. Evidence for the molecular origin of some hitherto unidentified interstellar lines. *Publications of the Astronomical Society of the Pacific*, JSTOR, v. 52, n. 307, p. 187–192, 1940. Cited on page 90.

MCQUARRIE, D. A. *Statistical Mechanics*. [S.l.]: Indiana University,Harper and Row, New York, 1976. v. 1. Cited on page 53.

MCQUARRIE, D. A.; SIMON, J. D. *Physical chemistry: a molecular approach*. [S.l.]: University science books Sausalito, CA, 1997. v. 1. Cited 10 times on pages 41, 42, 43, 44, 45, 48, 50, 54, 55, and 56.

MILAM, S. et al. Constraining phosphorus chemistry in carbon-and oxygen-rich circumstellar envelopes: observations of pn, hcp, and cp. *The Astrophysical Journal*, IOP Publishing, v. 684, n. 1, p. 618, 2008. Cited on page 27.

MILLAR, T. et al. The umist database for astrochemistry 2022. *Astronomy & Astrophysics*, EDP Sciences, v. 682, p. A109, 2024. Cited 7 times on pages 26, 29, 45, 46, 79, 87, and 93.

MILLAR, T. J.; BENNETT, A.; HERBST, E. An efficient gas phase synthesis for interstellar pn. *Mon. Not. R. Astron. Soc.*, v. 229, p. 41–44, 1987. Cited 4 times on pages 26, 29, 81, and 96.

MILLER, J. A. et al. The conversion of hcn to no and n2 in h2- o2- hcn- ar flames at low pressure. In: ELSEVIER. *Symposium (International) on Combustion*. [S.l.], 1985. v. 20, n. 1, p. 673–684. Cited 3 times on pages 27, 29, and 86.

MILLER, J. A.; KLIPPENSTEIN, S. J. Master equation methods in gas phase chemical kinetics. *The Journal of Physical Chemistry A*, ACS Publications, v. 110, n. 36, p. 10528–10544, 2006. Cited 3 times on pages 59, 60, and 61.

MILLER, J. A.; KLIPPENSTEIN, S. J. Determining phenomenological rate coefficients from a time-dependent, multiple-well master equation:“species reduction” at high temperatures. *Physical Chemistry Chemical Physics*, Royal Society of Chemistry, v. 15, n. 13, p. 4744–4753, 2013. Cited on page 60.

MILLER, J. A. et al. Detailed balance in multiple-well chemical reactions. *Physical Chemistry Chemical Physics*, Royal Society of Chemistry, v. 11, n. 8, p. 1128–1137, 2009. Cited on page 60.

MOSKALEVA, L.; LIN, M.-C. Computational study on the energetics of ncn isomers and the kinetics of the c+ n2 n+ cn reaction. *The Journal of Physical Chemistry A*, ACS Publications, v. 105, n. 16, p. 4156–4163, 2001. Cited 2 times on pages 91 and 93.

MOTA, V. C. et al. Accurate potential energy surface for quartet state hn_2 and interplay of $n(^4s)+nh(x^3\sigma)$ versus $h+n_2(a^3\sigma u+)$ reactions. *J. Phys. Chem. A*, ACS Publications, v. 124, n. 5, p. 781–789, 2020. Cited on page 83.

MOTA, V. C.; VARANDAS, A. J. C. $hn_2(^2a')$ electronic manifold. i. a global ab initio study of first two states. *J. Phys. Chem. A*, v. 111, p. 10191, 2007. Cited on page 83.

MOTA, V. C.; VARANDAS, A. J. C. $hn_2(^2a')$ electronic manifold. ii. ab initio based double-sheeted dmbe potential energy surface via a global diabatization angle. *J. Phys. Chem. A*, v. 112, p. 3768–3786, 2008. Cited on page 83.

NEESE, F. et al. The orca quantum chemistry program package. *J. Chem. Phys.*, AIP Publishing LLC, v. 152, n. 22, p. 224108, 2020. Cited 2 times on pages 64 and 65.

OLIVEIRA, L. P. de et al. A review of kinetic modeling methodologies for complex processes. *Oil & Gas Science and Technology–Revue d'IFP Energies nouvelles*, EDP Sciences, v. 71, n. 3, p. 45, 2016. Cited 5 times on pages 43, 44, 50, 54, and 57.

PAGE, M.; JR, J. W. M. On evaluating the reaction path hamiltonian. *J. Chem. Phys.*, American Institute of Physics, v. 88, n. 2, p. 922–935, 1988. Cited on page 65.

PARON, S. et al. Cyano radical emission at small spatial scales towards massive protostars. *Astronomy & Astrophysics*, EDP Sciences, v. 653, p. A77, 2021. Cited on page 90.

PASEK, M. A.; LAURETTA, D. S. Aqueous corrosion of phosphide minerals from iron meteorites: a highly reactive source of prebiotic phosphorus on the surface of the early earth. *Astrobiology*, Mary Ann Liebert, Inc. 2 Madison Avenue Larchmont, NY 10538 USA, v. 5, n. 4, p. 515–535, 2005. Cited on page 17.

PAULI, W. Uber das h-theorem vom anwachsen der entropie vom standpunkt der neuen quantenmechanik. *Probleme der Modernen Physik. Arnold Sommerfeld zum*, v. 60, p. 30–45, 1928. Cited on page 59.

PECHUKAS, P.; LIGHT, J. C. On detailed balancing and statistical theories of chemical kinetics. *The Journal of Chemical Physics*, AIP Publishing, v. 42, n. 9, p. 3281–3291, 1965. Cited on page 67.

PEVERATI, R.; TRUHLAR, D. G. M11-l: A local density functional that provides improved accuracy for electronic structure calculations in chemistry and physics. *J. Phys. Chem. Lett.*, ACS Publications, v. 3, n. 1, p. 117–124, 2012. Cited 3 times on pages 28, 62, and 73.

PUZZARINI, C. Gas-phase chemistry in the interstellar medium: the role of laboratory astrochemistry. *Frontiers in Astronomy and Space Sciences*, Frontiers Media SA, v. 8, p. 811342, 2022. Cited 3 times on pages 18, 21, and 31.

RAGHAVACHARI, K. et al. A fifth-order perturbation comparison of electron correlation theories. *Chem. Phys. Lett.*, North-Holland, v. 157, n. 6, p. 479–483, 1989. Cited 2 times on pages 41 and 63.

RIVILLA, V. M. et al. Alma and rosina detections of phosphorus-bearing molecules: The interstellar thread between star-forming regions and comets. *Mon. Not. R. Astron. Soc.*, v. 492, p. 1180–1198, 2020. Cited 6 times on pages 17, 23, 24, 25, 26, and 27.

RIVILLA, V. M. et al. The first detections of the key prebiotic molecule po in star-forming regions. *Astrophys. J.*, v. 826, p. 161, 2016. Cited 2 times on pages 26 and 27.

RIVILLA, V. M. et al. Phosphorus-bearing molecules in the galactic center. *Mon. Not. R. Astron. Soc. Lett.*, v. 475, p. L30–L34, 2018. Cited on page 27.

SCHMIDT, M. W. et al. General atomic and molecular electronic structure system. *J. Comput. Chem.*, v. 14, p. 1347, 1993. Cited 2 times on pages 62 and 64.

SHIOZAKI, T.; KNIZIA, G.; WERNER, H.-J. Explicitly correlated multireference configuration interaction: Mrci-f12. *J. Chem. Phys.*, American Institute of Physics, v. 134, n. 3, p. 034113, 2011. Cited 3 times on pages 39, 63, and 64.

SHRIVER, D. F. et al. *Química inorgânica*. [S.l.]: Bookman, 2008. Cited on page 25.

SIL, M. et al. Chemical complexity of phosphorous-bearing species in various regions of the interstellar medium. *The Astronomical Journal*, IOP Publishing, v. 162, n. 3, p. 119, 2021. Cited on page 27.

SILVA, M. X. et al. New routes for pn destruction and formation in the interstellar medium via neutral-neutral gas-phase reactions and an extended database for reactions involving phosphorus. *Astronomy & Astrophysics*, EDP Sciences, v. 696, p. A170, 2025. Cited 7 times on pages , 17, 26, 29, 68, 95, and 96.

SILVER, D. M. Hierarchy of symmetry conservation rules governing chemical reaction systems. *Journal of the American Chemical Society*, ACS Publications, v. 96, n. 19, p. 5959–5967, 1974. Cited on page 49.

SMITH, I. W.; HERBST, E.; CHANG, Q. Rapid neutral-neutral reactions at low temperatures: a new network and first results for tmc-1. *Mon. Not. R. Astron. Soc.*, Blackwell Science Ltd Oxford, UK, v. 350, n. 1, p. 323–330, 2004. Cited 5 times on pages 18, 26, 29, 31, and 86.

SNELL, R. L. Interstellar medium. In: *Encyclopedia of astrobiology*. [S.l.]: Springer, 2023. p. 1502–1509. Cited 2 times on pages 22 and 23.

SOUSA-SILVA, C. et al. Phosphine as a biosignature gas in exoplanet atmospheres. *Astrobiology*, v. 20, p. 235–268, 2020. Cited 2 times on pages 17 and 25.

SOUZA, A. C.; SILVA, M. X.; GALVÃO, B. R. Interconversion mechanisms of pn and po in the interstellar medium through simple atom–diatom collisions. *Monthly Notices of the Royal Astronomical Society*, Oxford University Press, v. 507, n. 2, p. 1899–1903, 2021. Cited 2 times on pages 26 and 29.

SZABO, A.; OSTLUND, N. S. *Modern Quantum Chemistry: Introduction to Advanced Electronic Structure Theory*. New York: McGraw-Hill, 1989. Cited 6 times on pages 31, 32, 33, 36, 37, and 39.

SZALAY, P. G. et al. Multiconfiguration Self-Consistent Field and Multireference Configuration Interaction Methods and Applications. *Chem. Rev.*, v. 112, n. 1, p. 108–181, 2012. Cited 3 times on pages 39, 63, and 64.

TENENBAUM, E.; ZIURYS, L. A search for phosphine in circumstellar envelopes: Ph3 in irc+ 10216 and crl 2688? *The Astrophysical Journal*, IOP Publishing, v. 680, n. 2, p. L121, 2008. Cited on page 27.

TENENBAUM, E. D.; WOOLF, N. J.; ZIURYS, L. M. Identification of phosphorus monoxide ($x^2\pi_r$) in vy canis majoris: Detection of the first p-o bond in space. *Astrophys. J.*, v. 666, p. L29–L32, 2007. Cited 2 times on pages 17 and 27.

TERZIEVA, R.; HERBST, E. The sensitivity of gas-phase chemical models of interstellar clouds to c and o elemental abundances and to a new formation mechanism for ammonia. *The Astrophysical Journal*, IOP Publishing, v. 501, n. 1, p. 207, 1998. Cited on page 18.

THORNE, L. R. et al. The chemistry of phosphorus in dense interstellar clouds. *Astrophys. J.*, v. 280, p. 139–143, 1984. Cited 2 times on pages 17 and 27.

TIELENS, A. G. *Molecular astrophysics*. [S.l.]: Cambridge University Press, 2021. Cited 5 times on pages 21, 22, 23, 30, and 31.

TISHCHENKO, O.; ZHENG, J.; TRUHLAR, D. G. Multireference model chemistries for thermochemical kinetics. *J. Chem. Theory Comput.*, ACS Publications, v. 4, n. 8, p. 1208–1219, 2008. Cited 2 times on pages 65 and 66.

TRUHLAR, D. G.; GARRETT, B. C. Variational transition-state theory. *Acc. Chem. Res.*, ACS Publications, v. 13, n. 12, p. 440–448, 1980. Cited on page 58.

TRUHLAR, D. G.; GARRETT, B. C. Variational transition state theory. *Annu. Rev. Phys. Chem.*, Annual Reviews 4139 El Camino Way, PO Box 10139, Palo Alto, CA 94303-0139, USA, v. 35, n. 1, p. 159–189, 1984. Cited 3 times on pages 53, 57, and 58.

TRUHLAR, D. G.; GORDON, M. S. From force fields to dynamics: classical and quantal paths. *Science*, American Association for the Advancement of Science, v. 249, n. 4968, p. 491–498, 1990. Cited on page 58.

TURNER, B. E.; BALLY, J. Detection of interstellar pn: The first identified phosphorus compound in the interstellar medium. *Astrophys. J.*, v. 321, p. L75–L79, 1987. Cited 2 times on pages 26 and 27.

WAKELAM, V. et al. The 2024 kida network for interstellar chemistry. *Astronomy & Astrophysics*, EDP Sciences, v. 689, p. A63, 2024. Cited 8 times on pages 26, 29, 45, 46, 79, 87, 93, and 96.

WAKELAM, V. et al. The 2014 kida network for interstellar chemistry. *The Astrophysical Journal Supplement Series*, IOP Publishing, v. 217, n. 2, p. 20, 2015. Cited on page 95.

WAKELAM, V. et al. Reaction networks for interstellar chemical modelling: improvements and challenges. *Space science reviews*, Springer, v. 156, p. 13–72, 2010. Cited on page 31.

WALCH, S. P.; DUCHOVIC, R. J.; ROHLFING, C. M. *J. Chem. Phys.*, v. 90, p. 3230, 1989. Cited on page 83.

WERNER, H. et al. Molpro, version 2015.1, a package of ab initio programs. *University of Cardiff Chemistry Consultants (UC3): Cardiff, Wales, UK*, 2015. Cited 2 times on pages 62 and 64.

WERNER, H.-J. et al. Molpro: a general-purpose quantum chemistry program package. *WIREs Comput. Mol. Sci.*, v. 2, p. 242–253, 2012. Cited on page 62.

WESTHEIMER, F. H. Why nature chose phosphates. *Science*, American Association for the Advancement of Science, v. 235, n. 4793, p. 1173–1178, 1987. Cited on page 17.

WIGNER, E. über die erhaltungssätze in der quantenmechanik. *Nachrichten von der Gesellschaft der Wissenschaften zu Göttingen, Mathematisch-Physikalische Klasse*, p. 375–381, 1927. Cited 2 times on pages 49 and 63.

WIGNER, E.; WITMER, E. On the structure of the spectra of two-atomic molecules according to quantum mechanics. World Scientific, p. 287–311, 1928. Cited on page 49.

WIGNER, E. P.; WITMER, E. E. Über die struktur der zweiatomigen molekelspektren nach der quantenmechanik. *The Collected Works of Eugene Paul Wigner: Part A: The Scientific Papers*, Springer, p. 167–194, 1928. Cited on page 49.

WOODALL, J. et al. The umist database for astrochemistry 2006. *Astronomy & Astrophysics*, EDP Sciences, v. 466, n. 3, p. 1197–1204, 2007. Cited on page 46.

YAMAMOTO, S. *Introduction to Astrochemistry: Chemical Evolution from Interstellar Clouds to Star and Planet Formation*. [S.l.]: Astronomy and Astrophysics Library, Springer, 2017. Cited 6 times on pages 18, 21, 22, 23, 26, and 30.

ZHAO, Y.; TRUHLAR, D. G. Density functionals with broad applicability in chemistry. *Accounts of chemical research*, ACS Publications, v. 41, n. 2, p. 157–167, 2008. Cited on page 62.

ZHAO, Y.; TRUHLAR, D. G. Exploring the limit of accuracy of the global hybrid meta density functional for main-group thermochemistry, kinetics, and noncovalent interactions. *J. Chem. Theory Comput.*, ACS Publications, v. 4, n. 11, p. 1849–1868, 2008. Cited 2 times on pages 28 and 62.

ZHAO, Y.; TRUHLAR, D. G. The m06 suite of density functionals for main group thermochemistry, thermochemical kinetics, noncovalent interactions, excited states, and transition elements: two new functionals and systematic testing of four m06-class functionals and 12 other functionals. *Theor. Chem. Acc.*, Springer, v. 120, n. 1-3, p. 215–241, 2008. Cited on page 62.

ZIURYS, L. M. Detection of interstellar pn: The first phosphorus-bearing species observed in molecular clouds. *Astrophys. J.*, v. 321, p. L81–L85, 1987. Cited 2 times on pages 26 and 27.

ZIURYS, L. M. The chemistry in circumstellar envelopes of evolved stars: Following the origin of the elements to the origin of life. *Proceedings of the National Academy of Sciences*, National Acad Sciences, v. 103, n. 33, p. 12274–12279, 2006. Cited 3 times on pages 23, 24, and 25.

ZIURYS, L. M. Prebiotic astrochemistry from astronomical observations and laboratory spectroscopy. *Annual Review of Physical Chemistry*, Annual Reviews, v. 75, 2024. Cited 5 times on pages 17, 22, 24, 27, and 28.

APPENDIX A – List of publications related to this work

1. GOMES, A. C. R. *et al.* Formation of phosphorus monoxide through the $P(^4S)+O_2(^3\Sigma^-) \rightarrow O(^3P) + PO(^2\Pi)$ reaction. *Journal of Molecular Modeling*, 28, 259 (2022). Available at: <https://doi.org/10.1007/s00894-022-05242-4>.

2. GOMES, A. C. R. *et al.* Destruction of phosphorus nitride through the $N(^4S)+PN(^1\Sigma^+) \rightarrow N_2(^1\Sigma^+) + P(^4S)$ reaction. *Monthly Notices of the Royal Astronomical Society*, 518 (4), 5991–5996 (2023). Available at: <https://doi.org/10.1093/mnras/stac3460>.

3. GOMES, A. C. R. *et al.* The $P(^4S) + NH(^3\Sigma^-)$ and $N(^4S) + PH(^3\Sigma^-)$ reactions as sources of interstellar phosphorus nitride. *Publications of the Astronomical Society of Australia*, 40, e011 (2023). Available at: <https://doi.org/10.1017/pasa.2023.13>.

4. SILVA, M. X. *et al.* New routes for PN destruction and formation in the ISM via neutral-neutral gas-phase reactions and an extended database for reactions involving phosphorus. *Astronomy & Astrophysics*, 696, A170 (2025). Available at: <https://doi.org/10.1051/0004-6361/202453204>.